

**FEDERAL UNIVERSITY OF ITAJUBÁ
POST-GRADUATE PROGRAM IN
PHYSICS**

Porous silicon photonic crystals: Surface passivation and etch-stop effect on the optical response.

Jackelyne Lisset Medina Villanueva

Itajubá, February 10, 2023

**FEDERAL UNIVERSITY OF ITAJUBÁ
POST-GRADUATE PROGRAM IN
PHYSICS**

Jackelyne Lisset Medina Villanueva

**Porous silicon photonic crystals: Surface
passivation and etch-stop effect on the optical
response.**

Submitted to the Post-Graduate Program in Physics as part of
the requirements for obtaining the Master's Degree in Physical
Sciences.

Concentration Area: Photonics

Supervisor: Prof. Dr. Danilo Roque Huanca

Co-supervisor: Prof. Dr. Adhimar Flávio Oliveira

February 10, 2023

Itajubá

Jackelyne Lisset Medina Villanueva

Porous silicon photonic crystals: Surface passivation and etch-stop effect on the optical response/ Jackelyne Lisset Medina Villanueva. – Itajubá, February 10, 2023-

100 p. : il. (some color.) ; 30 cm.

Supervisor: Prof. Dr. Danilo Roque Huanca

Thesis (Master's degree)

Federal University of Itajubá

Post-Graduate Program in Physics, February 10, 2023.

1. Porous silicon photonic crystal. 2. Porous surface passivation. 3. Etch-stop effect. I. Prof. Dr. Danilo Roque Huanca. II. Federal University of Itajubá. III. Post-graduate program in physics. IV. Porous silicon photonic crystals: Surface passivation and etch-stop effect on the optical response.

CDU 07:181:009.3

Acknowledgements

First and foremost, I would like to thank God who has gifted me with countless blessings, knowledge and opportunities so that I could finally complete this work.

Apart from my efforts, the success of this work depends largely on the encouragement and guidance of many others. I take this opportunity to express my gratitude to Prof. Danilo Roque Huanca, who gave me the opportunity to work on a topic that interested me, and Prof. Adhimar Flávio Oliveira, who contributed significantly to my academic growth and the successful completion of this work.

To my parents, who have always given me their affection and unconditional support, which has helped to achieve my goal and finish this path through science. To my mother, Luz, who was always on my guard and gave me the motivation not to give up. To my father, Lidio, who gave me the sense of manual labor. To my siblings, whom I always turn to when I need academic support, even during this time of my master's studies.

A special thanks to my great friend Neil, with whom I share pleasant moments of coexistence and philosophical conversations in moments of stress, and who has shown me his passion for teaching. Thank you to my friend Joaquin for keeping me company during this time of mastery. I am so grateful to MPhys. Alejandro Condori for the selfless help you have given me at all times in learning programming.

I would like to thank the Structural Characterization Laboratory for the SEM facilities and to FAPEMIG for the financial support of the scholarship.

*“Science knows no country, because belongs to humanity, and is the torch which
illuminates the world.”
(Louis Pasteur)*



Abstract

The aim of this study was to investigate the influence of the etch-stop time on the structural and optical properties of multilayer structures and their passivation to avoid aging effects. Structural analysis by scanning electron microscopy (SEM) and the optical reflectance data fitting procedure have shown that the inclusion of a pause during the growth of the porous matrix promotes the formation of thicker layers (2638 nm, for 10 s of pause), compared with the layer with low porosity without pause (2584 nm). Similar behavior was observed for high porosity layers changing from 4500 to 4780 nm. This trend was also observed for multilayer structures. As for porosity, an opposite behavior was observed, decreasing in about 9.5% and 6.5% with increasing etch stop time for single layers with low and high porosity, respectively. This phenomenon was attributed to the recovery of hydrofluoric acid consumed during pore formation at the electrolyte-silicon interface. To obtain 1D photonic crystals (1D-PC) of porous silicon with optical responses close to those projected, this phenomenon must be taken into account in device development. The fabrication of 1D-PC with a sequence starting with a layer with high porosity and others where the first upper layer has low porosity proves that the increasing effect of thickness and the decrease of porosity does not depend on the stacking order. However, the thermal treatment made in air environment shows significant changes in the optical response after the oxidation at 400°C. Since the oxidation of porous silicon depends on the characteristics of the porous matrix, it is concluded that the etch-stop promotes the formation of high and low porosity layers with different microstructures, so that after thermal annealing at 1000°C in devices with the first upper layer with high porosity, the main photonic band gap (PBG) is destroyed, i.e., the optical thickness of the high and low porosity layers no longer obeys Bragg's law due to the contraction-expansion effect of the low and high porosity layers.

Three different materials were used for surface passivation: thermal silicon oxide (SiO_2), gold (Au), and titanium oxide (TiO_2). Despite the passivation layer, the presence of these elements resulted in a blue shift of the PBG. However, in the case of the deposited TiO_2 , some samples showed a red shift, while in others the PBG is not changed. The red shift was associated with the presence of xylene in the sol-gel TiO_2 within the pores. Unaltered PBG was associated with the formation of a thin pore-sealing TiO_2 sol-gel layer. After thermal treatment, the typical blue shift was observed. Despite the passivation material, fast Fourier infrared spectroscopy (FTIR) reveals the presence of SiO_2 in addition to the Au or TiO_2 phases. Energy dispersive X-ray spectroscopy analysis (EDS) showed that Au and TiO_2 were deposited in a deep concentration gradient, but with a homogeneous distribution along the sample surface. X-ray diffraction (XRD) showed that after thermal treatment at 450°C, the rutile and anatase phases coexist, with the latter predominating. The stability of the optical properties after passivation was confirmed by measurements

of the samples after 20 and 36 weeks of storage. No spectral changes were observed in the PBG position.

Key-words: Porous silicon photonic crystal. Porous surface passivation. Etch-stop effect.

Resumo

O objetivo deste estudo foi investigar a influência do tempo de pausa (*etch-stop*) nas propriedades estruturais e ópticas de estruturas multicamadas e sua passivação para evitar efeitos de envelhecimento. A análise estrutural por microscopia eletrônica de varredura (MEV) e o procedimento de ajuste dos dados de refletância óptica mostraram que a inclusão de uma pausa durante o crescimento da matriz porosa promove a formação de camadas mais espessas (2638 nm, em 10 s de pausa), em comparação com a camada com baixa porosidade sem pausa (2584 nm). Um comportamento semelhante foi observado para camadas de alta porosidade variando de 4500 a 4780 nm. Essa tendência também foi observada para estruturas multicamadas. Quanto à porosidade, observou-se um comportamento oposto, diminuindo em cerca de 9,5% e 6,5% com o aumento do tempo do *etch-stop* para camadas individuais com baixa e alta porosidade, respectivamente. Este fenômeno foi atribuído à recuperação do ácido fluorídrico consumido durante a formação dos poros na interface eletrólito-silício. Para obter cristais fotônicos 1D (1D-PC) de silício poroso com respostas ópticas próximas às projetadas, esse fenômeno deve ser levado em consideração no desenvolvimento do dispositivo. A fabricação do 1D-PC com uma sequência iniciando com uma camada com alta porosidade e outras onde a primeira camada superior possui baixa porosidade prova que o efeito de aumento da espessura e diminuição da porosidade independe da ordem de empilhamento. No entanto, o tratamento térmico feito em ambiente de ar mostra mudanças significativas na resposta óptica após a oxidação a 400°C. Como a oxidação do silício poroso depende das características da matriz porosa, conclui-se que o *etch-stop* promove a formação de camadas de alta e baixa porosidade com diferentes microestruturas, de modo que após o recozimento térmico a 1000°C em dispositivos com a primeira camada superior com alta porosidade, o gap fotônico principal (PBG) é destruído, ou seja, a espessura óptica das camadas de alta e baixa porosidade não obedece mais à lei de Bragg devido ao efeito de contração-expansão das camadas de baixa e alta porosidade.

Três materiais diferentes foram usados para a passivação da superfície: óxido de silício térmico (SiO_2), ouro (Au) e óxido de titânio (TiO_2). Apesar da camada de passivação, a presença desses elementos resultou em um deslocamento para o azul do PBG. No entanto, no caso do TiO_2 depositado, algumas amostras apresentaram um deslocamento para o vermelho, enquanto em outras o PBG não foi alterado. O deslocamento ao vermelho foi associado à presença de xileno no sol-gel TiO_2 dentro dos poros. O PBG inalterado foi associado à formação de uma fina camada de sol-gel de TiO_2 de vedação dos poros. Após o tratamento térmico, observou-se o típico deslocamento para o azul. Apesar do material de passivação, a espectroscopia rápida de infravermelho de Fourier (FTIR) revela a presença de SiO_2 além das fases Au ou TiO_2 . A análise por espectroscopia de raios-X por dispersão de energia (EDS) mostrou que Au e TiO_2 foram depositados em um gradiente de

concentração profundo, mas com uma distribuição homogênea ao longo da superfície da amostra. A difração de raios X (XRD) mostrou que após o tratamento térmico a 450°C, as fases rutilo e anatase coexistem, com predominância da última. A estabilidade das propriedades ópticas após a passivação foi confirmada por medições das amostras após 20 e 36 semanas de armazenamento. Nenhuma mudança espectral foi observada na posição PBG.

Palavras-chave: Cristal fotônico de silício poroso. Passivação de superfícies porosas. Efeito do etch-stop.

List of Figures

Figure 1 – Classification of photonic crystals.	21
Figure 2 – Natural photonic crystal	22
Figure 3 – Man-made photonic crystals	23
Figure 4 – Derivation of fresnel’s formulae for one planar interface.	24
Figure 5 – Derivation of fresnel’s formulae for two planar interfaces.	24
Figure 6 – Graphical representation of a one-dimensional photonic crystal	26
Figure 7 – Theoretical relation dispersion of a porous silicon multilayer.	30
Figure 8 – Schematic representation of a 1D-PC with microcavity	31
Figure 9 – Experimental setup	32
Figure 10 – Evolution of p^+ porous silicon with current and doping density.	33
Figure 11 – SLIM method for determining the optical thickness from the reflectance spectra in air and ethanol.	36
Figure 12 – Fourier transform spectrum of porous single-layer silicon in air and ethanol	37
Figure 13 – Formation of porous silicon using an etch-stop time of 2 s	40
Figure 14 – SEM images of single layers with low porosity.	43
Figure 15 – Reflectance spectra of low porosity single layer	44
Figure 16 – SEM images of high porosity single layers	46
Figure 17 – Reflectance spectra of high porosity single layer	47
Figure 18 – Optical absorbance of porous silicon single layers	48
Figure 19 – SEM image of fabricated one-dimensional photonic crystal	49
Figure 20 – Comparison of the reflectance spectra of multilayer structures (LH) ¹⁵ and (HL) ¹⁵ for different etch-stop time	50
Figure 21 – Relation dispersion of 1D-PSPC	51
Figure 22 – Optical parameter of photonic crystals for electrolyte type I and etching time I.	53
Figure 23 – Input parameters of 1D-PSPC anodized with electrolyte type I and etching time I.	54
Figure 24 – Comparison of the reflectance spectra with electrolyte type I and type II	55
Figure 25 – SEM image of 1D-PSPC-Mc	56
Figure 26 – Comparison of reflectance spectra of 1D-PSPC-Mc at different etch-stop time using electrolyte type I and time I	57
Figure 27 – Input parameters of 1D-PSPC-Mc anodized with electrolyte type I and etching time I	58

Figure 28 – Reflectance spectra of 1D-PSPC-Mc at different etch-stop time anodized with electrolyte type II and etching time I	59
Figure 29 – Input parameters of 1D-PSPC-Mc anodized with electrolyte type II and etching time I	60
Figure 30 – Reflectance spectra of 1D-PSPC-Mc at different etch-stop times using electrolyte type II and etching time II	61
Figure 31 – Input parameters of 1D-PSPC-Mc anodized with electrolyte type II and etching time II	62
Figure 32 – Comparison of the refractive indices	63
Figure 33 – Reflectivity spectra of 1D-PSPC oxidized in air at different temperatures	64
Figure 34 – Relationship between photonic bandgap width and photonic bandgap center position as a function of oxidation temperature	65
Figure 35 – Calculated dependence of porous silicon oxidation degree with the effective refractive index of PS layers passivated SiO ₂ for various initial porosity.	66
Figure 36 – Comparison of reflectance spectra of single layers with low porosity by Au deposition and thermal annealing.	67
Figure 37 – Comparison of reflectance spectra of high porosity single layer with Au deposition and thermal annealing.	68
Figure 38 – EDS of Au passivated single layers	69
Figure 39 – X ray diffraction pattern of low PS: Au:900°C.	70
Figure 40 – Reflectance spectra of Au passivated 1D-PSPC	70
Figure 41 – EDS of 1D-PSPC: Au	71
Figure 42 – Calculated dependence of the effective refractive index on the wavelength in a system composed of air, gold and porous silicon with an initial porosity of 70%.	72
Figure 43 – Calculated dependence of the degree of oxidation of porous silicon with the effective refractive index of PS layers passivated with Au and SiO ₂ for different initial porosities. The volume fraction of gold is 0.03	73
Figure 44 – X ray diffraction pattern of 1D-PSPC: Au:900°C.	74
Figure 45 – SEM image of a fabricated 1D-PSPC-Mc with the etch-stop	74
Figure 46 – Reflectance spectra of sample S26 for as-prepared porous silicon photonic crystal (black), with physical deposition of Au (yellow) and oxidized at 900°C (red) for 5 minutes.	75
Figure 47 – EDS of 1D-PSPC-Mc passivated with Au	76
Figure 48 – X-ray diffraction pattern of 1D-PSPC-Mc: Au:900°C.	76
Figure 49 – Visual effect of 1D-PSPC-Mc before and after gold incorporation	77
Figure 50 – Reflectance spectra of 1D-PSPC-Mc passivated with TiO ₂ and thermal treatment	77

Figure 51 – Visual effect of 1D-PSPC-Mc passivated with TiO ₂ before and after thermal annealing	79
Figure 52 – λ_c , $\Delta\lambda_c$ and PBG comparison for as-etched 1D-PSPC-Mc, TiO ₂ incorporation and after thermal annealing	80
Figure 53 – Calculated dependence of the effective refractive index with a wavelength in a system composed of air, titanium dioxide, and porous silicon with initial porosity of 70%.	80
Figure 54 – Calculated dependence of porous silicon oxidation degree with the effective refractive index of PS layers passivated with TiO ₂ and SiO ₂ for various initial porosity. The volume fraction of TiO ₂ is 0.138	81
Figure 55 – FTIR of 1D-PSPC-Mc:TiO ₂ and after thermal annealing	81
Figure 56 – EDS of 1D-PSPC-Mc:TiO ₂ :450°C	82
Figure 57 – XRD of 1D-PSPC-Mc:TiO ₂ :450°C	83
Figure 58 – Stability of the optical response of 1D-PSPC-Mc devices	84
Figure 59 – Comparison of FTIR passivated devices with SiO ₂ , Au and TiO ₂	84
Figure 60 – Optical thickness of single PS layers as a function of the refractive index of the organic solvent	86
Figure 61 – Optical thickness of 1D-PSPC-Mc as a function of the refractive index of the organic solvent	86

List of Tables

Table 1 – Chemical composition of electrochemical solvents.	40
Table 2 – Etching times in the formation of porous silicon.	40
Table 3 – Parameters of electrochemical etching in the fabrication of porous silicon structures	41
Table 4 – Optical parameters for low porosity single layers	43
Table 5 – Optical parameters of high porous single layers	47
Table 6 – Input parameters of 1D-PSPC anodized with electrolyte type I and etching time I.	52
Table 7 – Displacement of the physical thickness as a function of the etch-stop time	53
Table 8 – Input parameters of 1D-PSPC anodized with electrolyte type I and etching time I.	54
Table 9 – Input parameters of 1D-PSPC-Mc anodized with electrolyte type I and etching time I	57
Table 10 – Input parameters of 1D-PSPC-Mc anodized with electrolyte type II and etching time I.	59
Table 11 – Input parameters of 1D-PSPC anodized with electrolyte type II and etching time II.	60
Table 12 – Fitted linear values of the thickness curve	62
Table 13 – λ_c position comparison for as-etched 1D-PSPC-Mc, after TiO_2 deposition and thermal annealing	78

List of abbreviations and acronyms

μ	Magnetic permeability
ρ	Charge density
ε	Electric permittivity or dielectric function
\vec{B}	Magnetic induction
\vec{D}	Electric displacement vector
\vec{E}	Electric field
\vec{H}	Magnetic field
\vec{j}	Current density
\vec{k}_B	Bloch wave vector
s	Oxidation degree of silicon
1D-PSPC	One dimensional porous silicon photonic crystal
1D-PSPC-Mc	One dimensional porous silicon photonic crystal with microcavity
BEMA	Bruggeman effective medium approach
CVD	Chemical vapor deposition
DBR	Distributed bragg reflector
EDS	Energy X-ray dispersive
Electrolyte type I	HF:ethanol (3:7)
Electrolyte type II	HF:H ₂ :ethanol (3:3:4)
Etching time I	$t_L = 11.2$ s and $t_H = 7.1$ s
Etching time II	$t_L = 10.9$ s and $t_H = 6.8$ s
FFT	Fast fourier transform
FTIR	Fourier transform infrared spectroscopy
L	Depolarization factor. $L = 0$ (needle), $L = 1/3$ (sphere) and $L = 1$ (pancake)
OT	Optical thickness
PC	Photonic crystal
PGB	Photonic band gap
PL	Photoluminescence
PS	Porous silicon
SCR	Space charge region
SEM	Scanning electron microscopy
TEM	Transmission electron microscopy
TMM	Transfer matrix method
XRD	X-ray diffraction

List of symbols

Λ	Unit cell, $\Lambda = d_L + d_H$
\hat{n}	Complex refractive index, $\hat{n} = n - i\kappa$.
κ	Imaginary part of the complex refractive index, or extinction coefficient
λ_0	Wavelength of the maximum reflectance
λ_c	Position of the transmittance band or microcavity
λ_m	Wavelength of the m-th maximum
ϕ	Light incident angle
ψ	Light refracted angle
ATO	Sb-SnO ₂
Au	Gold
d_c	Physical thickness of the microcavity layer.
d_H	Physical thickness of high porosity layer.
d_L	Physical thickness of low porosity layer.
diH ₂ O ₂	Deionized water
e ⁻	Electrons
h ⁺	Holes inside the silicon
H ₂ O ₂	Hydrogen peroxide
HF	Hydrofluoric acid
HF ₂ ⁻	Hydrofluoric acid ion
n _{eff}	Effective refractive index.
n ₁	Refractive index of the medium where light is transmitted.
n _H	Refractive index of high porosity layer.
n _L	Refractive index of low porosity layer.
NH ₄ OH	Ammonium hydroxide
p	Porosity
p _H	High porosity layer.
p _L	Low porosity layer.
Si	Silicon
SiF ₆ ²⁻	Silicon hexafluoride ions
SiO ₂	Silicon dioxide
TiO ₂	Titanium dioxide

Contents

1	INTRODUCTION	18
2	PHOTONIC CRYSTALS	20
2.1	What is a photonic crystal?	20
2.2	Interaction of light with matter	21
2.2.1	Fresnel's equations	22
2.2.2	Transfer Matrix Method	25
2.2.3	Let there be light: The master equation	27
2.2.4	Band gap structure	28
2.2.5	Photonic crystals with microcavity	29
2.3	Optical properties of porous structures	30
2.3.1	Fundamental of porous silicon: A short review	30
2.3.2	Relationship between porosity and effective refractive index: effective medium approach models	34
2.3.2.1	Maxwell-Garnett Model (MGM)	34
2.3.2.2	Bruggeman Model	35
2.3.2.3	Looyenga's model	35
2.4	Simultaneous determination of porosity and thickness: Spectroscopic Liquid Infiltration Method	35
2.5	Porous structure passivation	37
3	EXPERIMENTAL PROCEDURE	39
3.1	Initial preparation of silicon layers	39
3.2	Preparation of one-dimensional porous silicon photonic crystals	39
4	RESULTS AND DISCUSSIONS	42
4.1	Structural and morphological characterization of single porous silicon	42
4.1.1	Low porosity single layers	42
4.1.2	High porosity single layers	46
4.1.3	FTIR analysis of single layers	48
4.2	Structural and morphological characterization of one-dimensional porous silicon photonic crystal	49
4.2.1	One-dimensional porous silicon photonic crystal using type I and time I	49
4.2.2	Devices yielded using solution II and set time I	54
4.3	Structural and morphological characterization of one-dimensional porous silicon photonic crystal with resonant microcavity	55

4.3.1	Photonic crystals yielded in HF:ethanol (3:7) and set Time I.	55
4.3.2	Photonic crystals yielded in HF:ethanol:H ₂ O (3:4:3) and set Time I.	57
4.3.3	Photonic crystals yielded in HF:ethanol:H ₂ O (3:4:3) and set Time II.	59
4.4	Passivation of the porous silicon structures	62
4.4.1	Passivation by thermal oxidation	63
4.4.2	Passivation by gold nanoparticles deposition	66
4.4.2.1	Single layers	66
4.4.2.2	Multilayers: 1D-Photonic crystals and cavities	69
4.4.3	Passivation by Titanium dioxide: multilayer structures with resonant cavity .	77
4.4.3.1	Complementary analysis for TiO ₂ in multilayers: FTIR, EDS and XRD	79
4.5	Optical response of passivated devices in air and liquid media	85
5	CONCLUSIONS	88

ANNEX 89

ANNEX A – WORKS PRESENTED AT CONFERENCES AND EVENTS 90

BIBLIOGRAPHY 91

1 Introduction

In the last 20 years, interest in the propagation of light through a periodic medium called *photonic crystal*, PC, has increased due to the possibility to manipulate light in ways similar to semiconductors that control electron flow. Whereas in a semiconductor the electron flow is controlled by a periodic electric field displaying the conduction and valence bands, the shaping of light in a photonic crystal is done by a periodicity of the refractive index or physical thickness of the materials, which modifies the dispersion relation of the photon and indicates the available and forbidden photons within the structure, appearing the so-called *photonic band gap* (PBG), brought by constructive interference of reflected waves traveling through the lattice. Tuning the PBG allows reflective and antireflective coating, laser cavity, and functionalized medical devices, it also opens up new technological possibilities in transmission, quantum computing [1, 2, 3] and spintronic [3] where the use of light rather than electrons, enhances the processing velocity and opens the limitations of electron technology. However, a pure optical technology is still under investigation, and for this purpose, the photonic crystal, metamaterials [4][5] and plasmon resonance [6][7][8] are some optimal proposals.

The photonic crystal can be classified according to the dimension periodicity in one-dimensional (1D), two-dimensional (2D), and three-dimensional (3D) structures. In this sense, the main objective of this work was the fabrication of 1D photonic crystals using the technology of porous silicon (PS) due to its fabrication facilities [9][10].

Since a PC is a structure where its refractive index, i.e., dielectric permittivity, varies periodically along the entire structure, a wide range of materials can be considered for fabrication, such as ferromagnetic [11][12], hybridization of polymers [13], metamaterials [14], and Fibonacci sequence [15], to mention few. In this vast universe of materials, silicon is a great candidate not only because it is abundant and cheap, but also because it allows integration with other semiconductor devices using complementary metal-oxide-semiconductor (CMOS) technology. Silicon was already successfully used for the fabrication of one-dimensional silicon-based photonic crystals such as Si/SiO₂, SiO₂/TiO₂, SiO₂/SnO₂, SiO₂/ATO [16][17][18]. Some studies have reported the use of silicon-based photonic structures doped with rare earths (Yb⁺³, Er⁺³) for improving in photoluminescence (PL) properties of different rare-earths, such as Er⁺³, for instance, which has a photo-emission peak at 1.54 μm, open the possibility of the fabrication of silicon-based laser. Thus, the photonic crystal could expand the technological possibilities of information transport, applications where electronically matched systems are limited due to charge and mass carriers.

Although the existence of different methods for the fabrication of silicon-based PCs, in the last years the use of PS as an alternative method has grown rapidly. This rapid rise is associated with its interesting and singular optical properties. For instance, it was found that the PL of porous silicon increases with porosity, whereas the crystallite size defines the light emission wavelength [19].

Although lithography, holography, chemical vapor deposition, molecular beam epitaxy, and other methods have shown excellent results, their main disadvantage is associated with their high production costs and limited access to this handling technology. In counterpart, the production of PCs using electrochemical anodization has proven to be a good low-cost technique. However, some drawbacks such as interface roughness and porosity gradient still need to be solved before commercial application. The cause of these problems has been attributed to the consumption of the HF electrolyte during pore formation. To overcome these drawbacks, the strategy of inclusion of pauses between layers during the anodization process (*etch-stop time*) was earlier proposed by Thönissen et al [20], but a systematic investigation of the effect of this inclusion on the optical and structural properties of 1D-PSPC needs to be investigated.

Thus, this master thesis deals with the systematic research of the optical response of 1D-PSPCs and resonant microcavities (1D-PSPC-Mc) fabricated by using the etch-stop method and the influence of the anodization parameters on the electromagnetic response. This work is divided into five chapters. Chapter 1 presents the current state of the art in the fabrication of porous silicon for photonic devices and their applications. Chapter 2 reviews briefly the history of photonic crystals and introduces the concept of photonic crystals. Then, the theory section explains the pore formation in a silicon substrate by electrochemical route, the propagation of electromagnetic waves in a porous medium, and the models used to describe the dielectric function of thin film media up to multilayers, using Fresnel's equations as a first approximation and the Bruggeman effective medium approximation along with TMM (Transfer matrix method) as a robust model, but with some limitations. Chapter 3 presents the experimental fabrication of a multilayer porous silicon structure using an electrochemical solution of hydrofluoric acid, current density, and anodization time to control the morphological features such as thickness and porosity of the photonic device, as well as the incorporation of the etch-stop method. In Chapter 4, the obtained results and related discussions are presented. Finally, the conclusions and future perspectives of the developed work are presented in Chapter 5.

2 Photonic Crystals: Basic Fundamentals

The propagation of electromagnetic waves in stratified media was originally studied by Lord Rayleigh (1887) as the sum of multiple reflections at each interface. Abelés contributed to the understanding of the optical properties of thin films and multilayered structures by using the transfer matrix [21][22]. Several approaches have been developed to understand the optical response of periodic media. Some of them are band structure analysis [23], finite-difference time-domain method [24], transfer matrix method (TMM), coupled modes, perturbative technique and scattering method [4].

In 1987, John Sajeev [25] investigated the suppression of the density of states in disordered and non-dissipative media, and Yablonovitch [26] worked on the inhibition of spontaneous emission of atoms located in dielectric cavities. Yablonovitch extended earlier work (mainly 1D) to a fully open photon dispersion relation (band gap) in 3D, taking control of light in all directions. This pioneering work was the beginning of a new line of research in optics devoted to the interaction of light with periodic matter, henceforth referred to as *photonic crystals*, whose most important optical feature is the presence of an optical region in which photonic states are forbidden by the periodic structure. This optical region is called the photonic band gap (PBG).

Although this type of structure was initially classified as a metamaterial, because this structure was unknown in nature, posterior research using modern scanning electron microscopy (SEM) showed that this structure can be found in the internal microstructure of the skin, wings, or feathers of chameleons, male peacocks, and fish, resulting in bright and iridescent colors [27][28]. The discovery and understanding of the physical principles and the development of fabrication methods will enable the application of these structures in medicine as bio- and chemosensors. To this end, the photonic structure must be functionalized with organic and biological analytes or even metallic nanoparticles to enhance surface plasmon resonance [29].

2.1 What is a photonic crystal?

In the thin-film physics framework, photonic crystals are interpreted as a stratified medium that exhibits a periodic distribution of its dielectric constant along the entire structure. Depending on how this periodic variation occurs, photonic crystals are classified as one-dimensional (1D), two-dimensional (2D), and three-dimensional (3D) and are shown schematically in Figure 1.

In nature, while some colors are based on molecular pigments, others depend en-

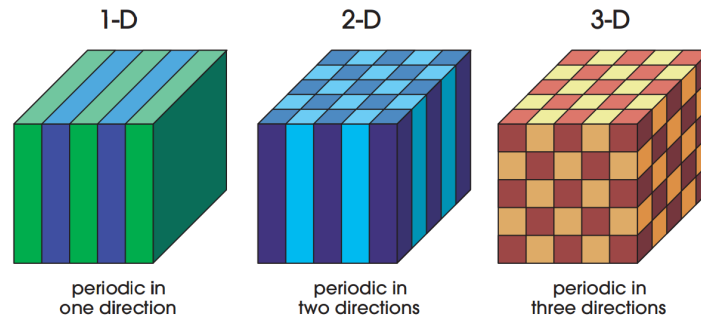


Figure 1 – *Classification of photonic crystals. Each color represents a layer with a different refractive index. Image extracted from [23].*

tirely on the internal structure. The mechanism of such structural colors is the diffraction and reflection of light. While part of the incoming light is transmitted through the structure or absorbed, photons having wavelengths in the order of periodicity undergo constructive interference and thus give rise to the formation of a region with complete reflectance, known as PBG. Figure 2 shows an example of natural periodic nanostructures found in some insects.

To study these types of structures, various techniques have been developed to fabricate nanostructures on the order of nanometers. Some examples of them are electrochemical anodization, lithography, holography, chemical vapor deposition (CVD), molecular beam epitaxy (MBE), inverse opals for the 3D case, and others, resulting in the structures shown in Figure 3. Only the 3D structure exhibits a complete band gap, i.e., forbidden bands in all propagation directions of the photon. However, the 1D photonic crystal exhibits many of the physical phenomena that occur in complex structures, which allows a simple and direct understanding of the subject, besides the fact that a 1D structure is cheaper and easy to fabricate. Nowadays, the developments of different photonic crystal methods fabrication, together with the various methods of passivation and functionalization, enable the fabrication of optical sensors for the detection of biological [33][34] and chemical analytes [35], as well as applications as Bragg filters for the textile industry [36] and optical devices controlled by a magnetic field [37].

2.2 Interaction of light with matter

The interaction between matter and light is perhaps the best-known phenomenon because everything around us interacts with light. This subject has been studied in optical physics in various frameworks. According to classical optics, when light is incoming into the matter, some of it is reflected and some of it is transmitted (refracted). Depending on the optical properties of some materials, light may also be absorbed. If the surface is rough, some of the incident light will be scattered. Thus, the relationship between these

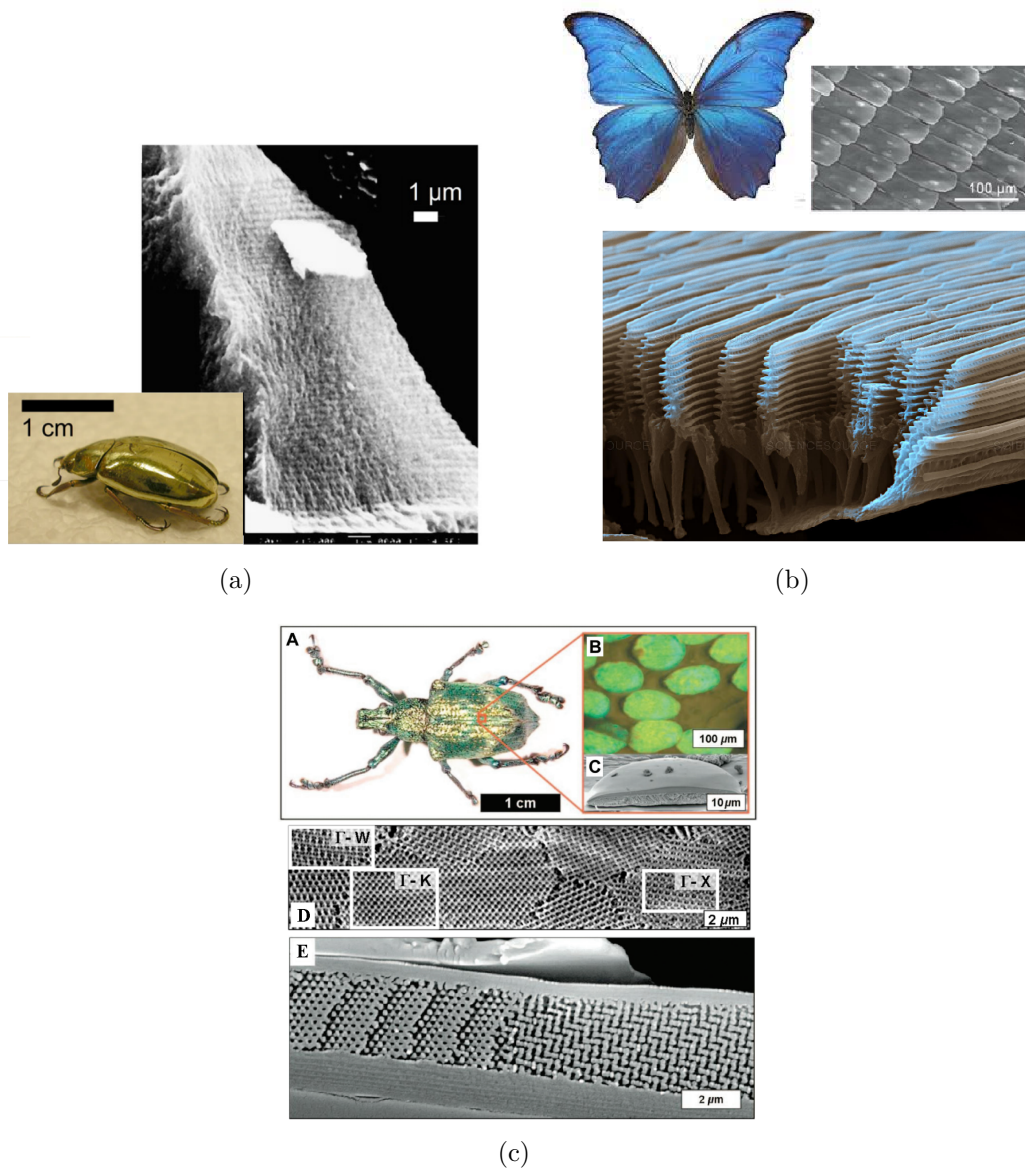


Figure 2 – Examples of natural photonic crystals (a) 1D - the beetle *Chrysina resplendens* shows a metallic gold in its elytra due to a broad band of the Bragg reflector and a rotation of 60° [30] (b) 2D - photograph of *Morpho rhetenor*, and magnified view and TEM micrograph of scale butterfly [27] (c) 3D - *Lamprocyphus augustus*, showing a SEM image of the top view (D) and cross section (E) of weevil wing cases [27][28].

quantities is thus described by

$$T + R + S + A = 1 \quad (2.1)$$

where T, R, S and A are the transmitted, reflected, scattered and absorbed parts of the incident light [38].

2.2.1 Fresnel's equations

For the case of a smooth and well-defined sharp interface, the study of Augustin-Jean Fresnel states that both reflection and transmission phenomena depend strongly

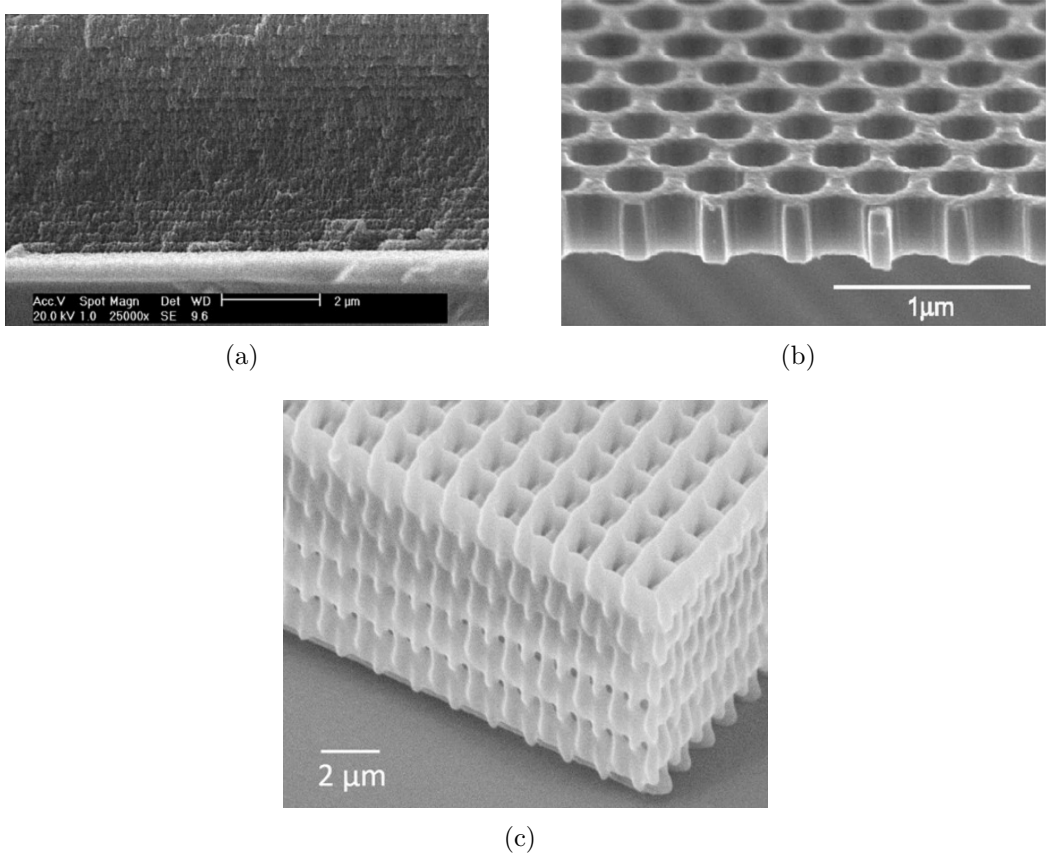


Figure 3 – Example of man-made photonic crystals in 1D, 2D and 3D. (a) Image SEM of 1D porous silicon with unit cell of 222 nm [31], (b) Image SEM of 2D-PC of unit cell 415 nm, (c) Image SEM of 3D-PC built by woodpile technique, unit cell of ≈ 260 nm \times 260 nm \times 960 nm [32].

on the optical properties of the medium in which the light travels and on the angle of incidence (φ). Considering the below schematic representation of the interface (Figure 4), the optical properties of the incident medium are represented by its complex refractive index, denoted by \hat{n}_1 , while \hat{n}_2 stands for the interacting matter. The complex refractive index is defined as $\hat{n}_j = n_j - ik_j$. From Figure 4, the Fresnel relation between \hat{n}_1 and by \hat{n}_2 for the polarization states s and p are described by Equations (2.2) to (2.5). After light-matter interaction, part of the electromagnetic wave propagates parallel to the plane of incidence (s - polarization), while the other part travels perpendicular to the plane of incidence (p - polarization). In Equations (2.2) to (2.5), r_s and t_p are the reflectivity and transmittance for s -polarization and r_p and t_p for p -polarization.

For s -polarization:

$$r_s = \frac{\hat{n}_1 \cos \varphi - \hat{n}_2 \cos \psi}{\hat{n}_1 \cos \varphi + \hat{n}_2 \cos \psi} \quad (2.2)$$

$$t_s = \frac{2\hat{n}_1 \cos \varphi}{\hat{n}_1 \cos \varphi + \hat{n}_2 \cos \psi} \quad (2.3)$$

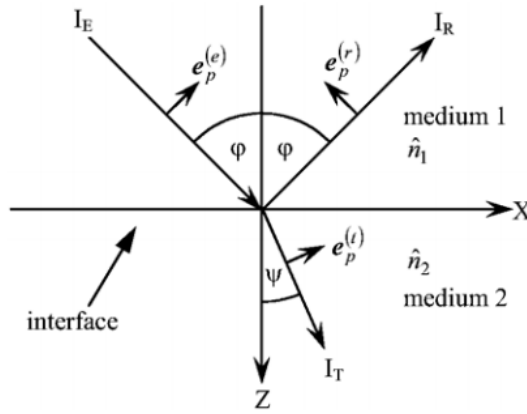


Figure 4 – Schematic representation of the interaction of light in a planar interface.

For p -polarization:

$$r_p = \frac{\hat{n}_2 \cos \varphi - \hat{n}_1 \cos \psi}{\hat{n}_2 \cos \varphi + \hat{n}_1 \cos \psi} \quad (2.4)$$

$$t_p = \frac{2\hat{n}_1 \cos \varphi}{\hat{n}_2 \cos \varphi + \hat{n}_1 \cos \psi} \quad (2.5)$$

From these equations, the reflectance and transmittance are calculated by multiplying the complex part of Fresnel's equation and its conjugate. In the case of reflectance, it can be written as follows

$$R = |r|^2 \quad (2.6)$$

If the light interaction occurs with three subsequent media having well-defined and parallel sharp interfaces, where the middle medium is a thin film with thickness d and complex refractive index, \hat{n}_2 (Figure 5), the reflectivity from this structure is written as

$$r_{123} = \frac{r_{12} + r_{23}e^{-2i\delta}}{1 + r_{12}r_{23}e^{-2i\delta}} \quad (2.7)$$

where the optical phase difference (δ) due to the light interactions is defined by Equation (2.8), λ is the incident light wavelength and d is the physical thickness of the thin film layer. For a non-absorbing film, the complex refractive index is reduced only to the real refractive index.

$$\delta = \frac{2\pi}{\lambda} \hat{n}_{film} d \quad (2.8)$$

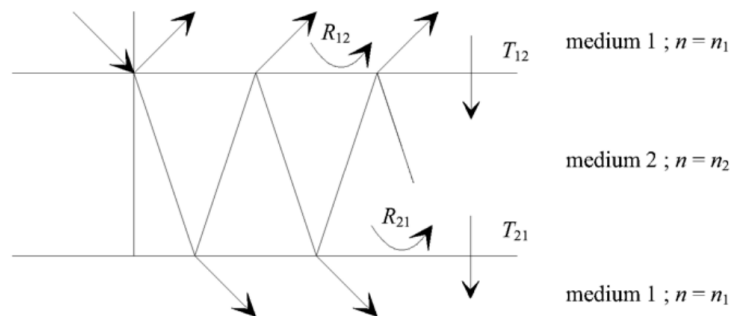


Figure 5 – Schematic representation of the interaction of light in two planar interfaces.

$$\hat{n}_{film} = \sqrt{\hat{n}_2^2 - \hat{n}_1^2 \sin^2 \varphi} \quad (2.9)$$

The n_{film} is a relation dependent on the angle of incidence of the light beam, as Equation (2.9). However, real structures deviate from this optical behaviour due to the roughness of the interfaces [39][40] and the refractive index gradient [31]. The multilayer model [31, 40] was used to correct the effect of the in-depth refractive index gradient, while the effect of the interface roughness, σ , was considered assuming that the roughness is a probabilistic deviation from the smooth interface that obeys a normal distribution. The corrected Fresnel equation is therefore as follows

$$r_{ij}^{corr} = r_{ij} e^{-2k_i k_j \sigma_{ij}^2} \quad (2.10)$$

where r_{ij} is the Fresnel equation for smooth interfaces, and the wave vectors are defined as

$$k_j = \left(\frac{2\pi}{\lambda} \right) \sqrt{n_j^2 - (n_i \sin \phi)^2} \quad (2.11)$$

the subindex i refers to the incident medium and j to all possible media of the system (air, PS and bulk silicon). Similar to Davie's expression for a specular reflection [39], the reflectivity is affected by the roughness and leads to a decrease in the optical response for a layer with a high refractive index at normal incidence.

The cause of both the in-depth refractive index and the roughness of the interfaces are related to the process used to produce the thin films [38]. For thin films of porous silicon (PS), the effective refractive index gradient at depth is related to the formation of a porosity gradient at depth, which in turn is related to difficulties in diffusion of hydrofluoric acid (HF) toward the electrolyte/silicon interface through the porous structure [31, 20]. The work of Huanca and Salcedo [31, 41] shows that this depth porosity gradient is complex at a high concentration of the electrolyte HF and leads to porous structures with low mechanical stability at a low concentration HF.

2.2.2 Transfer Matrix Method

In the thin-film framework, a 1D photonic crystal is treated as a periodic stack of single layers with high and low refractive index, n_H and n_L , and thicknesses d_H and d_L , respectively. In the case of devices made of porous materials, the n_H and n_L are linked to the porosity p_L and p_H , respectively. The optical response of this structure can be well-described by the transfer matrix method (TMM) [38]. TMM consists in expressing the electric field as the sum of incident and reflected plane waves in k-space and rewriting it into a matrix form [42]. This method is limited by the geometry of the structure and the memory capacity of the computer. Nevertheless, TMM is widely used in reflectance calculation, band structure and porosity gradient modeling [43].

The behavior of a single and homogeneous layer with complex refractive index \hat{n} and thickness z for s - polarization is characterized by the M-matrix of Equation (2.12)

$$M(z) = \begin{pmatrix} \cos(k_o \hat{n} z \cos \psi) & -\frac{i}{\hat{n} \cos \psi} \sin(k_o \hat{n} z \cos \psi) \\ -i \hat{n} \cos \psi \sin(k_o \hat{n} z \cos \psi) & \cos(k_o \hat{n} z \cos \psi) \end{pmatrix} \quad (2.12)$$

where $k_o = 2\pi/\lambda$ is the wave vector of the incident beam. For the case of a periodically stratified medium with periodicity $\Lambda = d_1 + d_2$ for a binary system, i.e., a system consisting of two materials with different optical properties, ε_1 and ε_2 , such a system is shown in Figure 6a. The characteristic matrix of the stack is represented in Equation (2.13) as the product of the N-layer constituents of the system.

$$\hat{M}_{stack} = \prod_{j=1}^N \hat{M}_j(z_j) = \begin{pmatrix} m_{11} & m_{12} \\ m_{21} & m_{22} \end{pmatrix} \quad (2.13)$$

To calculate the reflectance of a stack over a substrate with refractive index \hat{n}_s

$$\begin{pmatrix} u \\ v \end{pmatrix} = \begin{pmatrix} m_{11} & m_{12} \\ m_{21} & m_{22} \end{pmatrix} \begin{pmatrix} 1 \\ \hat{n}_s \cos \psi_s \end{pmatrix} \quad (2.14)$$

u stands for the light propagating to above of the structure, and v for the incident light. So the fraction of the light outside the structure is expressed by Equation (2.15)

$$r_s = \frac{u \hat{n}_1 \cos \varphi - v}{u \hat{n}_1 \cos \varphi + v} \quad (2.15)$$

The present work focuses on the s - state of light; for those interested in p -polarization, detailed information can be found in different thin film books, such as that made by Stenzel. [38].

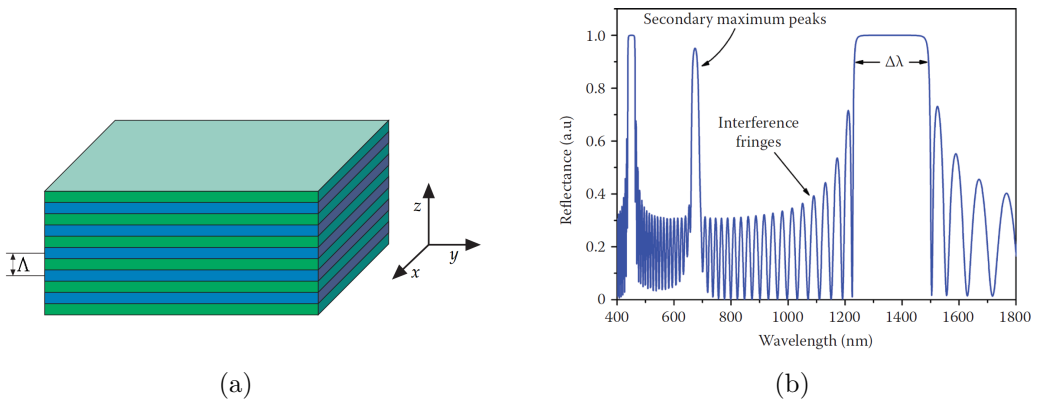


Figure 6 – Graphical representation of the one-dimensional photonic crystal. See the alternating layers, where each color represents a single layer with a particular refractive index. Two consecutive layers conform to a unit cell (Λ). Image taken from [23].

2.2.3 Let there be light: The master equation

The state of classical electromagnetic theory, summarized by Maxwell (1865) in four equations for homogeneous, isotropic, and nonmagnetic materials in the international system of units, is as follows [44]:

$$\nabla \cdot \vec{D}(\mathbf{r}, t) = \rho \quad (2.16)$$

$$\nabla \cdot \vec{B}(\mathbf{r}, t) = 0 \quad (2.17)$$

$$\nabla \times \vec{E}(\mathbf{r}, t) = -\frac{\partial \vec{B}(\mathbf{r}, t)}{\partial t} \quad (2.18)$$

$$\nabla \times \vec{H}(\mathbf{r}, t) = \frac{\partial \vec{D}(\mathbf{r}, t)}{\partial t} + \vec{j} \quad (2.19)$$

where \vec{D} represents the electric displacement vector, \vec{B} is the magnetic induction, \vec{E} is the electric field, and \vec{H} is the magnetic field. And ρ is the charge density and \vec{j} is the current density. In general, the sources and the electromagnetic fields are space and time dependent.

$$\vec{D}(\mathbf{r}, t) = \varepsilon(\mathbf{r})\vec{E}(\mathbf{r}, t) \quad (2.20)$$

$$\vec{B}(\mathbf{r}, t) = \mu(\mathbf{r})\vec{H}(\mathbf{r}, t) \quad (2.21)$$

Equations (2.20) and (2.21) are generally valid for anisotropic media in which the tensors of electric permittivity (ε) and magnetic permeability (μ) have complex elements. When the three eigenvalues of each tensor are equal, the case of linear media holds, and the constitutive equations can be written as harmonics,

$$\vec{F}(\mathbf{r}, t) = \vec{F}(\mathbf{r})e^{-i\omega t} \quad (2.22)$$

where $\vec{F}(\mathbf{r}, t)$ represents any quantity of the presented above. This type of media is also called isotropic. From Maxwell's equations and the constitutive Equations (2.21), after an algebraic treatment, the equation describing the interaction of light with periodic photonic structures is derived and called the master equation:

$$\nabla \times \left(\frac{1}{\varepsilon(\mathbf{r})} \nabla \times \vec{H}(\mathbf{r}) \right) = \left(\frac{\omega}{c} \right)^2 \vec{H}(\mathbf{r}) \quad (2.23)$$

in its differential form also called Helmholtz equation. Equation (2.23) shows an eigenvalue problem entirely in $\vec{H}(\mathbf{r})$, where the light speed in vacuum and the parameters ε_0 and μ_0 are related by $c = 1/\sqrt{\varepsilon_0\mu_0}$. The choice of the magnetic field instead of the electric field to reformulate Maxwell's equations is due to mathematical simplicity, since in this way the operator is Hermitian, which guarantees the real nature of the eigenvalue [23]. The solution of the Equation (2.23) for a given $\varepsilon(\mathbf{r})$ and frequency ω determines the allowable modes or states of the system.

2.2.4 Band gap structure

Since the dielectric function $\varepsilon(\mathbf{r})$ is periodic in space, i.e., $\varepsilon(\mathbf{r}) = \varepsilon(\mathbf{r} + \mathbf{\Lambda})$, where $\mathbf{\Lambda}$ is the lattice vector of the periodic photonic crystal lattice and in the one-dimensional case of a binary system, which consists of dielectric functions ε_1 and ε_2 and thicknesses d_1 and d_2 , the lattice vector is determined by the relation $\Lambda = d_1 + d_2$. With the help of Bloch's theorem [45] and the periodicity of the magnetic field $\vec{H}(\mathbf{r})$ or of any electromagnetic field

$$\vec{H}(\mathbf{r}) = \vec{H}_{k_B, m}(\mathbf{r}) = \vec{u}_{k_B, m}(\mathbf{r})e^{-ik_B d} \quad (2.24)$$

where $\vec{H}(\mathbf{r})$ is characterized by the Bloch wave vector k_B in the first Brillouin zone and a band index m . This vector is a function of frequency, and the functional relation is shown as the dispersion relation in Figure 7. The main characteristic of a photonic crystal is the presence of regions where photonic states are forbidden, i.e. light cannot travel through the periodic structure. These regions are called the photonic bandgap (PBG) and their properties depend on the geometrical characteristics of the unit cell (Λ) and the contrast of the dielectric constant (or refractive index). The position and width of the PBG are determined by solving the master equation in conjunction with Bloch's theorem. After a tedious and exhaustive algebraic handle, the dispersion relation is given by

$$\cos(k_B(\omega)\Lambda) = \cos(k_{1x}d_1)\cos(k_{2x}d_2) - \frac{1}{2}\left(\gamma + \frac{1}{\gamma}\right)\sin(k_{1x}d_1)\sin(k_{2x}d_2) \quad (2.25)$$

where the parameter $\gamma = \frac{k_{1x}}{k_{2x}}$ for the TE mode, and $\gamma = \frac{k_{1x}n_2^2}{k_{2x}n_1^2}$ for the TM mode, and $k_{jx} = \frac{\omega}{c}n_j\cos(\theta_j)$. With $j=1,2$ [46]. The optical behavior of the system is characterized by the Bloch wave, and this behavior can be divided into three regimes:

- $|\cos(k_B(\omega)\Lambda)| < 1 \Leftrightarrow k_B\Lambda \in [0, \pi]$ corresponds to the real k_B in the first Brillouin zone, and the electromagnetic field in the reciprocal space is periodic and a traveling wave function.
- $|\cos(k_B(\omega)\Lambda)| > 1 \Leftrightarrow k_B\Lambda \notin [0, \pi]$ corresponds to an imaginary wave vector defined by $k_B\Lambda = m\pi + ig(\omega)$ and the electromagnetic field in reciprocal space is an evanescent wave function. These are the so-called forbidden bands.
- $\cos(k_B(\omega)\Lambda) = 1 \Leftrightarrow k_B\Lambda = m\pi$; $E(z, k_B)$ is a periodic function of period 2^{nd} with the special property of being d-shifted skew-symmetric, $E(z + \Lambda, k_B) = E(z, k_B)$ [46].

The presence of a PBG and its value depends on the refractive indices of the H, and L layers. For the case of a constant refractive index, the PBG is shown in Figure 7a.

The light-matter interaction was investigated by different approaches [23][47][4]. In the case of omnidirectional propagation of light, the thin-film stacking approach, described

in detail by [47], shows that the PBG edges can be obtained by solving Equation (2.26)

$$\frac{\cos(\delta_H + \delta_L) - \rho^2 \cos(\delta_H - \delta_L)}{1 - \rho^2} = -1 \quad (2.26)$$

where δ_i refers to the optical phase of the H and L layers ($i = H, L$), defined as

$$\delta_i = \frac{2\pi}{\lambda} n_i d_i \quad (2.27)$$

For the case of a porous structure of PS, n_i is the so-called effective refractive index of the porous silicon layer and d_i is the physical thickness of the i -th porous layer. The n_i depends on the angle of incidence of the beam and the refractive index of the incident medium, as given by Equation 2.9 For the case in which $\delta_H = \delta_L$, the optical thickness (OT) of the layer with low and high refractive index equals $\lambda/4$. For this condition, the main PBG width can be written as [48]

$$\frac{\Delta\lambda}{\lambda_0} = \frac{4}{\pi} \cdot \arcsin\left(\frac{n_L - n_H}{n_L + n_H}\right) \quad (2.28)$$

λ_0 is the wavelength at the center of the photonic band (or gap, in the case of photonic band structure). Equation (2.28) provides a better understanding of the relationship between gap-mid and gap ratio ($\Delta\lambda/\lambda_0$), and n_L and n_H are the upper and lower limits of the 1D bandgap of Figure 7. To optimize the widest bandgap, Xifré [43] found that it depends more strongly on the refractive index at lower porosity (n_L), and a decrease in the refractive index at higher porosity (n_H) does not necessarily lead to an increase in the ratio of gap/gap-mid. For perpendicular incidence, Equation (2.29), known in thin film theory as Bragg's law, applies [47][38]

$$\lambda_0 = 2(n_H d_H + n_L d_L) \quad (2.29)$$

2.2.5 Photonic crystals with microcavity

Another interesting structure consists of two distributed Bragg reflectors (DBRs), one upper and one lower, separated by a defect layer, also called a microcavity (Figure 8a). Usually, the geometrical and optical features of this microcavity differ from those of the H and L layers to break the original periodicity of the photonic crystal. From the point of view of light-matter interaction, the introduction of this microcavity is comparable to the doping process in semiconductor physics, since this defect layer allows the incorporation of photonic states into the PBG. The presence of this aperiodic layer enables a unique behavior of light that depends on the refractive index: If its refractive index is comparable to that of H-layers (high porosity), it behaves like a resonant cavity, but if it is an L-layer (low porosity or high refractive index), this cavity acts like a waveguide.

When an incident light beam interacts with the defect layer, it is absorbed by the electrons of the defect layer and then re-emitted with lower energy, being confined by the

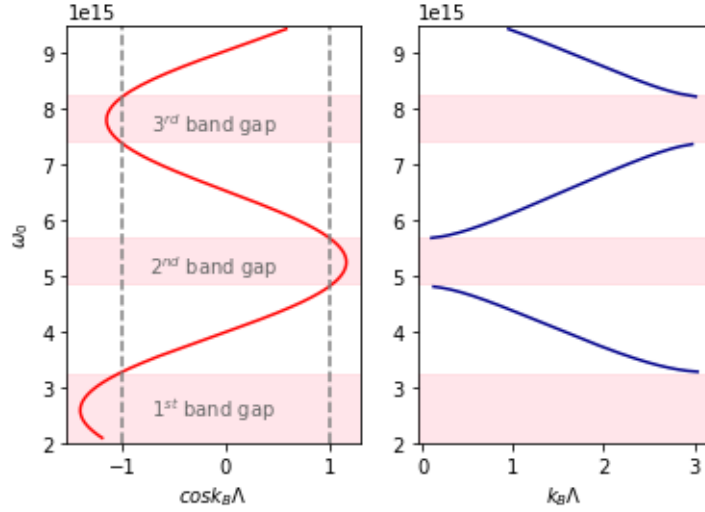


Figure 7 – Theoretical results of the relation dispersion for a porous silicon multilayer structure with thicknesses 150 nm and 40 nm, and real effective refractive index. $n_1 = 3.6$ and $n_2 = 1.45$. The values outside the limits marked by the dashed gray lines are represented in the dispersion relation as the forbidden bands.

microcavity in a quantum well, creating available states. The microcavities are integrated into the periodic structure of the photonic crystal and serve to confine the photons in this layer. According to the work of Torres [49], using a silicon-based photonic structure, a strong coupling phenomenon with the trapped photons is observed as a consequence of this interaction. Conversely, this interaction should lead to the formation of a quasiparticle called an exciton.

In Figure 8a is shown a schematic representation of a 1D-PC with a microcavity. The theoretical reflectance spectrum in Figure 8b shows the effect of the microcavity on the optical response by creating a narrow transmission fringe in the centre of the photonic band. This transmission fringe (λ_c) can be tuned by the thickness (d_c) or refractive index (n_c) of the defect layer as follows in Equation (2.30)

$$\lambda_c = 2d_c \sqrt{n_c^2 - n_0^2 \sin^2 \theta} \quad (2.30)$$

2.3 Optical properties of porous structures

2.3.1 Fundamental of porous silicon: A short review

Matter can also be found in porous form. Some porous structures are made intentionally, and various methods are used to achieve this goal, such as electrochemical processes, chemical vapor deposition, and so on [50][51][29][52]. Among the numerous porous materials, porous silicon is the most studied nowadays because of its potential application in photonic devices [17][18]. Various strategies have been used to fabricate

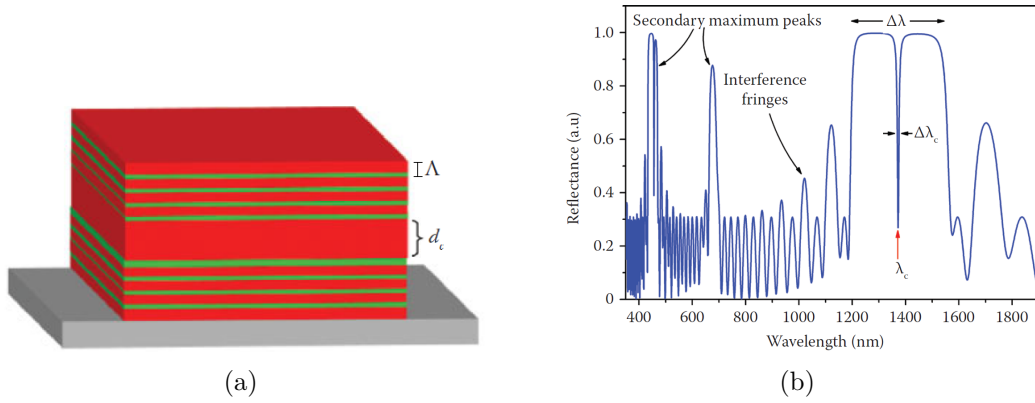


Figure 8 – (a) Graphic depict of a Bragg mirror with an aperiodic layer inclusion in the periodic structure (b) Theoretical reflectance spectrum of such a Bragg mirror with the aperiodic layer.

PS, but the most common is the anodization process [9][51]. The structural and morphological properties of PS and consequently the optical properties are strongly dependent on these characteristics. Since this work aims to produce multilayers, it is of interest to know the factors that influence the thickness and the porosity. From the literature it is found that many authors [41][50][9] point out that both the thickness and the porosity strongly depend on the electrolyte and substrate properties, as well as on the electrochemical parameters such as crystallographic orientation, doping type and degree, interface states; among the external parameters, the solvent type and concentration, viscosity, pH, current density, etching time, and stirring are important for the electrolytes. The mechanism of porous silicon formation is briefly explained below.

Pore formation mechanism

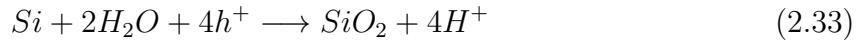
Silicon is thermodynamically unstable in air and water, for which it forms oxygen bounds,



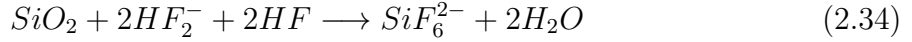
Only SiO_2 is affected by HF and not silicon, so anodization bias is required to achieve porous formation. Pore formation occurs in two regimes with different dissolution valence. The dissolution valence is defined as the ratio of exchanged charge carriers per dissolved silicon atom. In the anodic regime, there is a migration of holes from the silicon to the front side of the silicon, and a migration of electrons from the electrolyte to the interface. The divalent dissolution of silicon is described by Equation (2.32), where a simple substitution of silicon in the electrolyte is dissolved as SiF_6^{2-} . Hydrogen gas evolves in this regime.



In the second anodic regime, tetravalent dissolution occurs, as in Equation 2.33, where four holes are involved in the reaction and the silicon is anodically oxidized.



Thereby HF can freely react with silicon dioxide to dissolve silicon:



The hydrofluoric acid ion (HF_2^-) is a strongly corrosive acid that is considered an important additive in the formation of porous silicon, dissolving the insulating oxide that would otherwise stall the electrochemical corrosion reaction [9]. This results in silicon nanocrystallites exhibiting photoluminescence at room temperature, whereas bulk crystalline silicon does not have this property due to its indirect band gap, which prevents radiative recombination of electrons and holes. Despite the importance of holes in pore formation, the final structure is determined by other parameters related to the type of electrolyte composition as well as substrate characteristics (type, doping density, and crystallographic orientation) [9][50]. The morphology of the pores shows a dependence on the doping level, current density and solvent concentration, which has been studied by many authors [53]. As Figure 10 shows, the porosity increases with increasing current density and decreases with HF concentration for p-type Si.

Porosity

The optical properties of PS have been extensively studied because of their promising applications. Experimental observations by various research groups [53][54] have shown that the main parameter defining not only the physical but also the chemical properties is related to the porosity of the porous layer [55][56]. By definition, porosity describes the ratio between the effective volume of the porous layer divided by the total volume of the sample [9]. Although porosity is the main factor determining the PS properties,

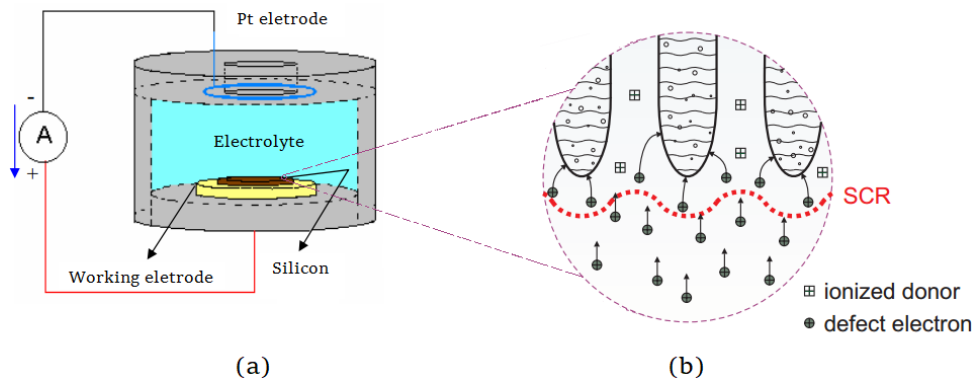


Figure 9 – (a) Schematic representation of the electrochemical etching of silicon. The front side is in contact with the electrolyte. (b) A magnified view of pore formation in the space charge region (SCR).

the geometric characteristics of the pores, as well as the shape and remaining silicon size, called crystallites, are crucial factors in changing the properties of PS. For example, in microporous structures, where the size of the pores and crystallites are on the order of a few nanometers, the phenomenon of photoluminescence (PL) is observed even at room temperature [57][58]. Since silicon is an indirect band semiconductor, one of the most accepted explanatory models is the effect of quantum confinement related to the small dimensions of the crystallites [59]. According to the quantum model, PS is considered as a disordered arrangement of undulating quantum wires in which the excitons are all confined, and the PL emission is attributed to the recombinations of electrons trapped in dangling bonds formed on the surfaces of the Si nanocrystals. In this case, the importance of the nanocrystallite size is reflected in the PL peak shift from 1.14 to 2.2 eV [58][57].

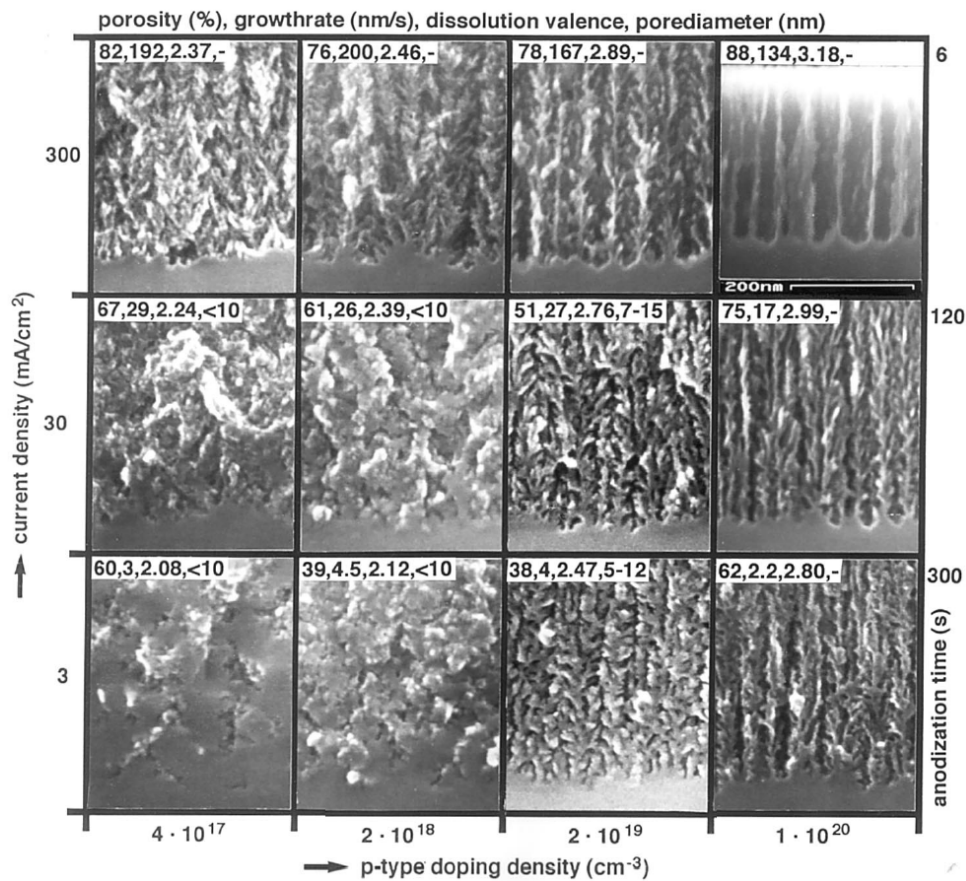


Figure 10 – Scanning electron micrographs of the interface between bulk silicon and porous silicon for p-type doped [100] silicon electrodes anodized galvanostatically in ethanoic acid HF. Image taken from [53].

In structures with a pore size on the micrometric scale, strong light absorption is observed [60][59]. For example, if the porous structures shown in Figure 10 have different optical and electrical response with the same porosity and thickness, this difference is due to their different porous morphology. These results show that, despite the importance of porosity in changing the optical properties of PS, another factor that must be considered for a complete description of the optical properties is associated with the pore morphology.

Regarding the geometrical characteristics of pores, the size of pores is defined by the International Union of Pure and Applied Chemistry (IUPAC) [61]. Thus, structures with pores smaller than 2 nm in diameter are called "micropores," while structures with pore sizes between 2 nm and 50 nm are called "mesopores". If the pore size is larger than 50 nm, the structure is called "macropores". However, in practice, systems in which the pore size is on the order of a few hundred nanometers are called mesopores. In this type of system, the most important factor for changing the PS properties is primarily the porosity. Besides the physical thickness, porosity is the most important parameter for defining the PS optical properties. Since the as-etched porous structure consists only of silicon and voids, the effective refractive index, n_{PS} , is determined by the fraction of silicon and voids (porosity). Various models have been proposed to calculate this refractive index, some of which are briefly described in the next section.

2.3.2 Relationship between porosity and effective refractive index: effective medium approach models

Models describing the macroscopic properties of a porous material are based on certain parameters such as the volume fraction (porosity) and the dielectric function of the materials of which it is composed. Effective medium approximation (EMA) models such as Maxwell-Garnett, Bruggeman, and Looyenga models are commonly used in reflectance modeling of one-dimensional structures because they reduce the number of adjustable parameters that are included in the modeling program suitable for the 1D-PS structure. On the other hand, Bergmann and models are commonly used for reflectance modeling of PS structures. The dielectric function of a porous film (ε_{eff}) is composed of the matrix host, which in our case is silicon-based, and the dielectric function of the medium filling the pores (in many cases air).

2.3.2.1 Maxwell-Garnett Model (MGM)

The Maxwell-Garnett model [62] is based on metallic spherical inclusions labeled as j immersed in a homogeneous background or host. The inclusions are randomly arranged and are described by a system of isolated particles that do not touch. In the case of two phases where the host is a dielectric material, the MGM evolves well for large volume spheres [57] using the following equation

$$\frac{\varepsilon_{eff} - \varepsilon_{host}}{\varepsilon_{eff} + 2\varepsilon_{host}} = (1 - p) \frac{\varepsilon_j - \varepsilon_{host}}{\varepsilon_j + 2\varepsilon_{host}} \quad (2.35)$$

the ε_j , ε_{host} and ε_{eff} are the inclusion, the host (silicon), and the effective dielectric constant of the system.

2.3.2.2 Bruggeman Model

Also called the Bruggeman Effective Medium Approximation (BEMA), the method is described by a dense mixture of percolated particles, and its application in PS films is well adapted for porosities below 66% [53][57]. Equation (2.36) expresses a generalized form of the relationship between the dielectric permittivities and the morphological features of the pores.

$$\sum_j p_j \frac{\varepsilon_j - \varepsilon_{eff}}{\varepsilon_{eff} + (\varepsilon_j - \varepsilon_{eff})L} = 0 \quad (2.36)$$

where ε_j is the dielectric permittivity of the j -th particle embedded in the host and L is the depolarization factor that depends on the geometric shape of the inclusion, in particular for $L=0$ (needle), $L=1/3$ (sphere), and $L=1$ (pancake).

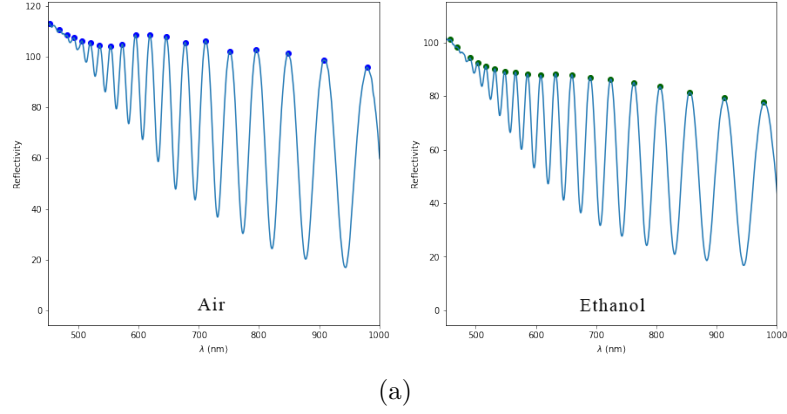
2.3.2.3 Looyenga's model

This model applies to homogeneous mixtures where the shape or boundaries need not be considered [63], but is limited to high porosity media [41]. This model is defined by:

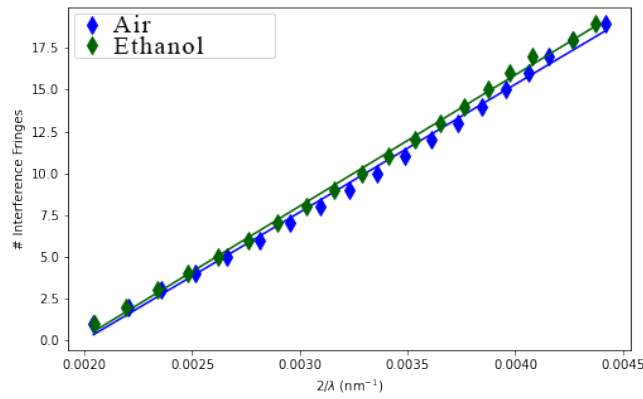
$$\varepsilon_{eff}^{1/3} = p\varepsilon_j^{1/3} + (1-p)\varepsilon_{host}^{1/3} \quad (2.37)$$

2.4 Simultaneous determination of porosity and thickness: Spectroscopic Liquid Infiltration Method

The literature on porous silicon is rich in the current state-of-art, and various methods for measuring thickness and porosity have been reported. Perhaps the most common methods for measuring thickness and porosity are scanning electron microscopy, profilometry, gravimetry, and so forth [64][65][9]. The major drawback of these techniques is their destructive nature. In particular, measuring porosity using the gas adsorption method requires large amounts of PS samples, making this method tedious and slow [66]. An alternative to the simultaneous calculation of porosity and thickness is the method of fitting reflectance spectra. However, the accuracy and speed of this procedure is related to the model used for the fitting. Typically, models based on the effective medium approach are used to calculate the effective refractive index of the porous structure, as summarized in the previous section. In a relatively recent work, linking reflectance measurements in air and in a liquid solution with a known refractive index together with a model based on EMA was proposed to simultaneously measure the thickness and porosity of PS single layers [50][67]. The main advantage of this method is its non-destructive character and was named Spectroscopy of Liquid Infiltration Method (SLIM). For this purpose, the optical thickness of the PS layer in air, OT_{air} , and in liquid, OT_{liq} , is obtained from the reflectance spectra by linear fitting of the relations between the inverse of the spectral



(a)



(b)

Figure 11 – (a) Reflectance spectra recorded in air and in ethanol as organic solvent on a single-layer porous silicon sample. (b) Plot of the number of integer fringes as a function of wavelength at each position where they were recorded.

position of the maximum interference fringes, λ_m , and the number of these maxima, $m = 1, 2, \dots$ (Equation 2.38), as shown in Figure 11.

$$m = 2 \frac{OT_j}{\lambda_m} \quad (2.38)$$

where $OT_j = n_{PS,j} d_{PS,j}$ is the optical thickness defined by the effective refractive index, $n_{PS,j}$, and thickness of the porous layer, $d_{PS,j}$, in j -th environment ($j = \text{air, liquid}$). The porosity and thickness are estimated by solving the system given by the Equations (2.39) and (2.40).

$$f(p, \varepsilon_{Si}, \varepsilon_{air}, OT_{air}/d_{PS}, L) = 0 \quad (2.39)$$

$$f(p, \varepsilon_{Si}, \varepsilon_{liq}, OT_{liq}/d_{PS}, L) = 0 \quad (2.40)$$

where the function $f(p, \varepsilon_{Si}, \varepsilon_j, OT_j/d_{PS}, L)$ is an arbitrary EMA model for calculating porosity (p).

Another way to determine the OT is by the fast Fourier transform (FFT). However, the spectrum of the reflectance data must first be equally spaced. Cubic spline

interpolation must be performed, and the data must be in frequency units. The resulting FFT signal is a plot where the x-axis indicates the effective optical thickness, $2n_{eff}d$, where n_{eff} and d are the effective refractive index and physical thickness of the porous layer, respectively. Figure 12 shows the FFT signal, where the x-axis represents the optical thickness [9]. Although both methods are simple and useful for calculating OT_j from the reflectance spectrum, the main drawback of both methods is that the value OT represents only the mean OT. For an accurate analysis, the wavelength dependence of OT must be taken into account.

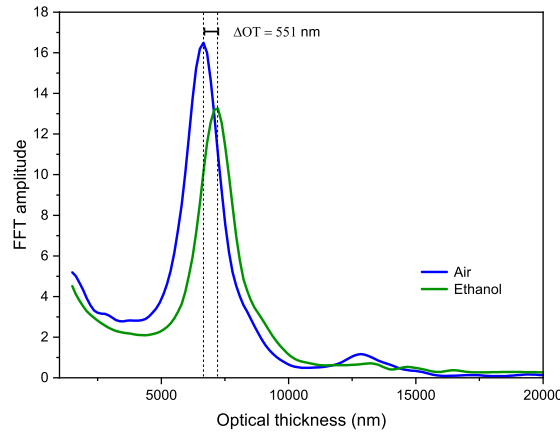


Figure 12 – *Fourier transform spectrum of a p^+ type porous single-layer silicon measured in air (blue) and ethanol (green) in the range of the reflectance spectrum from 500 nm to 1075 nm. The optical thickness of the sample in air is 6655 nm and in ethanol 7206 nm. The FFT signal was obtained from Figure 11a.*

2.5 Porous structure passivation

The porous silicon surface is chemically reactive to bound to oxygen or water, and reacts spontaneously to form an oxide layer [9] that uncontrollably alters its original optical properties. To control this irreversible effect, some coating techniques have been used as passivation methods. Although an initial proposal changes the optical and chemical properties of PS, the idea is to promote an invariant structure with stable optical and chemical properties. For example, various techniques such as thermal oxidation, carbonization and metallization are used [68][69][70][71].

In the particular case of thermal oxidation, the decrease in silicon leads to an increase in the amount of SiO_2 due to the deformation of the lattice caused by the stress and strain in the SiO_2 formation [72]. The temperature changes the pore morphology from small interconnections in the microstructure to elongated, spherical and faceted pores with increasing temperature, also the time dependence of the pores in the annealing process develops the same pore contraction [73]. The effect of oxidation in 1D-PSPC or 1D-PSPC-Mc is evidenced by the blue shift of photonic band gap or resonance peak, the shift is

inversely related to the volume fractions of oxidized silicon and oxidation temperature [74].

3 Experimental procedure

In this chapter, the construction of a one-dimensional photonic crystal based on mesoporous silicon (PS) using two types of electrochemical solutions and different etching times for multiple etch-stop times at constant current density is described in detail.

3.1 Initial preparation of silicon layers

Highly doped silicon wafers with thickness of $500 \mu\text{m} \pm 10 \mu\text{m}$ with crystallographic orientation (100) and $1 \text{ m}\Omega\cdot\text{cm} - 5 \text{ m}\Omega\cdot\text{cm}$ resistivity were used. The silicon was doped with boron at a concentration of $10^{19}\text{cm}^{-3} - 10^{20}\text{cm}^{-3}$ [75] to obtain a p^+ type silicon involved in the formation of porous material.

Before the etching process, it's very important to perform an initial cleaning of the silicon wafer to avoid impurities. First, a chemical attack with $\text{H}_2\text{SO}_4 : \text{H}_2\text{O} : \text{H}_2\text{O}_2$ with ratios of (3:1:1) was performed at 80°C for 10 minutes to remove organic impurities, followed by a second cleaning with $\text{NH}_4\text{OH} : \text{H}_2\text{O} : \text{H}_2\text{O}_2$ with ratios of (1:5:1) at 70°C for 10 minutes.

3.2 Preparation of one-dimensional porous silicon photonic crystals

After chemical cleaning, the silicon substrate was immediately placed in the single electrochemical cell, as shown in Figure 9a. Then the electrochemical cell was filled with the electrochemical solution, using one of the following types: Solution type I (HF:ethanol (3:7)) and Solution type II (HF:H₂O:ethanol (3:3:4)). In these solutions, the HF was diluted with ethanol to obtain HF highly concentrated (48%), while the H₂O used refers to deionized water. The use of these solutions was decided because they are suitable to minimize the inhomogeneities in-depth associated with the surfactant effect of ethanol in solution type I, while the addition of water (solution type II) allows the formation of mechanically robust porous structures, although the surfactant effect is compromised. These solutions are summarized in Table 1, while Table 2 corresponds to the etching time for the formation of the high porosity layer (t_H) and the low porosity layer (t_L). These are the results of a previous study where the etching rate was measured in single layers with high and low porosity.

The formation of a one-dimensional Bragg mirror occurs through periodic changes in refractive index associated with a periodic stack of layers having low (L) and high (H) porosity. For its formation, a periodic current density of low and high intensity is applied

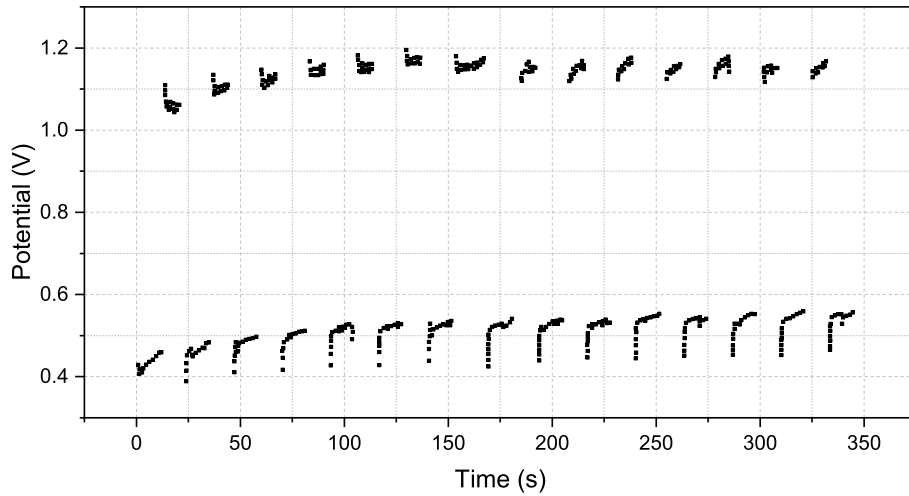


Figure 13 – Formation of porous silicon using the etch-stop time method showing time dependence of current density for 1D-PSPC-Mc with 2 s of pause (S45).

during anodization. For the devices here produced, the applied current density was (j_H) of 50 mA/cm^2 to form the H layers, whereas for the L layers, the current density (j_L) was 5 mA/cm^2 . To produce PS with a microcavity, the thickness of the defect layer was set to $d_C = 2d_H$. Besides, the etch-stop method was carried out by including a pause time, i.e. a stop of the current flux, immediately after the formation of a single layer (L or H).

Pore formation during anodization was performed using an AUTOLAB potentiostat, where the etching parameters (etching time, etch-stop time, and current density) were controlled by NOVA 2.1.4 software. The Stellarnet Black Comet spectrometer recorded the reflectance spectra in a wavelength range from 350 to 1080 nm.

Table 1 – Chemical composition of electrochemical solvents.

Type	Composition	Ratio
I	HF:ethanol	(3:7)
II	HF:H ₂ O:ethanol	(3:3:4)

Table 2 – Etching times in the formation of porous silicon.

Time	t_L	t_H
I	11.2 s	7.1 s
II	10.9 s	6.8 s

To achieve the chemical and physical properties stability, the samples were passivated with three different materials. Since thermal oxidation was the simplest method, thermal SiO₂ was used as the first passivation layer. In this sense, the as-etched 1D-PSPCs were thermally annealed in air environment for 5 minutes. On the other hand, a set of 1D-PSPC-Mc was covered with a thin Au layer (60 nm nominal thickness) deposited

by sputtering at a rate of 1 nm/s. Subsequently, this set was thermally annealed in an air environment at 900°C for 5 minutes. This passivation procedure was also extended to single-layer structures in this case. Finally, the third set of samples were coated with TiO₂ using the sol-gel method; the detailed procedure can be found elsewhere in [76]. Briefly, TiO₂ was prepared by the inverted micelle method by mixing 0.3 mol/l Triton X-100, 0.6 mol/l deionized water, 30 ml xylene, and 0.5 mol/l titanium butoxide (IV); all these products were purchased from Sigma Aldrich. The TiO₂ was introduced into the porous structure by immersing the above samples for one week, after which their optical response was measured. Then, these samples were annealed at 450°C for 15 minutes to calcine the organic compounds of the gel solution and promote better diffusion of TiO₂ in the pores.

Table 3 – Parameters of electrochemical etching in the fabrication of porous silicon structures

Sample ID	Structure type	j_L	j_H	j_C	Etching time (s)	Pause (s)	Electrolyte
S14	Single layer (L)	5	-	-	900	0	Type I
S15	Single layer (L)	5	-	-	$t_1=420$ $t_2=480$	10	Type I
S34	Single layer (L)	5	-	-	900	0	Type II
S16	Single layer (H)	-	50	-	300	0	Type I
S17	Single layer (H)	-	50	-	$t_1=120$ $t_2=180$	10	Type I
S35	Single layer (H)	-	50	-	300	0	Type II
S6	(LH) ¹⁵	5	50	-	Time I	0	Type I
S12	(LH) ¹⁵	5	50	-	Time I	5	Type I
S22	(LH) ¹⁵	5	50	-	Time I	8	Type I
S5	(LH) ¹⁵	5	50	-	Time I	10	Type I
S7	(HL) ¹⁵	5	50	-	Time I	0	Type I
S8	(HL) ¹⁵	5	50	-	Time I	10	Type I
S27	(HL) ¹⁵	5	50	-	Time I	5	Type I
S36	(HL) ¹⁵	5	50	-	Time I	5	Type II
S33	(LH) ⁷ (HL) ⁸	5	50	50	Time I	0	Type I
S32	(LH) ⁷ (HL) ⁸	5	50	50 ^a	Time I	3	Type I
S31	(LH) ⁷ (HL) ⁸	5	50	50*	Time I	5	Type I
S24	(LH) ⁷ (HL) ⁸	5	50	50*	Time I	8	Type I
S39	(LH) ⁷ (HL) ⁸	5	50	50	Time I	0	Type II
S37	(LH) ⁷ (HL) ⁸	5	50	50	Time I	3	Type II
S38	(LH) ⁷ (HL) ⁸	5	50	50	Time I	5	Type II
S40	(LH) ⁷ (HL) ⁸	5	50	50	Time II	0	Type II
S45	(LH) ⁷ (HL) ⁸	5	50	50	Time II	2	Type II
S42	(LH) ⁷ (HL) ⁸	5	50	50	Time II	4	Type II
S43	(LH) ⁷ (HL) ⁸	5	50	50	Time II	6	Type II
S44	(LH) ⁷ (HL) ⁸	5	50	50	Time II	8	Type II

^a A pause was applied after a corrosion time t_H .

4 Results and Discussions

As mentioned above, the structural and geometrical characteristics of the porous layers are determining parameters of PS optical properties, which, in turn, they depend on the electrochemical parameters during anodization. For given substrate and electrolyte characteristics, the PS thickness is controlled by the anodization time, but as pore depth increases, the concentration of HF in the electrolyte decreases [77][50] due to waste chemicals during silicon etching, such as the generation of bubbles of H_2 , silicon hexafluoride ions SiF_6^{2-} , and SiO_2 , which prevent diffusion of HF. Previous observations show that another important factor for the HF variation at the etching front is associated with HF consumption due to silicon dissolution for pore formation [20]. Therefore, to reduce these drawbacks, an etch-stop (pause during anodization) was introduced during anodization. The structural and morphological changes due to this etch-stop were investigated by reflectance spectroscopy studies in the range of 400 to 1100 nm. This study was performed on different PS structures (single layer, multilayer and microcavity structures) prepared with different etching times and two electrochemical solvents. Details are described in this section.

4.1 Structural and morphological characterization of single porous silicon

To investigate the effect of the pause (etch-stop) in PS, two sets of single-layer devices were fabricated; the first having Low porosity and the second with high porosity.

4.1.1 Low porosity single layers

Three single-layer samples with the same electrochemical parameters were prepared for the L-porosity devices: A current density of 5.0 mA/cm^2 and an etching time of 900 s. The sample without the etch-stop was denoted as S14, immersed in electrolyte type I, and S34, engaged in electrolyte type II. S15, on the other hand, represents the sample that was provided with an etch-stop time of 10 s. For the latter sample, the total etching time (900 s) was divided into a first etch of 420 s, followed by a pause of 10 s, and a second etch of 480 s.

Figure 14 shows the cross-sectional images SEM of samples S14, S15, and S34. Using these images, the physical thickness was measured and determined to be 2583 nm, 2834 nm, and 2636 nm, respectively, as summarized in Table 4. These values were also measured using two other methods based on optical reflectance measurements to gain

additional insight into the effects of pause on porosity and thickness. The first method was the SLIM, and the second was the fitting procedure of the reflectance spectra of these samples. The optical reflectance of the samples, measured in air and at room temperature, is shown in Figure 15a. In this figure, the etch-stop effect is clearly visible as the reflectance spectrum of S15 (red open circles) appears shifted with respect to S14 (black open circles), while the reflectance spectrum also appears shifted upon the addition of H₂O to the electrolyte (S34). This fact is better visualized by Reflective Interferometric Fourier Transform spectroscopy (RIFTS) in Figure 15b, data obtained by Fourier transform (FFT - Fast Fourier Transform) from the experimental reflectance spectra.

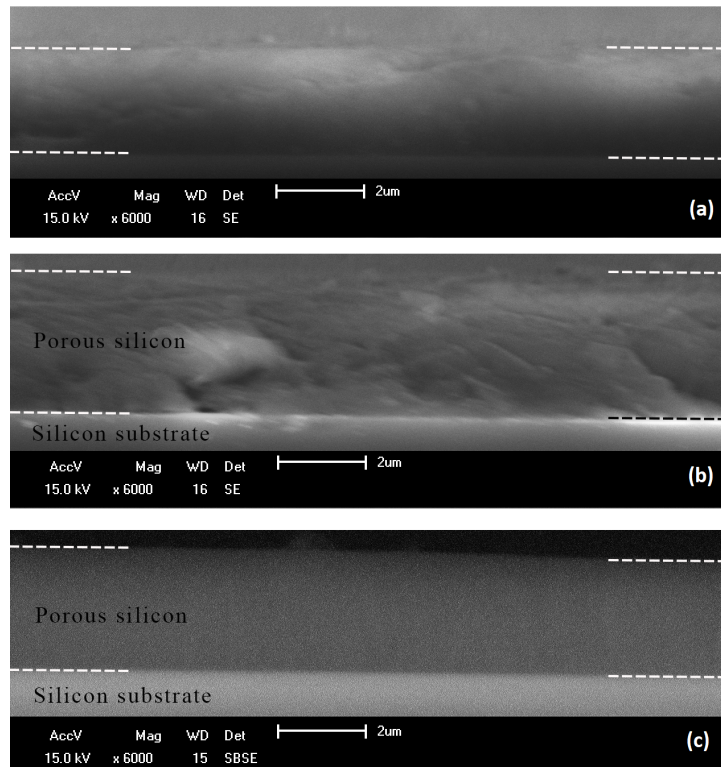


Figure 14 – Scanning electron micrographs of single layers with low porosity (a) S14, (b) S15, and (c) S34.

In Figure 15b, the x-axis of the FFT diagram refers to the position of the optical thickness, $OT = n_{PS}d_{PS}$, where n_{PS} and d_{PS} are the effective refractive index and thickness of the

Table 4 – Optical parameters of low single layers. For the SLIM and fresnel procedures, the BEMA spheres were used.

	Etch-stop time (s)	Electrolyte	Thickness (nm)			Porosity (%)		
			SEM	SLIM	Fresnel	SEM ^a	SLIM	Fresnel
S14	0	Type I	2583 ± 79	2855	2584	63.4	57.5	64.3
S15	10	Type I	2834 ± 125	2885	2638	62.9	56.3	62.7
S34	0	Type II	2636 ± 79	3661	2900	59.0	60.0	59.0

^a The porosity value of SEM was fitted by fresnel.

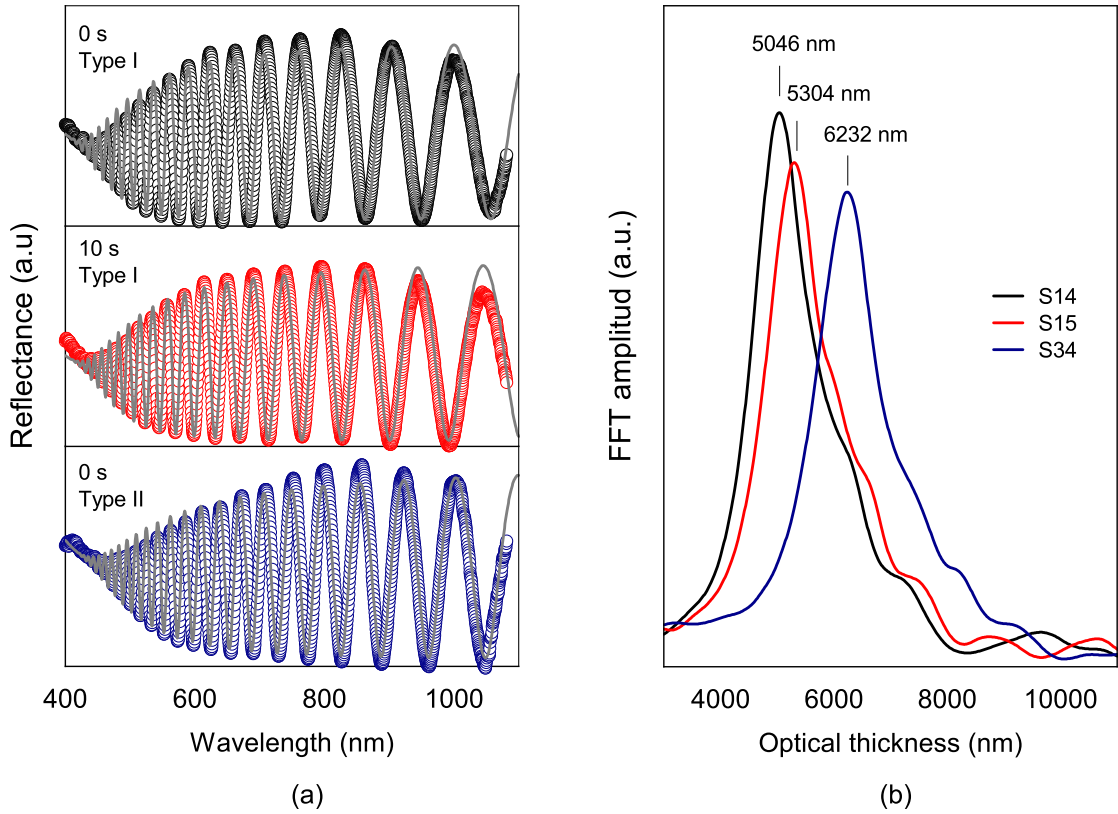


Figure 15 – **(a)** Reflectance spectra of single layer PS with low porosity anodized with electrolyte type I (black), with 10 s of etch-stop time in electrolyte type I (red), and electrolyte type II (blue). A Gray solid line represents the fitting curve of each experimental curve. **(b)** Reflectivity Interferometric Fourier Transform Spectroscopy (RIFTS) of data obtained from reflectance spectra.

porous layer, respectively. According to this figure, a porous structure with OT of 5046 nm is obtained when no etch-stop is applied (S14), but the etch-stop (10 s) inclusion promotes the formation of a porous structure with OT of 5304 nm, while the PS anodized with the electrolyte type II (S34) produces an even larger shift with OT = 6232 nm. Since OT is defined by the product of the physical thickness times the effective refractive index, the reason for this behavior is associated with the variation of both parameters once these they are linked to each other, i.e, changes in thickness unavoidable leads to changes in porosity (effective refractive index).

Aiming to measure both thickness and porosity, the SLIM method was used measuring the optical reflectance of PS in air and liquid with a well-known refractive index. Different liquids were used (ethanol, methanol, toluene, heptane, and isopropyl alcohol). To calculate the porosity and thickness, the nonlinear system of equations given by Equations (4.1) and (4.2) was solved, using the OT of the sample in air and liquid extracted by interference fringes or FFT. The values for porosity and thickness depend on the approach used for the effective medium. For our samples, Bruggeman's model for $L = 1/3$ was used, with the relationship between OT in air and the effective refractive index in

air, $n_{eff} = OT_{air}/d_{PS}$, and between OT in liquid and the corresponding effective refractive index $n_{eff} = OT_{liq}/d_{PS}$ inserted into the equations

$$p \frac{\varepsilon_{air} - \varepsilon_{eff}}{\varepsilon_{air} + 2\varepsilon_{eff}} + (1 - p) \frac{\varepsilon_{Si} - \varepsilon_{eff}}{\varepsilon_{Si} + 2\varepsilon_{eff}} = 0 \quad (4.1)$$

$$p \frac{\varepsilon_{ethanol} - \varepsilon_{eff}}{\varepsilon_{ethanol} + 2\varepsilon_{eff}} + (1 - p) \frac{\varepsilon_{Si} - \varepsilon_{eff}}{\varepsilon_{Si} + 2\varepsilon_{eff}} = 0 \quad (4.2)$$

where p and d_{PS} are the porosity and thickness of PS, and ε_{eff} is the effective dielectric function of the porous matrix ($\varepsilon_{eff} = \sqrt{n_{eff}}$) which is wavelength dependent. Equations (4.1) and (4.2) were solved simultaneously using the Newton-Raphson method for computing p and d_{PS} .

Finally, the third method was to use the relation describing the interaction of light with thin films, expressed by the Fresnel relationship (Equation 2.2). However, since it was derived for non rough thin films with sharp interfaces and homogeneous mass density along the entire surface, the correction for porous structures with rough interfaces was made by taking into account this roughness, σ , using Equation 2.10, whereas $n_{PS} = n_{eff}$ is computed as a function of porosity using the BEMA, assuming the PS film composed of spherical pores ($L=1/3$). The results of these three methods are summarized in Table 4. According to this table, S15 is thicker than S14, while SLIM and the fitting procedure indicate that the thickness of S34 is greater than that of S15. These results are compatible with the thicknesses measured by SEM, as shown in Table 4. Comparing the results of these three methods, the thickness of sample S34 measured by SEM appears thinner. This apparent discrepancy could be explained by the following facts: SEM is a local analysis technique, and also our samples are not completely homogeneous in their thickness, because during pore formation a larger current density is located in the middle region of the sample [51], i.e., the thickness at the lateral Si/PS interface is thinner. On the other side, the formation of thicker layers in aqueous HF solution - here referred to as electrolyte type II- has been reported by several research groups [41][78]. The observations of these groups suggest that the incorporation of H₂O into the solvent increases the SiO₂ growth rate due to the large affinity between Si and oxygen, and therefore Si is more susceptible to be attacked by HF, which increases the silicon etching rate, resulting in thicker porous structures with lower porosity than in solutions without H₂O.

Concerning to the porosity, a small decrease in porosity of about 1.5% is observed when an etching pause is included during the pore formation in electrolyte type I. This slight decrease can be explained by the pause between processes enhancing HF diffusion toward the etch-front, resulting in the formation of pores with slightly different diameters. For a given substrate property, the pore shape and size depend on the HF concentration [53]. In addition, Billat et al [77] indicated that the etch-stop creates a more controllable in-depth porosity gradient that could be treated as a new layer. However, in our case,

since was incorporated just one pause of 10 s in the entire structure, unlike Billat [77], the slight porosity variation could be assumed just as a deviation within experimental error.

4.1.2 High porosity single layers

For the H porosity devices, three single-layer samples were prepared with the same electrochemical parameters: Current density of 50.0 mA/cm^2 and etching time of 300 s. The samples without the etch-stop were designated as S16, immersed in electrolyte type I, and S35, engaged in electrolyte type II. S17, on the other hand, represents the sample prepared with an etch-stop time of 10 s. For the latter sample, the total etching time (300 s) was divided into a first corrosion of 120 s, followed by a pause of 10 s, and then the second corrosion of 180 s.

Figure 16 shows the cross-sectional images SEM of samples S16, S17, and S35, whose physical thickness was measured at 2955 nm, 4470 nm, and 4845 nm, respectively. The thickness was also measured by two other methods, SLIM, and the fitting method, whose reflectance spectra were measured in air and at room temperature, as shown in Figure 17a. In this figure, the etch-stop effect is clearly seen as the reflectance spectrum of S17 (red open circles) appears shifted with respect to that of S16 (black open circles), while the reflectance spectrum also appears shifted upon addition of H_2O to the electrolyte. This fact is better visualized by RIFTS in Figure 17b. From this figure, it can be seen that a porous structure with $\text{OT} = 7186 \text{ nm}$ is formed when no etch-stop is applied (S16), but the inclusion of the etch-stop during anodization changes OT to 7449 nm . Similar behavior is observed when electrolyte type II is used ($\text{OT} = 8459 \text{ nm}$). This shift is more significant than that in low PS, which should translate into a larger change in thickness or porosity. To determine both the thickness and porosity, the SLIM by solving Equation

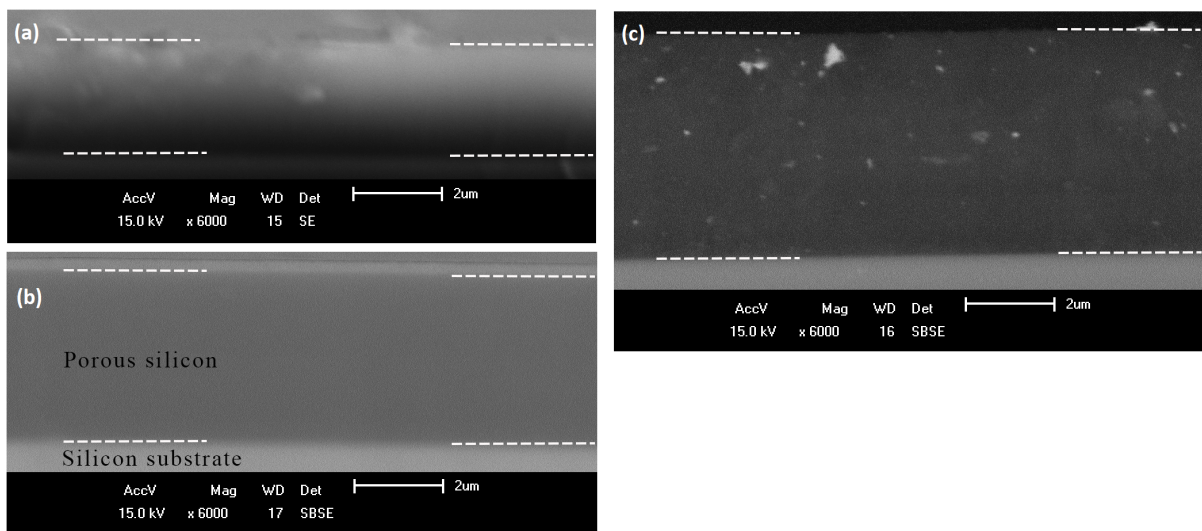


Figure 16 – Scanning electron micrograph of a highly porous single layer from samples (a) S16, (b) S17, prepared by the etch-stop method for 10 s pause, and (c) S35.

Table 5 – Optical parameters of H-single layers. For the SLIM and Fresnel methods, the BEMA spheres were used.

	Etch-stop time (s)	Electrolyte	Thickness (nm)			Porosity (%)		
			SEM	SLIM	Fresnel	SEM	SLIM	Fresnel
S16	0	Type I	2955 ± 86	4620	4500	-	68.3	73
S17	10	Type I	4470 ± 111	5049	4780	90.5	71	74.5
S35	0	Type II	4845 ± 26	5458	5000	-	68	70.5

4.1), and 4.2, as well as by fitting the reflectance data using Equation 2.7 for the case of rough interfaces (Equation 2.10). The results are shown in Table 5. These results show a significant increase in thickness. Again, the structure yielded using electrolyte type II depicts larger OT than the others. According to previous reports [41][78], the addition of H₂O to the HF:ethanol solution could allow homogeneous and high-quality pores, and this fact, combined with the formation of well-defined big pores when high current densities are applied [50], suggest that the incorporation of a pause in the H single layer could promote the formation of more regular distribution of the pores along the whole structure.

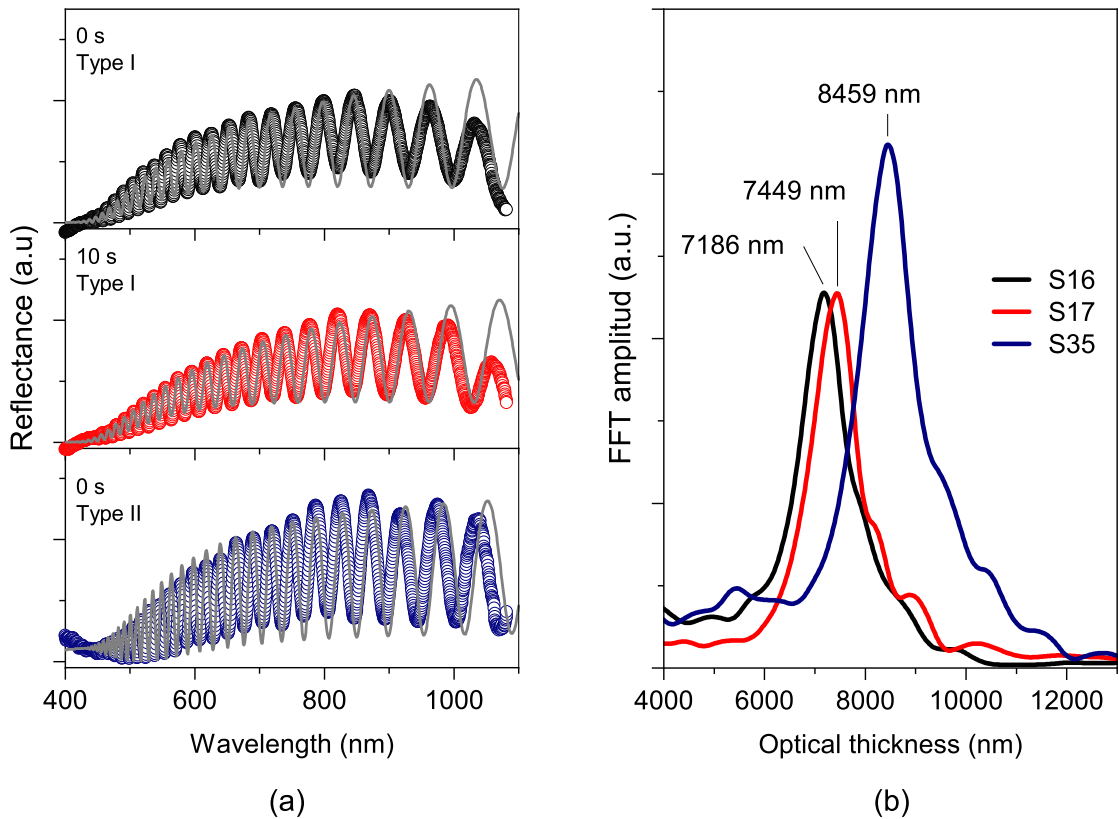


Figure 17 – (a) Reflectance spectra of a highly porous single layer PS, anodized with electrolyte type I (black), with 10 s of etch-stop time in electrolyte type I (red), and electrolyte type II (blue). A gray solid line represents the fitting curve of each experimental curve. (b) Reflectivity Interferometric Fourier transform spectroscopy (RIFTS) of data obtained from reflectance spectra.

4.1.3 FTIR analysis of single layers

According to the literature [58], porous silicon structures exhibit aging problems because their high specific area, about $1000 \text{ m}^2/\text{cm}^3$, reacts with ambient air and consequently their chemical and optical properties change with time due to the formation of native SiO_2 . For example, after drying, oxygen adsorbs to the ambient air, and its presence increases in a non-passivated sample. The presence of this compound leads unavoidably to in time changes of the effective refractive index of the porous structure, at least that silicon oxide is grown purposely. To confirm this trend in our samples, they were analyzed by FTIR after 13 days of formation. Figure 18 shows the presence of the main vibrational modes of the Si-O-Si groups at 804 and 1054 cm^{-1} . According to the literature [58], the absence of functional groups $\text{O}_x\text{-Si-H}$ from 2200 to 2500 cm^{-1} indicates that the PS single layers are not fully oxidized. The presence of CH_x bonds as well as C=O and Si-O bonds also indicates such confirmation, which is found in all samples. However, the peaks at 1209 and 1740 cm^{-1} are marked in sample S17 and belong to the asymmetric and symmetric stretching vibrations [79] of the carbonyl group O-C=O . The peak at 874 cm^{-1} corresponds to the stretching vibration of the C=O bonds. Regarding the peaks at 2926 and 1368 cm^{-1} corresponding to the CH_x groups, it is important to highlight that their source seems to be associated with the remaining solvent inside after the SLIM analysis. The hydrocarbons that predominate in the sample with the etch-stop time suggest that they adhere to the pore wall because the pore diameter decreases, making it difficult for the molecules to diffuse through the pores. The FTIR analysis confirms the aging effect of

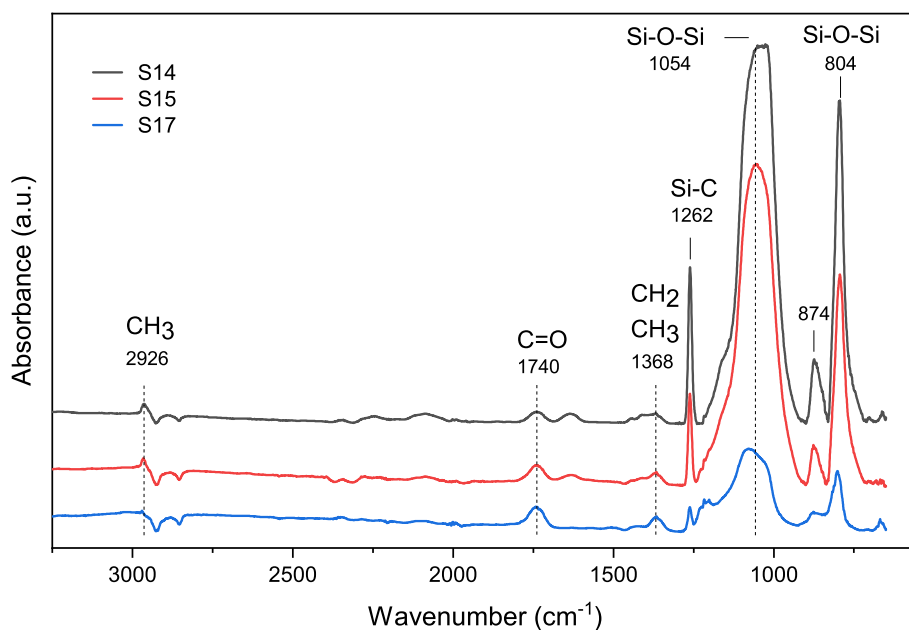


Figure 18 – Optical absorbance of porous single layers anodized in electrolyte type I and time I for low porosity: S14 (0 s) and S15 (10 s), and high porosity: S17 (10 s).

PS. The use of as-etched devices is not suitable for sensing purposes because its natural aging trend. For this application, the porous structure must be passivated.

4.2 Structural and morphological characterization of one-dimensional porous silicon photonic crystal

In the previous section, the effect of the etch-stop time on the single layers L and H was studied, which promoted the increase of the thickness and of the effective refractive index, the latter being measured by the dependence on porosity. In the following, the effect of the number of layers with the etch-stop method, the influence of the upper layer, and the type of electrolyte are studied.

4.2.1 One-dimensional porous silicon photonic crystal using type I and time I

For this purpose, two sets of multilayer structures defined as 1D-PSPC were prepared by periodically forming layers with L and H porosity according to the $(LH)^N$ and $(HL)^N$ sequence, where $N=15$ denotes the number of periods. Both sets of devices were prepared with the same electrochemical parameters: Current density of $j_L = 5 \text{ mA/cm}^2$ and $j_H = 50 \text{ mA/cm}^2$ during times $t_L = 11.2 \text{ s}$ and $t_H = 7.1 \text{ s}$ (called Time I) and immersed in electrolyte Type I.

Following the $(LH)^{15}$ structure, four samples were prepared. The one without etch-stop was named S6, and the other three were prepared with the following etch-stop times of 5, 8, and 10 s and named as S12, S22, and S5, respectively. In the second group, prepared with $(HL)^{15}$, the sample without etch-stop was designated as S7, while S8 represents the sample prepared with a 10 s of pause.

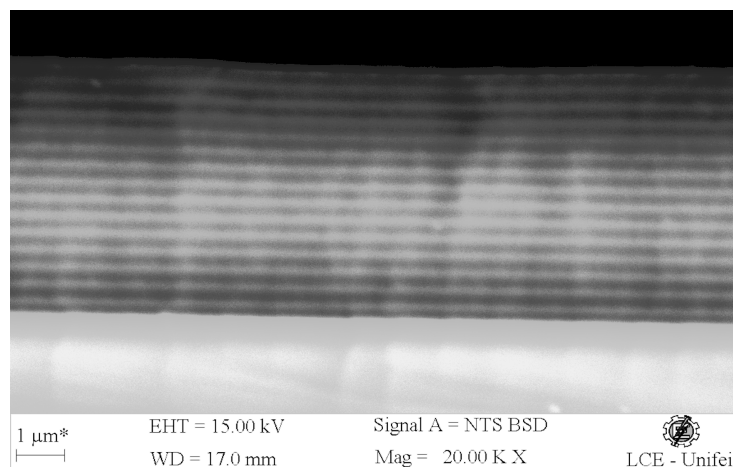


Figure 19 – Scanning electron microscope image of a one-dimensional photonic crystal. The light gray layer corresponds to low porosity (L) and the dark gray to high porosity layer (H).

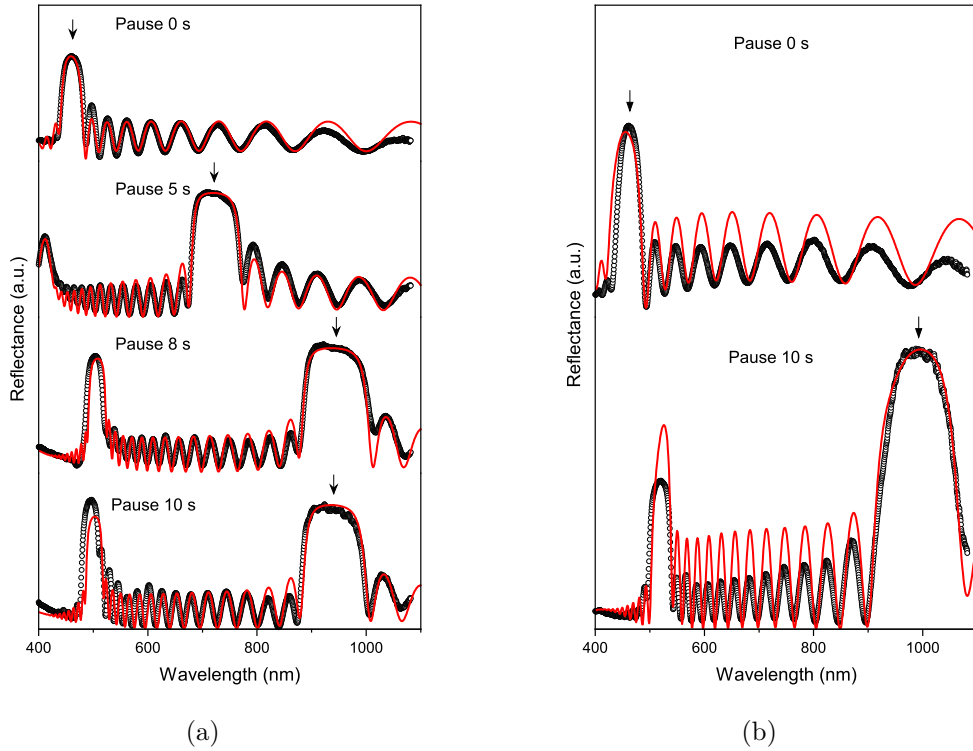


Figure 20 – Comparison of the reflectance spectra of multilayer structures for the (a) $(LH)^{15}$ and (b) $(HL)^{15}$ structure types for different etch-stop times. See the distortion of the lateral edges of the PBG of $(HL)^{15}$ sample with 10 s of pause. The red curve represents the fitting curve, where the input parameters are summarized in Table 6.

Figure 19 shows a representative cross-sectional image SEM of a 1D-PSPC with the etch-stop time (S22). The layers are well-defined and two types of layers can be distinguished. The parallel light gray lines correspond to the layers with low porosity (high refractive index), while the dark gray lines represent the layers with high porosity (low refractive index).

The optical reflectance of these structures taken in air environment at room temperature is shown in Figure 20. In this figure, the etch-stop effect is indicated by the black arrow in the photonic band gap (PBG), and a red shift of the PBG along the pause increments can be observed. In Figure 20a, for the 1D-PSPC having $(LH)^{15}$ yielded without pause, the photonic band appears at 461 nm, and is redshifted in about 263 nm in the sample yielded using 5 s of etch-stop time so that the main PBG is located at 724 nm and its secondary one appears 411.5 nm. When 8 s of etch-stop time is applied, the main PBG is shifted to 947 nm and a secondary photonic band appears at 496.5 nm. Similar behavior was observed in the sample anodized including 10 s of etch-stop.

In the case of the structure $(HL)^{15}$, the reflectance spectrum shows a photonic band at 463 nm and at 10 s of etch-stop time it is shifted 530 nm to the right and a secondary photonic band appears at 520 nm. These bands are visible in a portion of the

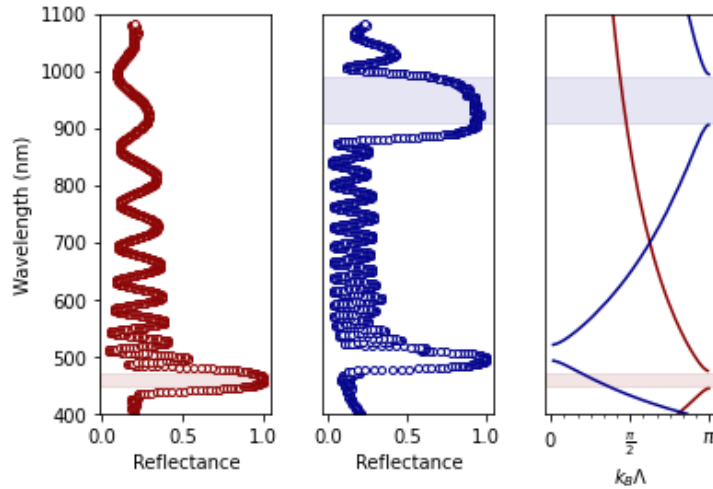


Figure 21 – *Experimental results of the relation dispersion for 1D-PSPC, S6 (red) and S5 (blue) using real and wavelength dependence effective refractive index. The shadow signs the position of the principal forbidden bands.*

near-infrared (NIR) region due to instrument limitations. The main PBG at a pause of 10 s has different features in the two structures. The lateral bands of (HL)¹⁵ are clearly lopsided. This is an effect of roughness at the interface due to the loss of refractive index contrast, which creates tiny gradients in the H-L adjunct. This roughness also results in more light scattering, making the optical response of the secondary band only half as intense as that of the main PBG. While the (LH)¹⁵ structure performs better at the higher etch-stop time, this is observed at the main PBG edges and the intensity of the secondary PBG, which is similar to an ideal 1D-PSPC. In an ideal 1D-PC, the PBG edges appear completely vertical.

The analysis of the optical behavior with respect to the dispersion properties of these samples can be seen in Figure 21. This dispersion diagram was constructed considering the wavelength dependence of the effective refractive index of the H and L layers conforming to the 1D-PSPC. The red line corresponds to the dispersion diagram for the device fabricated without a pause, while the blue solid line is for the device fabricated with a 10 s of etch-stop time. As for the PBG position and width, the etch-stop results not only in a change of the PBG position but also in an increase of the width. The forbidden modes correspond to the photonic band gap of the reflectance spectra shown on the left and in the center of the figure.

The main feature of a 1D-PSPC is its PBG, where the center of the PBG, λ , relates to the OT of the structure. From Figure 20, it can be seen that the fabrication of 1D-PSPC with different etch-stop times produces structures with different OT, i.e., unit cells with different characteristics in terms of thickness and porosity, as in the case of the single layer produced by a pause during pore formation. To investigate the effect of the pause on the thickness and porosity of multilayer structures with 15 unit cells, the

experimental reflectance data were fitted using TMM and BEMA ($L= 1/3$) to calculate the effective refractive index of each H and L layer as a function of porosity. The results are summarized in Table 6. According to this table, the etch-stop increases the etching rate of silicon, which is the reason why the thickness of H and L layers becomes thicker, and also increases the values of n_H and n_L associated with the decrease of porosity p_H and p_L , respectively. According to Figure 22 and Figure 23, this behavior does not depend on the multilayer stacking order, i.e., the same results are observed for 1D-PSPCs formed following the HLHL... HL or LHLH... LH sequence, as can be seen in Figure 22a. This increase in thickness and in n_{eff} explains why the redshift of λ follows an almost linear dependence with the etch-stop time. A similar trend is observed for the FWHM of the PBG width, $\Delta\lambda$. According to the results in Table 6 and Figure 23, the values of d_H , and d_L as well as of p_H , and p_L are larger, although the devices with the sequence (HL)¹⁵ were fabricated with the same electrochemical parameters as the (LH)¹⁵. These results suggest that the porosity of the upper layer is important for the etching rate and the formation of the pore size. This could be related to the larger pore size embedded in the first upper layer with high porosity when compared to the L-layers. This allows for better HF diffusion toward the etch-front, leading to faster silicon etching during the formation of PS.

Billat et al. [77] have shown, with reference to Figure 22 and Figure 23, that the incorporation of pauses during PS formation leads to an increase in thickness and a decrease in porosity because the etch-stop allows better diffusion of HF into the electrolyte, i.e., during the pause, the consumed HF is restored at the etch-front so that the etching rate of the silicon returns to its original performance, which promotes the formation of thick layers with the better mechanical stability of the layers at depth. In summary, diminution of thickness in-depth is an expected fact that is restored by the inclusion of etch-stop, although the apparent increase in thickness to the naked eye. This apparent increment insofar the etch-stop time increment is verified by comparing the structural features of both sets of devices.

Table 6 – *Optical parameters of 1D-PSPC anodized with electrolyte type I and etching time I at different etch-stop times. Thickness and porosity values were fitted by TMM method using BEMA sphere model.*

Samples ID	Break (s)	d_L (nm)	d_H (nm)	p_L (%)	p_H (%)	λ (nm)
S6	0	35	118	70.5	78.5	461.4
S12	5	62	175	65	75.8	725.2
S22	8	70	210	58	69.7	935.9
S5	10	75	220	61	72	938.5
S7	0	36.3	121	71	81	463.7
S8	10	92.5	230	65	75	993.4

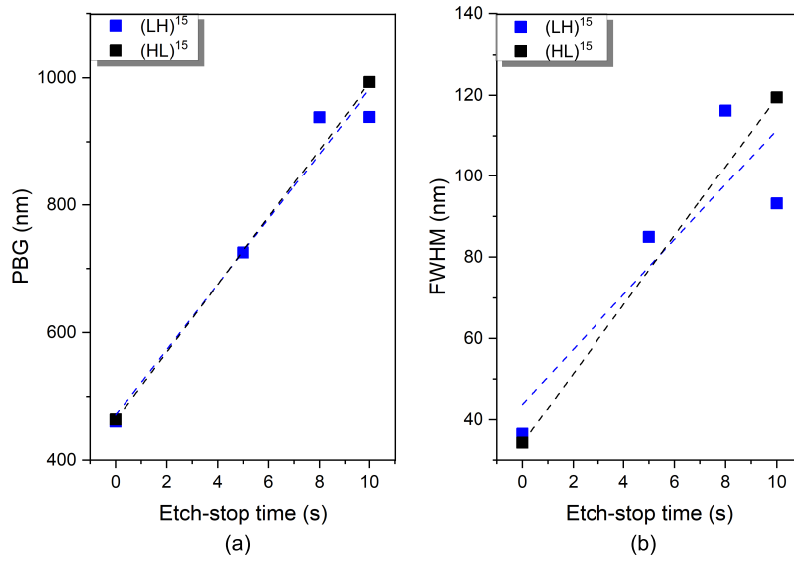


Figure 22 – Optical parameters of (a) photonic band gap and (b) full width at half maximum of the PBG from Table 6 for samples anodized with electrolyte type I and etching time I.

The physical thicknesses of the 1D-PSPC, shown in Figure 23, follow a linear relationship and the fitting parameters of that trend are summarized in Table 7. These results show that the slope of the d_L curve is higher in the (HL)¹⁵ structure and is associated with a higher etching rate than in (LH)¹⁵ structure, although the same electrochemical parameters were used in both cases. No significant change is observed in the d_H profile. As mentioned before, this change in the etching rate is related to the enhancement of HF diffusion due to the pause. This fact is particularly pronounced when the first upper layer consists of large pores and has high porosity, as in the (HL)¹⁵ structure. This fact, together with the longer etch-stop time could allow faster restitution of the consumed HF at the etch front during pore formation. Thus, the HF diffusion, and the structure type play the uttermost role in the etching rate, thickness, and porosity of the porous structure.

Table 7 – Displacement of the physical thickness as a function of the etch-stop time, obtained from the BEMA ($L = 1/3$) fitted from Figure 23, was used a linear function, $y = a + b\tau$.

1D-PSPC		a	b	Adj-R ²
		(nm)	(nm/s)	
(LH) ¹⁵	d_L	41.5 ± 2.4	3.5 ± 0.3	0.97
	d_H	121.9 ± 5.1	10.3 ± 0.7	0.98
(HL) ¹⁵	d_L	39	5.35	-
	d_H	112	11.8	-

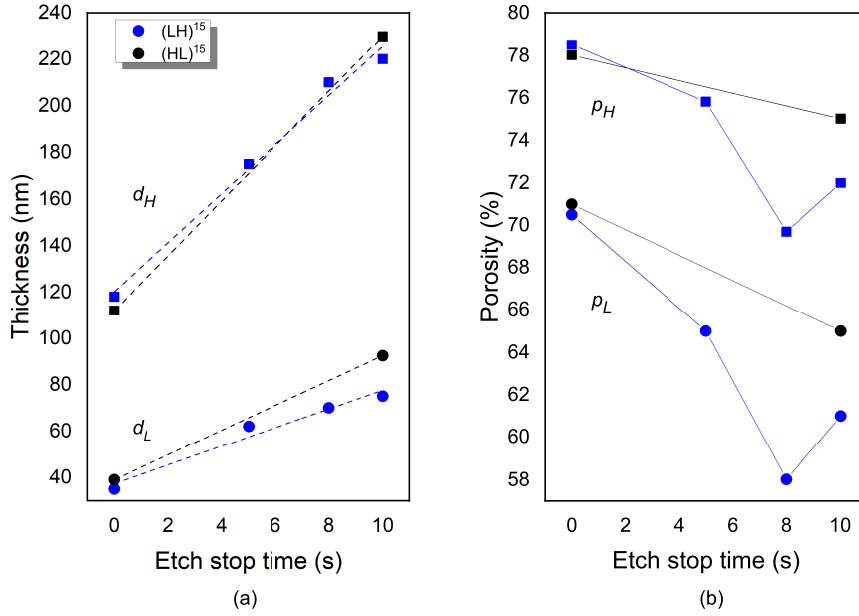


Figure 23 – Input parameters of (a) thickness and (b) porosity using Bruggeman's model for spheres in TMM for 1D-PSPC of (LH)¹⁵ (at blue) and (HL)¹⁵ (at black) devices anodized with electrolyte type I and etching time I.

Table 8 – Optical parameters of porosity, thickness, and center of the PBG of 1D-PSPC anodized with time I at different etch stop time.

Samples ID	Pause (s)	Electrolyte	d_L (nm)	d_H (nm)	p_L (%)	p_H (%)	λ (nm)
S27	5	Type I	75	182	59.7	70.5	857.1
S36	5	Type II	80	191	58.7	71.4	895.8

4.2.2 Devices yielded using solution II and set time I

Two 1D-PSPC were fabricated using the (LH)¹⁵ sequence with the same electrochemical parameters: Current density of $j_L = 5 \text{ mA/cm}^2$ and $j_H = 50 \text{ mA/cm}^2$ during times $t_L = 11.2 \text{ s}$ and $t_H = 7.1 \text{ s}$ (denoted as Time I) and etch-stop time of 5 s in different electrolytes. The sample anodized in electrolyte Type I was designated as S27, and the sample immersed in electrolyte Type II was set as S36.

The optical response of these devices is shown in Figure 24. Although both devices were prepared with the same electrochemical parameters, the reflectance spectrum of the principal PBG anodized with type II is red-shifted by 38.7 nm compared to the PBG anodized with electrolyte type I, whose PBG is at 857 nm. This fact could be explained by the additional oxidizing effect of H₂O, which promotes the formation of silicon oxide prior to pore formation. Since the pores are formed by the divalent consumption of silicon by SiO₂, the presence of H₂O increases SiO₂ formation and thus the silicon etching rate during anodization [9] [31] [56].

The inclusion of a pause in the anodization method and of H₂O in the electrolyte

solution caused a higher shift of the PBG and the increase of the $\Delta\lambda$, the latter indicating a more differentiated contrast between H and L layers (Eq. 2.28), whose optical parameter can be observed via porosity, summarized in Table 8.

4.3 Structural and morphological characterization of one-dimensional porous silicon photonic crystal with resonant microcavity

In the previous section, it was shown the importance of the first upper layer of the multilayer stack for the optical response of the 1D-PSPC, which was fabricated by the etch-stop method and showed better performance than the $(LH)^{15}$ device. Considering this fact, the 1D-PSPC with resonant microcavity (called 1D-PSPC-Mc) was fabricated by using the L-layer as the first upper layer, i.e. the 1D-PSPC-Mc was fabricated according to the LHLH...LHHL...HLHL sequence consisting of a structure type $(LH)^7$ followed by a second structure $(HL)^8$ abbreviated as $(LH)^7(HL)^8$.

4.3.1 Photonic crystals yielded in HF:ethanol (3:7) and set Time I.

The 1D-PSPC-Mc was used to systematically investigate the influence of electrolyte and anodization time on the dependence of microcavity position and thickness on the etch-stop time. For this purpose, four samples were prepared with the same electrochemical parameters: Current density of $j_L = 5 \text{ mA/cm}^2$ and $j_H = 50 \text{ mA/cm}^2$ during times of $t_L = 11.2 \text{ s}$ and $t_H = 7.1 \text{ s}$ and immersed in electrolyte Type I. In the previous

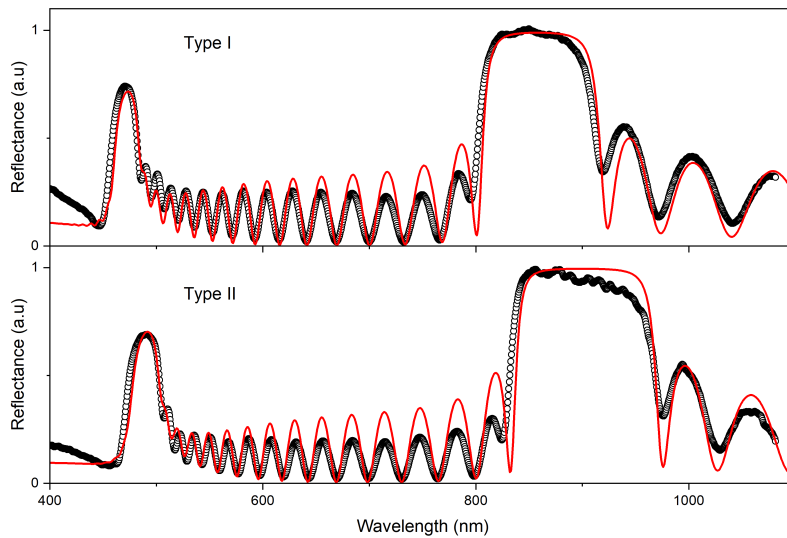


Figure 24 – Comparison of the reflectance spectra of $(LH)^{15}$, with density current of $j_L = 5 \text{ mA/cm}^2$ and $j_H = 50 \text{ mA/cm}^2$ with 5 s of etch-stop time in electrolyte type I (above) and type II (below). Showing a displacement of the PBG due to a change in the electrochemical analyte. Black circles are the experimental data of samples S27 and S36, red solid line is the fitting curve (BEMA).

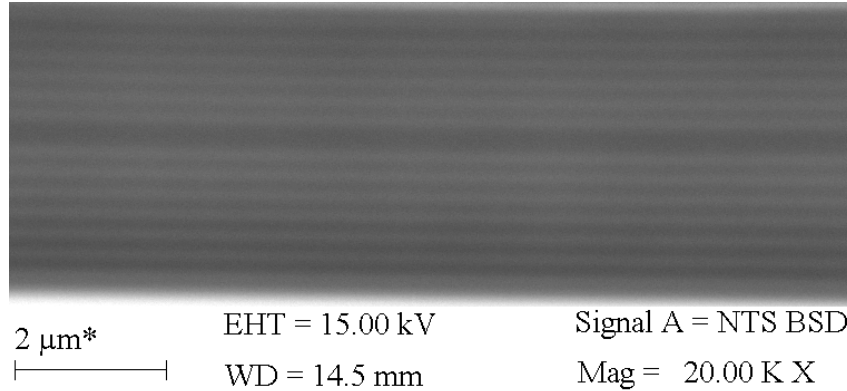


Figure 25 – Representative SEM image of a one-dimensional porous silicon photonic crystal with microcavity (1D-PSPC-Mc).

section, a better performance of the (LH)¹⁵ than the (HL)¹⁵ structure was observed, therefore the 1D- PSPC-Mc structures were initialized with L-layer and fabricated with the following structure (LH)⁷(HL)⁸. Again, the etch-stop time was introduced between two adjacent L and H layers, and a pause was incorporated inside the microcavity after a time of t_H to evaluate the optical response of the resonant microcavity. The sample without etch-stop was designated as S33, while S32, S31, and S24 represent the sample with 3, 5 and 8 s etch-stop time, respectively. Figure 25 shows a representative SEM image of the 1D-PSPC-Mc with an etching time of 5 s. It shows a periodic structure composed of an L and H layer (gray and black color, respectively), and the microcavity in the center of the SEM image is very clear.

The reflectance spectra of the devices (Figure 26a) show the expected redshift behavior of the PBG (Figure 26b), insofar the etch-stop time increases. Similar behavior was observed for the width of the PBG (or FWHM) (Figure 26c), except for the device obtained with an etch-stop time of 3 s. This increase in FWHM can be explained by the fact that in a 1D-PSPC with a microcavity with sharp and smooth interfaces, the resonance peak appears deep and with narrow FWHM. A strong asymmetry of λ_c in the PBG is also observed. However, this dislocation is not related to the corrosion properties or the parameters included in the analysis. Instead, this behavior is attributed to a violation of Bragg's law (Equation 2.30) of the microcavity caused by the incorporated pause in the microcavity. Nevertheless, the 8 s of etch-stop time cause a correction of the OT of the resonant microcavity and leads to a blue shift of the λ_c to its correct position.

Table 9 summarizes the quantification of thicknesses d_H , d_L and d_c , and porosities p_H , p_L and p_c by the fitting procedure of the reflectance spectra of Figure 26a using the TMM and BEMA for the sphere model. These results show the same characteristics as those of the 1D-PSPC: increase in thickness and n_{eff} with etch-stop time. However, the deviation from this behavior observed for the sample fabricated with 3 s of pause could be due to experimental errors during anodization. Nevertheless, the dependence of the

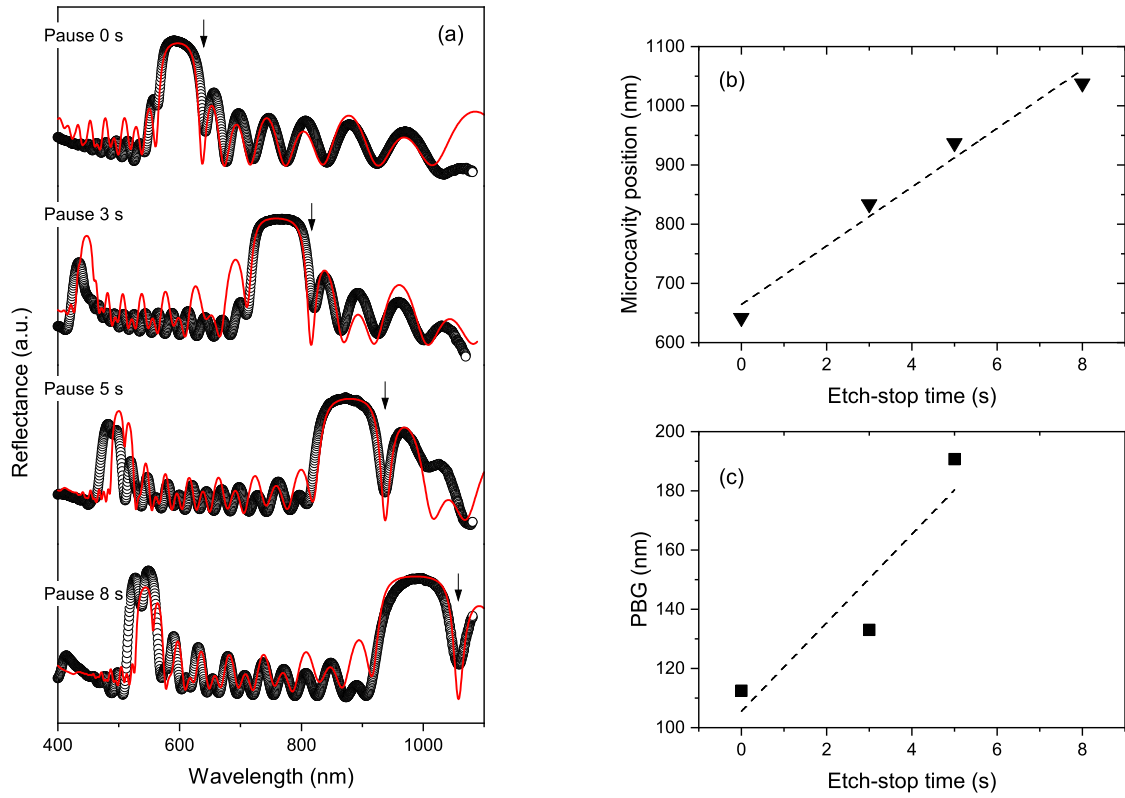


Figure 26 – (a) Optical response of as etched 1D-PSPC-Mc of samples S31-S33, showing the (b) resonance peak position microcavity redshifted, as well as (c) the PBG width for the different etch-stop times. These devices were fabricated using electrolyte type I and etching time I.

thickness and porosity on the etch-stop can be fitted by an exponential curve, $d = a + be^{ct}$ (Figure 27), where the coefficients b and c refer to the etching rate.

4.3.2 Photonic crystals yielded in HF:ethanol:H₂O (3:4:3) and set Time I.

Three 1D-PSPC-Mc were prepared in the following order (LH)⁷(HL)⁸. They were fabricated with the same current density corrosion parameters described in Chapter 3 using etching time I and electrolyte type II. The devices were fabricated using the etch-

Table 9 – Variation of thickness and porosity with respect to etch-stop time determined from optical response of devices prepared with electrolyte type I and time I.

Samples ID	Pause (s)	d_L (nm)	d_H (nm)	d_c (nm)	p_L (%)	p_H (%)	p_c (%)
33	0	50.5	89	263	48.8	58.9	65
32	3	45	140	320	43	58.6	54
31	5	55	155	327	42	56.3	50
24	8	62.5	171	330	40	56	50

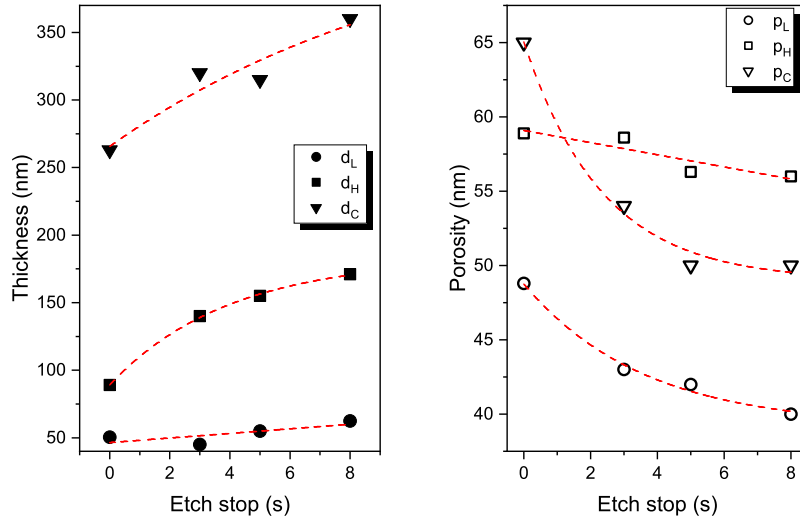


Figure 27 – Input parameters of (a) thickness and (b) porosity using Bruggeman's model for spheres in TMM for 1D-PSPC-Mc of samples S31-S33, anodized with electrolyte type I and etching time I.

stop method with pauses of 0, 3, and 5 s and designated as S39, S37, and S38, respectively. The reflectance spectra of these devices are shown in Figure 28a. It can be observed that the position of λ_c , marked by the black arrow, is located near the middle of the PBG for the three cases and shows the expected redshift and linear trend with pauses (Figure 28b). However, the inclusion of the etch-stop time leads to a decrease in the quality of the transmission band, as evidenced by the decrease in intensity at the depth of λ_c and the increase in $\Delta\lambda_c$ (Figure 28c).

The addition of H_2O to the electrolyte leads to an increase in the silicon etching rate so that the physical thicknesses d_L , d_H , and d_C are higher than for devices prepared by anodization in electrolyte type I (see Table 9 and Table 10 for comparison). These results evidence that the relationship between the thickness of the microcavity and the H layer ($d_C = 2d_H$) is achieved only for devices fabricated with setting time I and electrolyte type II. As for the porosity, it becomes larger in the structure prepared with the electrolyte type II. This increase was attributed to the additional oxidation due to the presence of H_2O . The change in the etching rate should lead to an increase in porosity and a decrease in pore diameter compared to the previous case.

The thicknesses obtained from the fitting procedure can be fitted with a linear or exponential fit. Since the exponential function is more general so that it can be expressed in a polynomial trend and truncated to the linear function, the thickness values from Figure 29 were fitted with the exponential function since it has a high certainty value.

Table 10 – Optical parameters for porous silicon structures with a microcavity, fabricated with electrolyte type II (HF:H₂O:Ethanol) and time I.

Sample ID	Electrolyte	Etch stop (s)	d_L (nm)	d_H (nm)	d_c (nm)	p_L (%)	p_H (%)	p_c (%)
S39	Type II	0	63	143	306	63.8	74.8	70
S37	Type II	3	67	187	374	60.8	72.7	68
S38	Type II	5	80	200	400	59.8	71.6	67.7

4.3.3 Photonic crystals yielded in HF:ethanol:H₂O (3:4:3) and set Time II.

The influence of the incorporation of H₂O to the solvent was studied in the previous section and it was demonstrated that the electrolyte type II improves some optical parameters of the reflectance spectra such as the PBG and the λ_c . In this section, the effect of etching time using electrolyte type II and time II is investigated. For this purpose, five 1D-PSPC-Mc devices were fabricated with an etch-stop time of 0, 2, 4, 6, and 8 s with the same current density as described in Chapter 3. These samples were designated as S40, S45, S42, S43, and S44, respectively.

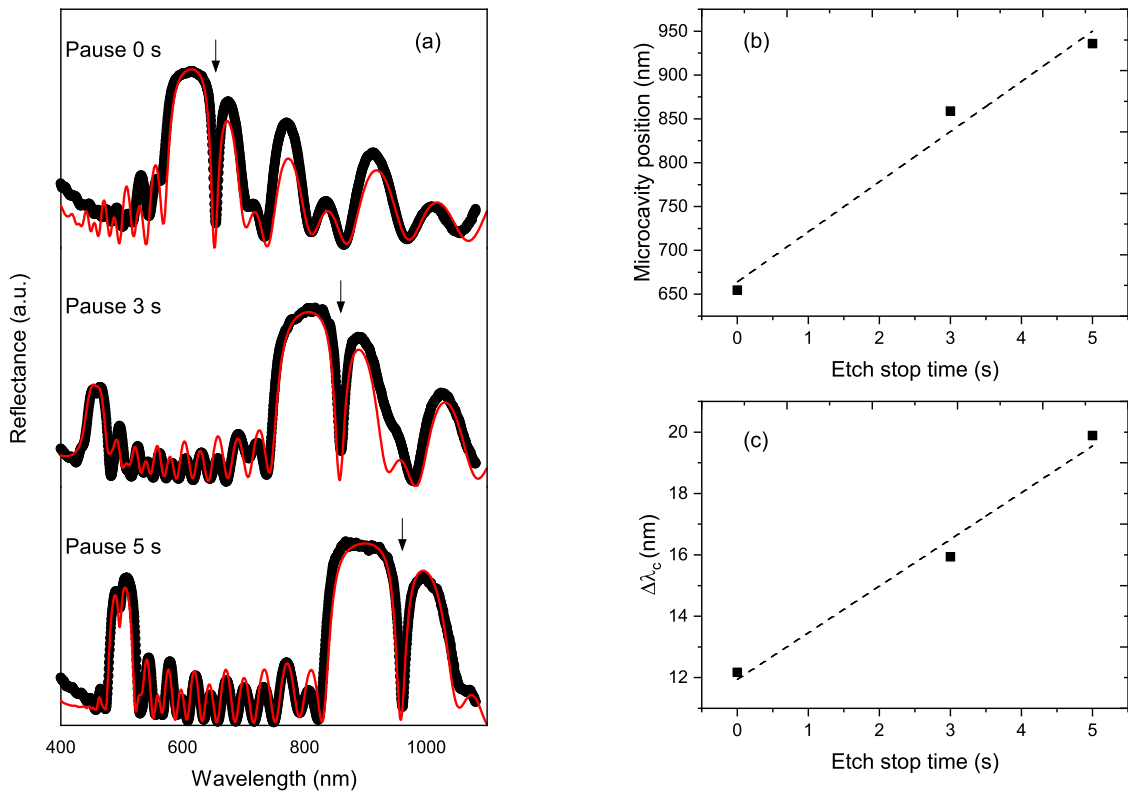


Figure 28 – As etched 1D-PSPC-Mc for sample S37-S39 anodized with electrolyte type II and etching time I. (a) Displacement of the resonant microcavity, marked by the arrow, for different etch-stop time. (b) Evolution of the microcavity position with a pause. (c) Evolution of the transmission band width with the pause.

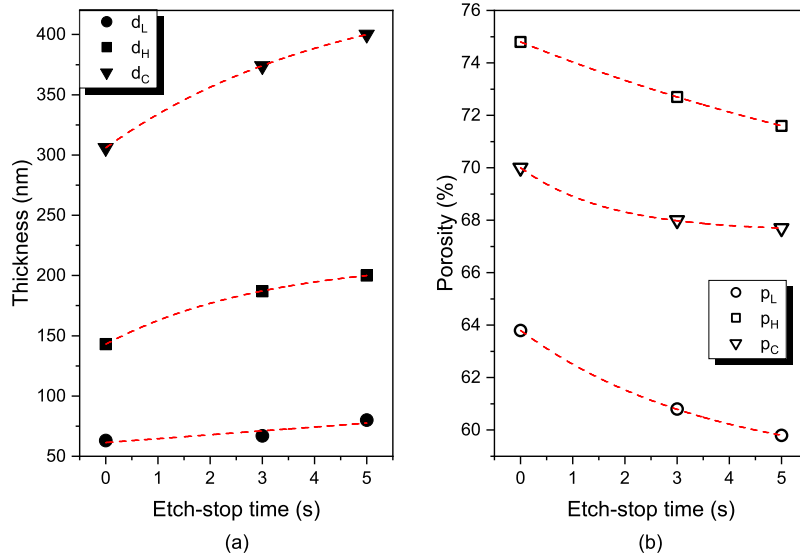


Figure 29 – Input parameters of (a) thickness and (b) porosity using Bruggeman's model for spheres in TMM for 1D-PSPC-Mc of samples S37-S39, anodized with electrolyte type II and etching time I.

Table 11 – Dependence of thickness and porosity at different etch-stop times in 1D-PSPC-Mc for electrolyte type II and etching time II, using BEMA ($L=1/3$) for the fitting procedure.

Samples ID	Etch-stop time (s)	d_L (nm)	d_H (nm)	d_c (nm)	p_L (%)	p_H (%)	p_c (%)
S40	0	56.5	80	160	65	72	70
S45	2	84.5	130	266	61.5	71.5	69.5
S42	4	80.5	160	280	60	71	70
S43	6	100	174	343	60	70	70
S44	8	-	-	-	-	-	-

The reflectance spectrum for the as-etched devices shown in Figure 30a shows the redshift of the transmission band where λ_c appears at 487 nm for 0 s of pause and is located at 955 nm for 6 s pause. The position of λ_c , marked by the arrow, is well centered in the PBG for all reflectance spectra fabricated with the etch-stop method, electrolyte type II, and etching time II, which improved the quality of the resonance microcavity, as shown by the intensity and position of the transmission band. Table 11 summarizes the thickness and porosity values resulting from the fitting procedure of the reflectance spectra using the TMM and BEMA ($L=1/3$) model. These values show an exponential best fit of the thickness, $d = a + be^{c\tau}$ (Figure 31).

To quantify the etch-stop time contribution to the etching rate of silicon for the given electrolyte solutions, the nonlinear thickness profile was fitted with a linear trend, where the slope of the linear curve represents the contribution of etch-stop time to the etching rate. These values were given in Table 12. Devices where etching time I was set in electrolyte type I (S31-S33) and electrolyte Type II (S37-S39) developed thicker H layers.

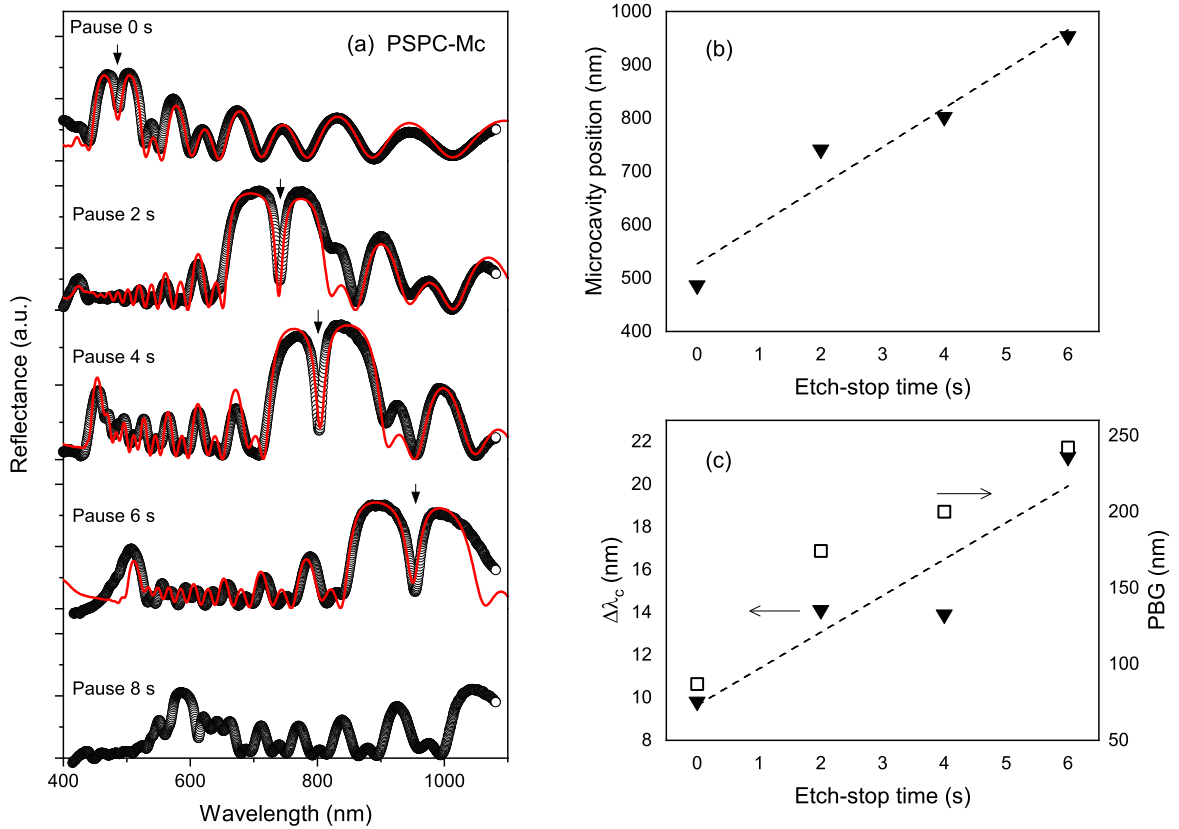


Figure 30 – As-etched 1D-PSPC-Mc of sample S40-S45, anodized with electrolyte type II and etching time II, showing their (a) reflectance spectra. Dependence of the (b) resonant microcavity, and (c) PBG and FWHM of the transmission band ($\Delta\lambda_c$) with the etch-stop time.

However, the incorporation of H_2O increases the etching rate, resulting in a significant increase of 15% for H and 69% for the microcavity. Considering that d_c was obtained at a setting of $t_c = 2t_H$, a similar etching rate is expected. This result is observed only for devices S31 to S33. In contrast, for the devices prepared in aqueous solution (S37-S39), the silicon etching is almost twice as high due to the etch-stop, confirming the importance of both the etch-stop and H_2O in increasing the silicon etching rate. This is the reason why the devices fabricated with the electrolyte type II consist of thicker d_H , d_L , and d_c . The significant difference in thickness between these two groups of 1D-PSPC-Mc devices is mainly related to the etching time since devices S37 to S39 were fabricated with time I, while time II was used for samples S40-S45. This time difference leads to an increase in silicon etching rate of about 92.3, 33.9, and 47.4% for the L, H, and cavity layers, respectively. This comparison highlights the role of the etch-stop time, as this is the reason why devices S40 to S45 have thicker layers, even though they were fabricated with a lower etching time than devices S37 to S39.

Table 12 – Fitted values of the thickness curve obtained from the TMM using BEMA ($L=1/3$) model for 1D-PSPC-Mc from Figure 27 to Figure 31, using the linear function $d = a + b\tau$.

Samples ID	Electrolyte	Etching time (s)	Thickness fitted		Adj-R ²	
			a (nm)	b (nm/s)		
S31-S33	Type I	Time I	d_L	46.4 ± 0.4	1.70 ± 0.98	0.40
			d_H	98.4 ± 10.7	10.1 ± 2.20	0.87
			d_c	269.4 ± 12.6	11.3 ± 2.53	0.86
S37-S39	Type II	Time I	d_L	61.4 ± 4.75	3.23 ± 1.41	0.68
			d_H	145.67 ± 7.5	11.65 ± 2.23	0.93
			d_c	309.05 ± 8.89	19.1 ± 2.64	0.96
S40-S45	Type II	Time II	d_L	61.4 ± 7.76	6.3 ± 2.07	0.73
			d_H	89.2 ± 10.66	15.6 ± 2.85	0.91
			d_c	177.8 ± 22.57	28.15 ± 6.0	0.87

4.4 Passivation of the porous silicon structures

As before mentioned, the porous structure of PS is subject to natural oxidation due to the high reactivity of the surface by the formation of SiO₂ in the ambient air. This fact leads to the degradation of optical properties over time. Such drawbacks prevent the commercial application of PS-based devices. To avoid this degradation, different passivation strategies have been proposed using different materials to cover the surface in a post-treatment. This process aims to avoid the chemical and electrical interaction of

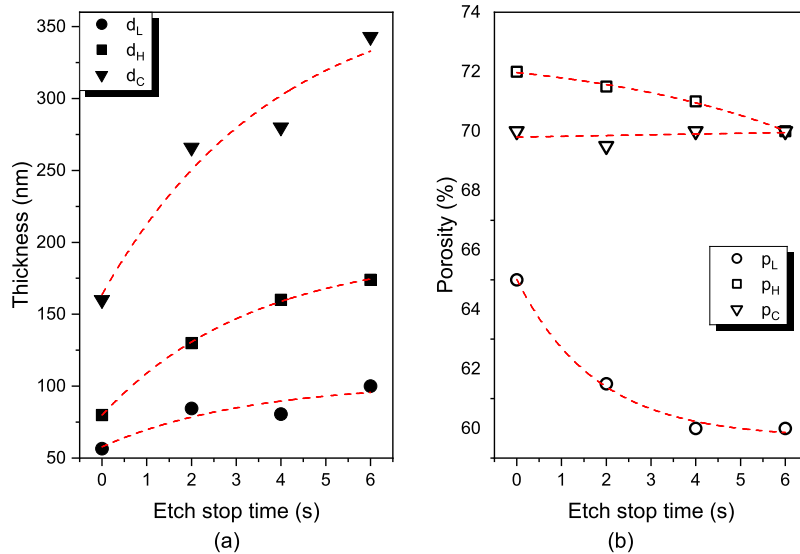


Figure 31 – Input parameters of (a) thickness and (b) porosity using BEMA ($L=1/3$) in TMM for 1D-PSPC-Mc of samples S40-S45, anodized with electrolyte type II and etching time II. The thickness values of all samples show a well exponential fitting.

the porous matrix with the environment. Among the numerous compounds used for this purpose, the thermal and chemical oxidation of silicon is the most common due to its simplicity and ease of use, but the use of polymers, metals and even insulating material must also be considered as alternatives.

The single and multilayers studied here were passivated by thermal oxidation, deposition of TiO_2 by the sol-gel method, and deposition of a thin gold layer. These materials were selected based on some unique properties. In the case of SiO_2 , the main advantage is its high electrical insulating ability, which ensures no charge transfer between the porous matrix and the surrounding environment, and its ease of processing in a conventional oven [72][80].

As for TiO_2 , it was chosen because of its wide use in sensor devices and solar cells [81]. In the case of gold, the use of this element in various optical and electrical gas and liquid sensors has been recently reported due to its catalytic property [82][83]. The passivating properties were investigated optically, as 1D-PSPC and microcavities have the potential to be used as optical gas and liquid sensors, as reported in previous work [35], [68].

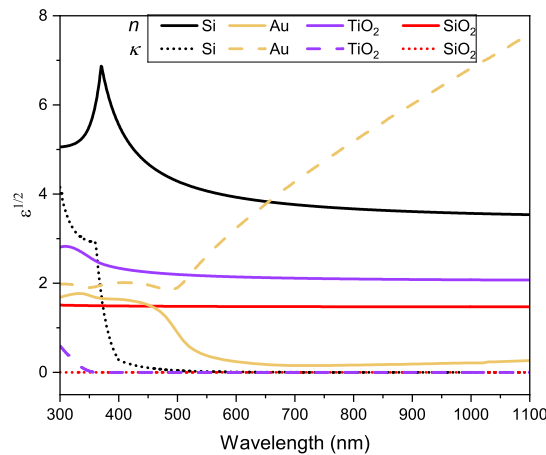


Figure 32 – Comparison between the complex refractive index (\hat{n}) for bulk silicon (black), 53 nm thin film of gold (yellow) [84], titanium dioxide (purple) [85] and silicon dioxide. The solid lines represent the $\text{Re}(\hat{n})$ and the dashed and dotted lines represent the $\text{Im}(\hat{n})$.

4.4.1 Passivation by thermal oxidation

Samples S5, S6, and S8, presented in subsection 4.2.1, were subjected to systematic thermal oxidation in air at 400°C, 600°C, 800°C, and 1000°C during 10 minutes for each step. In the case of the sample yielded without etch-stop (S6), the reflectance spectra (Figure 33) show a PBG at 460.6 nm, which is blueshifted to 440 nm after oxidation at

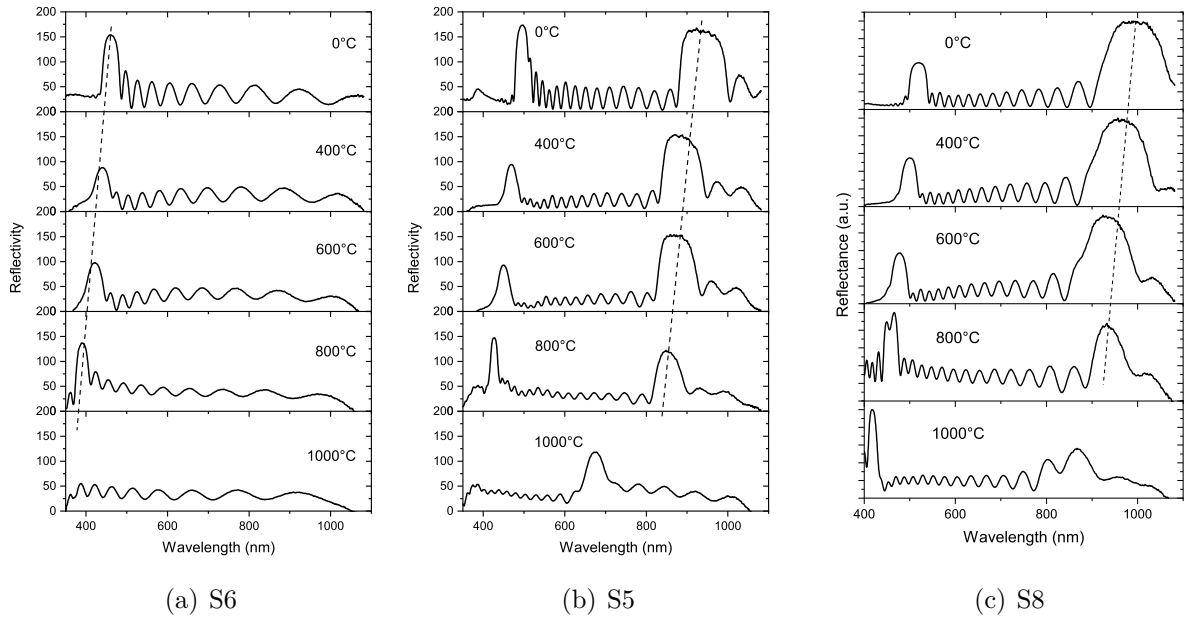


Figure 33 – Reflectivity spectra of as-prepared (top) and those oxidized in air at 400°C , 600°C , 800°C and 1000°C for 10 minutes, for 1D-PSPC fabricated with (LH)¹⁵ with (a) 0 s and (b) 10 s of pause, and for (c) (HL)¹⁵ structure with 10 s of pause.

400°C . A subsequent oxidation step at 600°C promotes the PBG shifts to 422, whereas at 800°C the PBG shifts to 392.5. The increment in temperature to 1000°C yields a blueshift of the PBG to wavelength ranges below the measurement range left edge of the equipment ($< 350\text{ nm}$), therefore it disappeared from the reflectance spectrum. Comparable behavior is observed after the different thermal oxidation steps of the device fabricated with 10 s of etch-stop time, S5, which was at 938 nm for the as-etched sample, was then blue shifted to 676 nm at 1000°C .

On the other hand, in the case of the sample having the HLHL...HL configuration and yielded using 10 s of etch-stop (S8), the PBG position for the as-etched condition was at 993 nm, but it is blue shifted to 867.5 nm at 1000°C . However, comparing the sample S5 and S8, yielded and oxidized under the same conditions, the latter sample shows a more pronounced change of its PBG width (Figure 33c), suggesting a loss of refractive index contrast and, thus, revealing differences in their microstructural features. This fact shows the importance of the porosity of the first upper layer of the periodic stack in defining the microstructural features.

Figure 34 shows the effect of oxidation temperatures on the rate of the FWHM of PBG and the center of the PBG determined from the reflectivity spectra. For both devices, the PBG center and FWHM follow an exponential fit. However, the $\Delta\lambda/\lambda$ behavior of the devices shows significant differences from each other. While the change tends to be minimized for sample S6 and remains independent of the oxidation temperature, there is a tendency for the PBG width to contract further for the devices fabricated with the

etch-stop time, leading to an abrupt drop at 800°C. Of course, this change implies a dramatic change in the OT, i.e., a change in thickness or refractive index or even both simultaneously. Previous work has reported that during oxidation not only the effective refractive indices of the single H and L layers contract due to the presence of SiO₂ but also the possible contraction-expansion phenomena [72][86]. Moreover, according to the literature [73][71][87], the oxidation rate is strongly dependent on the characteristics of the porous microstructure so that a more porous structure undergoes faster oxidation, i.e., complete oxidation is easily achieved in this type of structure. However, since S5 and S8 didn't exhibit a saturation tendency, this resulted in incomplete oxidation, although there is a loss of refractive index contrast across the width of the PBG. In view of this, the porous structure of the 1D-PSPC of samples S5 and S8 appears to be more porous than S6 during thermal oxidation. This fact is reinforced by the $\Delta\lambda/\lambda$ contraction of S5 and S8, as it depends only on the n_L and n_H contrast, Equation (2.28). While the PBG width of S6 remains almost constant with respect to temperature, it shrinks further in the case of samples S5 and S8.

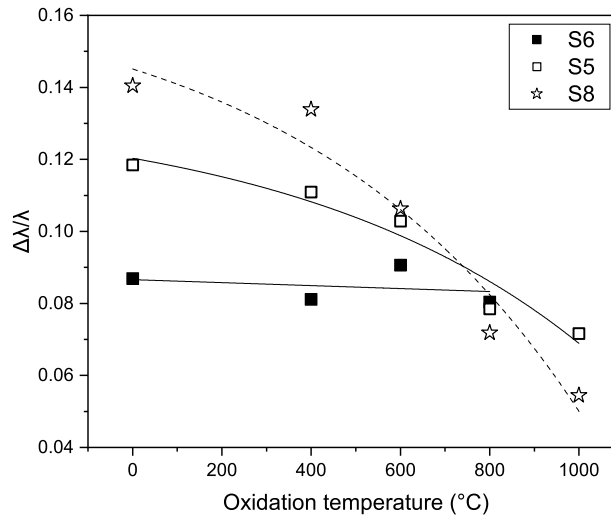


Figure 34 – Relationship between photonic bandgap width and photonic bandgap center position as a function of oxidation temperature for 1D-PSPC samples with $(LH)^{15}$ structure: S6 (0 s) and S5 (10 s), and $(HL)^{15}$ structure: S8 (10 s).

The blue shift of the PBG is related to the decrease in n_{eff} [88] of the complex system formed by Si, air, and SiO₂ (1D-PSPC:SiO₂), since the refractive index of SiO₂, n_{SiO_2} , along the wavelength measurement range is lower than that of silicon, n_{Si} (Figure 32), therefore the n_{eff} of the passivated system is lower. During the oxidation, the conversion of Si to SiO₂ takes place. For the analysis of this three-phase system, Astrova et al [89] propose that an x fraction of Si is converted to SiO₂, which occupies a volume of $2.27x$ [89]. Assuming that the system is homogeneous and completely oxidized, the new composition of the passivated layer gives a Si fraction = $f-x$, a SiO₂ fraction = $2.27x$,

and a pore fraction $p = 1 - f - 1.27x$. Although n_{Si} is wavelength dependent, some insight into the oxidation process can be gained by using the Bruggeman Equation (2.36) for the constants $n_{Si} = 3.607$, $n_{SiO_2} = 1.471$, and $n_{air} = 1.0$ at 900 nm. Using this strategy, it was possible to determine the degree of Si oxidation ($s = x/f$), defined as the ratio of the oxidized fraction to its original content in the PS layer [89], thus defining the porosity of the passivated porous layer. Figure 35 shows the calculated dependence of s and the n_{eff} of the system composed of Si, air, and SiO_2 for different initial porosities. For a porous matrix with a porosity of about 57% or more, the carcass of the porous matrix could undergo complete oxidation, leading to pores partially filled with SiO_2 , resulting in a final porosity of 5.5%. Porous layers with an initial porosity of less than 57% are subject to incomplete oxidation. With this in mind, and comparing the results of S5 and S8 from Figure 34, the reason for which the $\Delta\lambda/\lambda$ ratio of S8 drops faster indicates that this sample is more porous. This result and the fact that the first upper layer is H indicate that both factors are key to improving not only HF diffusion during pore formation but also oxygen diffusion during thermal oxidation, allowing faster oxidation.

4.4.2 Passivation by gold nanoparticles deposition

4.4.2.1 Single layers

As seen in section 4.1, fresh L-single layers (samples S14 and S15) and H-single layers (samples S16 and S17) were optically characterized. These samples were stored in

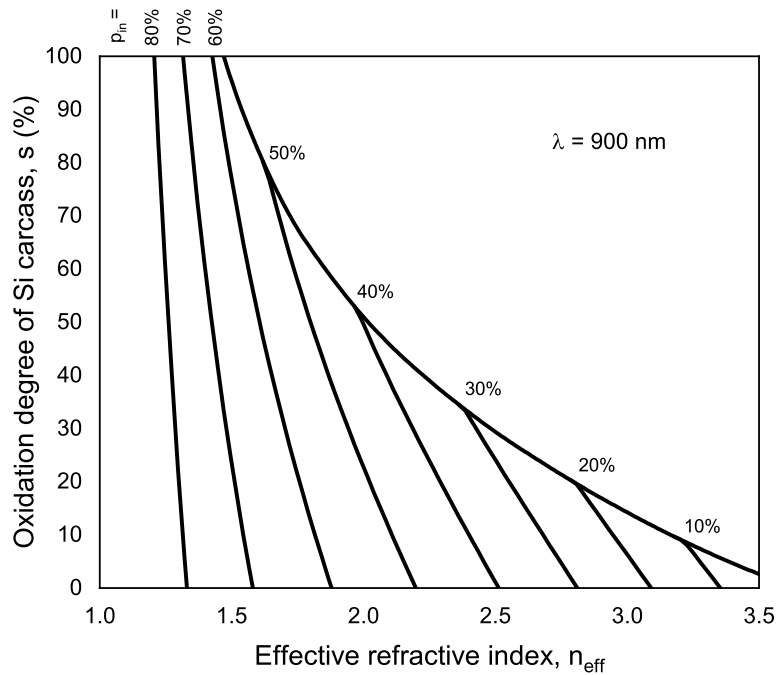


Figure 35 – Calculated dependence of porous silicon oxidation degree with the effective refractive index of PS layers passivated SiO_2 for various initial porosity.

air for almost two weeks without any special protection, so that the reflectance spectra marked by the black solid line in Figure 36a and Figure 37a correspond to the aged samples. The yellow and red curves were measured after the deposition of 60 nm of Au and subsequent thermal treatment, respectively. These reflectance spectra were analyzed using the FFT method for S14 and S15 (Figure 36b). A similar analysis was performed for samples S16 and S17. The reflectance spectra of the aged and treated surfaces are shown in Figure 37a, while Figure 37b shows the corresponding FFT analysis.

The deposition of Au onto PS was performed by sputtering for 60 s. The presence of Au in the PS microstructure is detected in the reflectance spectra (Figure 36a) by the shift of the interference fringes with respect to the aged PS and also by the increase of the reflectance intensity for wavelengths below 500 nm. This fact could be the result of surface plasmon resonance (SPR) [90]. FFT analysis shows a decrease in OT from 4891 to 4165 nm after Au coating in sample S14, for example. Since the thickness was not changed, this shift can only be attributed to the decrease in n_{eff} due to the presence of Au in the porous matrix. The refractive index of Au is lower than that of silicon and comparable to that of SiO_2 . Similar behavior was observed for the other L and H layers, as shown in Figures 36 and 37. However, in the case of sample S17, anomalous behavior is observed after Au deposition and sintering at 900°C , suggesting the formation of some Au-Si-O-based compounds with a larger effective refractive index or the formation of a

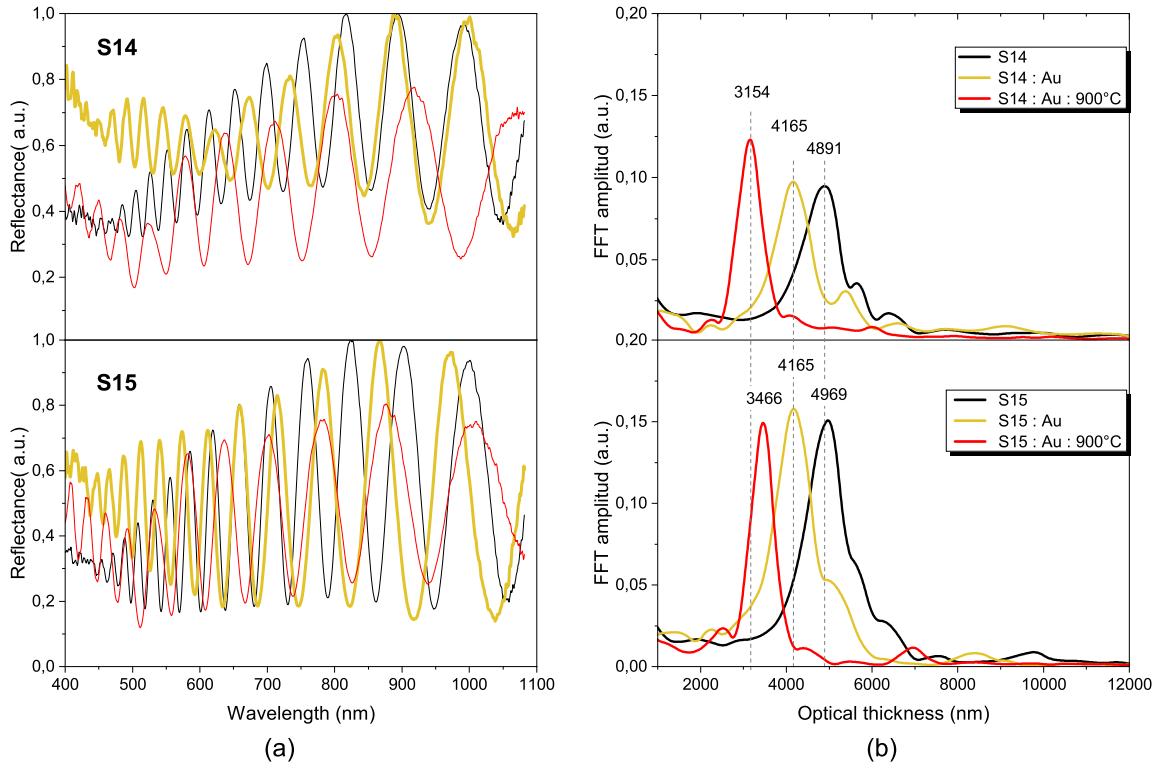


Figure 36 – (a) Reflectance spectra and (b) RIFTS of PS single layer with low porosity of samples: S14 (type I) and S15 (type I and 10 s of etch-stop time).

thicker layer. In this sense, Astrova et al. [89] and Zheng et al. [87] showed that oxidized porous silicon increases its thickness due to the expansion effect of the porous structure associated with SiO₂ growth.

According to Figures 36 and 37, the reflectance spectra of all samples after thermal sintering show a dip around 500 nm, which is called λ_{SPR} . This singular phenomenon was attributed to the contribution of the imaginary part of the refractive index (extinction coefficient, κ), as it has a larger value than the real part, which is due to the formation of surface states at the interface between Si-Au and Au-air. The inclusion of gold nanoparticles (Au NPs) in the PS structure leads to an increase in the surface roughness of PS due to the random arrangement of Au NPs [82]. In fact, the locations where the Au NPs could be located are limited to the density of the dangling bonds of the Si surface and within the pores, where the excitation wavelength of the resonance of the Au NPs depends on their size, shape, and external dielectric environment [90][91].

After Au deposition, the four samples were thermally oxidized in air at 900°C for 5 minutes. The reflectance spectra of the L layers, shown as a red solid line in Figure 36a, show different interference fringes, indicating good diffusion of Au after annealing, which is confirmed by EDS, XRD, and FFT analysis, as well as by the blue shift of the OT of both samples. For the H-layers, shown in Figure 37a, sample S16 shows the same behavior as the L-layers with an improvement in the optical response due to better

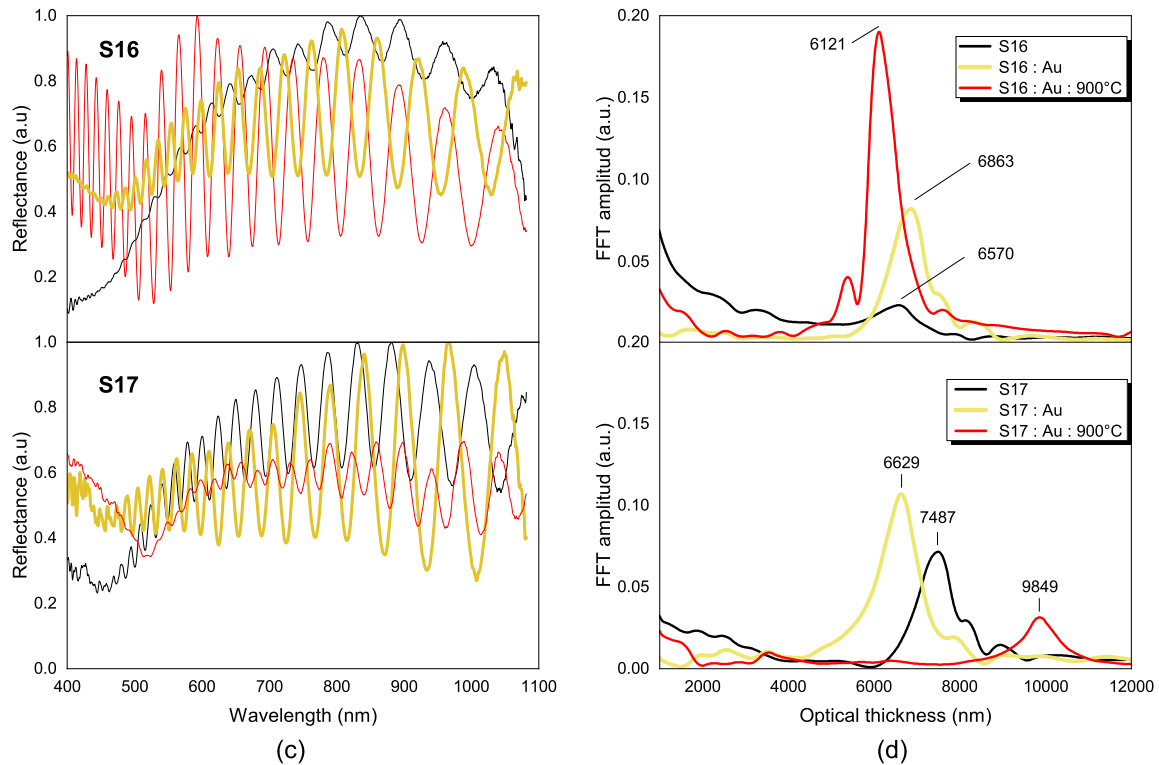


Figure 37 – (a) Reflectance spectra and (b) RIFTS of PS single layer of the high porosity of samples: S16 (type I) and S17 (type I and 10 s of etch-stop time).

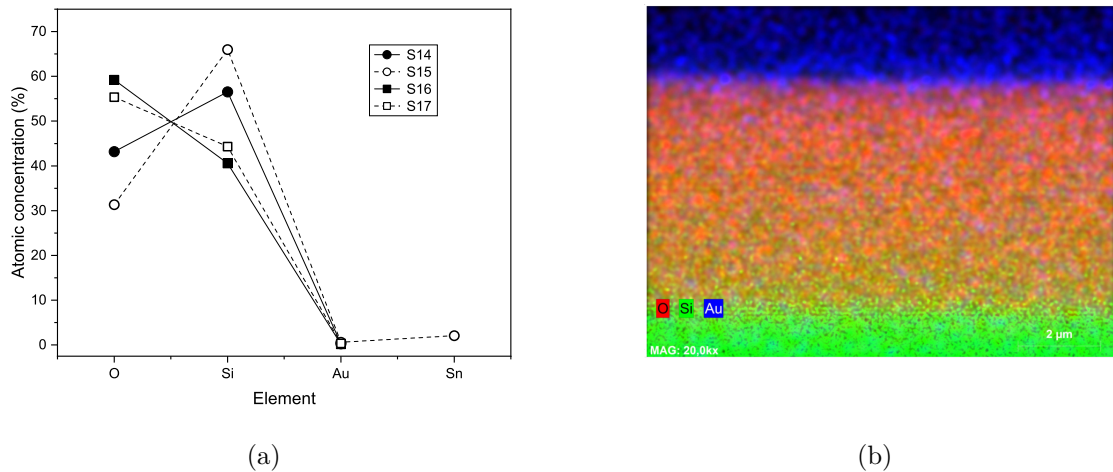


Figure 38 – (a) Semi-qualitative energy dispersive X-ray spectroscopy results (EDS) after Au deposition and thermal treatment at 900° for 5 min of porous silicon single layers anodized with electrolyte type I for L porosity: S14 (0 s) and S15 (10 s), and H porosity: S16 (0 s) and S17 (10 s). (b) EDS map of S16.

diffusion of Au, while the OT of sample S17 shows an increasing trend if compared with sample S16. This behavior is attributed to the diffusion of Au in a simultaneous way to the SiO_2 formation during the sintering process, allowing the possible distribution of Au onto the pore surface, creating a thin Au nanoparticles region that causes the red shift of the OT. This affirmation is observed in Figure 38b, in which is also observed that the Au concentration is greater in regions closer to the PS/air interface. In the EDS mapping spectra (38b), the silicon phase is identified as green, red is oxygen, and blue is gold. The formation of a thin Au film is clearly visible at the top of the structure as a faint blue region inside the porous matrix. However, it is important to emphasize that the large blue region above the PS structure observed in Figure 38b, in the order of 1/3 of the single layer, is an undesirable equipment artifact, since the nominal Au thickness was projected to be about 60 nm.

On the other hand, XRD analysis (Figure 39) shows the peaks at 38.2° , 44.4° , and 64.7° corresponding to the (111), (200), and (220) crystallographic planes of the face-centered cubic lattice of Au [92], while the peaks at 69.2° and 29° correspond to Si in the (400) phase and the latter in the amorphous phase transition to (111) [93], respectively. Similar XRD patterns were also observed for all samples containing Au nanoparticles.

4.4.2.2 Multilayers: 1D-Photonic crystals and cavities

Fresh 1D-PSPCs labeled as S22 and S27 were prepared with the same electrochemical parameters of current density using etching time I and electrolyte type I by inserting 8 and 5 s of etch-stop, respectively. Both samples were optically characterized before and after passivation with a thin Au layer and after thermal treatment. Reflectance spectra

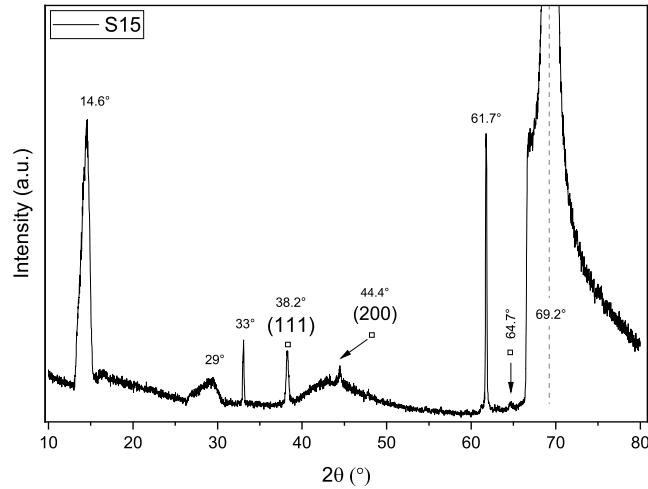


Figure 39 – X ray diffraction pattern of low PS: Au: 900°C. Square symbol signs the Au pattern.

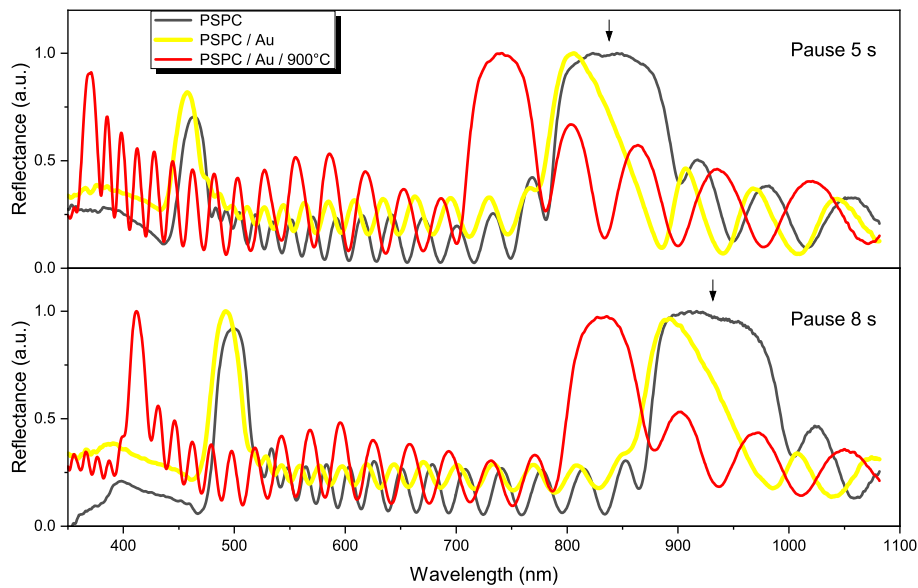


Figure 40 – Reflectance spectra for porous silicon photonic crystals in the initial state (black) using electrolyte type I and etching time I, with physical deposition of Au (yellow) and oxidized at 900°C for 5 min at (a) 5 and (b) 8 s etch-stop time.

are shown by solid black lines for the as-etched devices and by yellow lines for the devices after passivation with 60 nm Au. The curves in red lines correspond to the optical response after thermal sintering at 900°C for 5 minutes (Figure 40).

These spectra show us that the main effect of the Au thin film on the optical spectra is a slight blue shift in its central position and a deformation of the PBG features. After sintering, the PBG shape is relatively recovered, although its position is shifted more to the short wavelength region. According to Bragg's law, Equation (2.29), this behavior is associated with changes in the OT of each single layer composing the 1D-PSPCs.

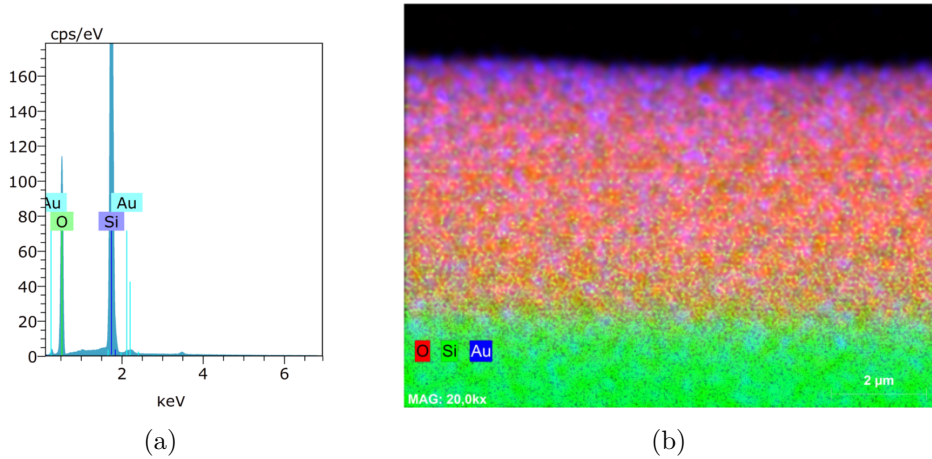


Figure 41 – *Semi-qualitative results of energy dispersive X-ray spectroscopy (EDS) after deposition of Au and thermal treatment of 1D-PSPC of sample S22 (a) elemental qualitative and (b) EDS map.*

Assuming that the physical thickness does not change, the presence of Au and other Au-based compounds formed after sintering leads to changes in the effective refractive index of the H and L layers. However, this change is not homogeneous in-depth since EDS analysis (Figure 41) indicates a higher Au concentration at the upper region. The peaks in Figure 41a show that the total concentration of Au along the surface is about 3%.

In the case of the 1D-PSPC covered with Au (1D-PSPC: Au), the system consists only of silicon, gold, and air. For rapid analysis, a nominal thickness of about 60 nm was deposited on the 1D-PSPC, and considering the complex refractive index for 53 nm of Au reported in the literature, n_{Au} , (Figure 32), it is found that the real part of n_{Au} along the reflection measurement range is lower than n_{Si} , consequently the effective refractive index of a system (n_{eff}) consisting only of silicon and gold will be lower in the order of porous H and L layers. After the inclusion of Au in the pores, the n_{eff} of the porous H and L layers decreases. The slight blue shift is explained by the assumption that Au is in the first upper H and L layers after deposition (Figure 42), so only these layers undergo changes in their n_{eff} . The amount of Au in the middle and lower H and L layers is negligible. This fact also explains why the PBG is only partially deformed. Since the Au-containing H and L layers do not change according to Bragg's law, but n_H and n_L are reduced, destructive interference fringes appear on these layers at a certain wavelength, leading to PBG deformation.

To avoid this anomaly in the optical response caused by the presence of the Au thin film on the surface, both samples S22 and S27 were thermally oxidized in air at 900°C for 5 minutes. According to Font and Myers [94], since this temperature is above the Au thin film melting point depression, diffusion of Au from the surface into the 1D-PSPC matrix occurs, forming Au nanoparticles or even compounds based on the combination of Au, Si, and oxygen. However, even after this thermal treatment, the EDS maps (Figure

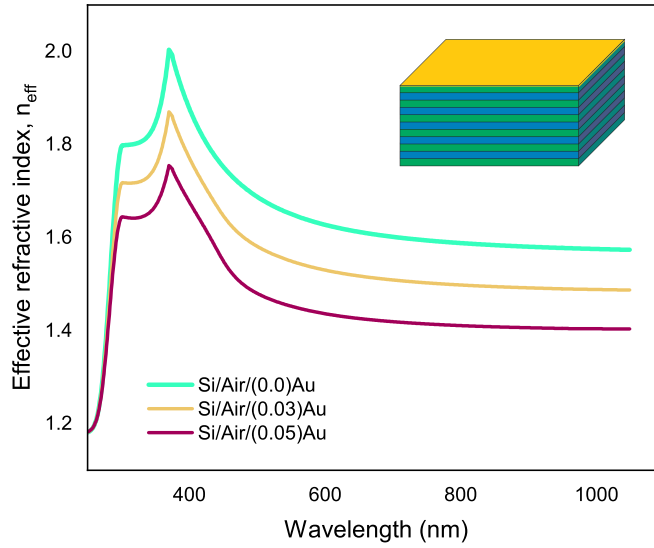


Figure 42 – Calculated dependence of the effective refractive index on the wavelength in a system composed of air, gold and porous silicon with an initial porosity of 70%.

41b) reveal a larger concentration of Au in the surface region. In this map, the different elements are highlighted by green for silicon, blue for gold, and red for oxygen. Considering that the optical response of both samples is reasonably fitted with the theoretical values for H and L layers with homogeneous porosity (Figure 20a), the only reason for the deviations from these spectra is the occurrence of this in-depth porosity gradient. The partial PBG recovery can be understood by assuming that SiO_2 formation predominates in the porous structure of the photonic devices. Moreover, the main effect of n_{Au} is noticeable for wavelengths below 550 nm (Figure 32). Due to this factor, the PBG of the devices after thermal treatment appears not only blueshifted but also narrow and well-defined PBG.

The predominance of SiO_2 in this 1D-PSPC: Au device is also confirmed by the expansion-contraction of the H and L layers. Previous work studied by Pap and Barla [72][86] reported this behavior associated with the complete oxidation of these layers. In our case, the quantification of this expansion-contraction was done by comparing the thickness of the H and L layers extracted from the fitting task of the reflectance data of these samples with the thickness measured from SEM images after thermal treatment. For example, the thickness of the H layers of S22 is 210 nm in the as-etched device and shrinks to 162 nm after thermal treatment. The expansion of the L-layers from 70 to 151 nm was measured, resulting in a global expansion of the device thickness from 4200 nm in the as-etched to 4700 nm after passivation.

The complex system is described as a four-component medium consisting of Si, SiO_2 , Au, and air (1D-PSPC: Au: SiO_2). During oxidation, a x part of Si is converted to

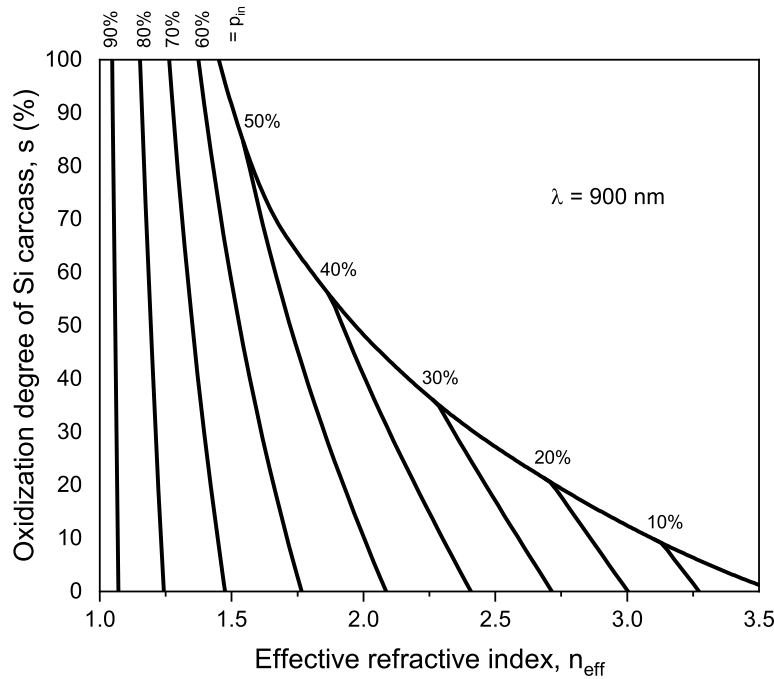


Figure 43 – Calculated dependence of the degree of oxidation of porous silicon with the effective refractive index of PS layers passivated with Au and SiO₂ for different initial porosities. The volume fraction of gold is 0.03

SiO₂, occupying a volume of 2.27x [89]. Assuming a homogeneous distribution of Au, the passivated structure is composed of (i) Si fraction = $f - x$, (ii) SiO₂ fraction = 2.27x, (iii) Au fraction = p_{Au} , and (iv) the pore fraction $p = 1 - f + x - p_{Au} - 2.27x$. Solving Bruggeman's Equation (2.36) for the constant refractive index at 900 nm: $n_{Si} = 3.607$, $n_{SiO_2} = 1.471$, $n_{Au} = 0.186$, and $n_{air} = 1.0$, it's possible to determine the porosity of the porous layer (1D-PS: Au: SiO₂) and its corresponding n_{eff} in a wide range of initial porosity. Figure 43 shows the calculated dependence of the degree of oxidation of the silicon carcass, i.e., the ratio between the oxidized fraction and the initial Si fraction, and the n_{eff} of the 1D-PS: Au: SiO₂. Porous layers with low initial porosity change n_{eff} over a wide range, making them more sensitive to oxidation and losing the porous property before they're fully oxidized. The line through the graph connecting the maximum points corresponds to the medium PS with an Au content of 3%, so the system remains porous at an initial porosity greater than 55%. In the case of S22, the initial porosities are $p_L = 58\%$ and $p_H = 69.7\%$, leading to a range of final porosity between 4.2% and 54.4% for L, and the final porosity for H is in the range between 36.4% and 68.2%.

Figure 44 shows the XRD pattern of 1D-PSPC: Au: 900°C devices (S22 and S27). In these spectra, the peaks at 29°, 33°, 61.7°, and 69.2° correspond to the silicon phase and are well defined in the device fabricated with 5 s of pause, while their absence in the sample yielded using 8 s of pause is associated to the setup reconfiguration to avoid them and highlight those that correspond to the Au phase. As already mentioned, the

peaks at 38 , 44.4 , and 64.7° are associated with the presence of Au nanoparticles. It is important to emphasize that the bump around 44.4° seems to be related to the presence of the amorphous phase of SiO_2 .

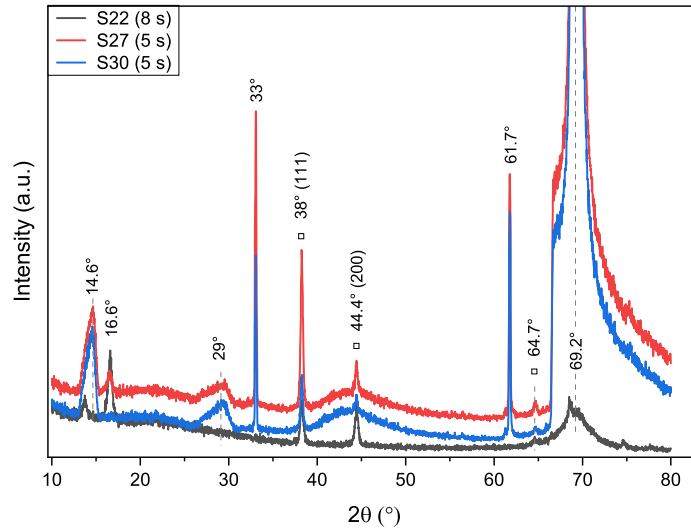


Figure 44 – *X ray diffraction pattern of 1D-PSPC: Au:900°C (S22 and S27), and 1D-PSPC:900°C :Au:900°C (S30). Square symbol signs the Au pattern.*

On the other hand, the 1D-PSPC-Mc of sample S26 prepared by the etch-stop method with 5 s of pause and corrosion characteristics of time I and type I is shown in Figure 45. The cross-section SEM image shows the periodic structure composed of L and H layers (gray and black, respectively) and the microcavity in the center projected to $d_c=2d_H$.

The reflectance spectra for the as-etched devices are shown in black solid line in Figure 46, while the device after passivation of 60 nm Au are shown in yellow line and the curves in the red solid line correspond to the optical response after thermal annealing at 900°C for 5 minutes. The position of λ_c is marked by the black arrow and shows a blue shift of λ_c and a deformation of the PBG feature. As with the 1D-PSPC, we investigated whether the incorporation of Au into the 1D-PSPC-Mc (1D-PSPC-Mc: Au)

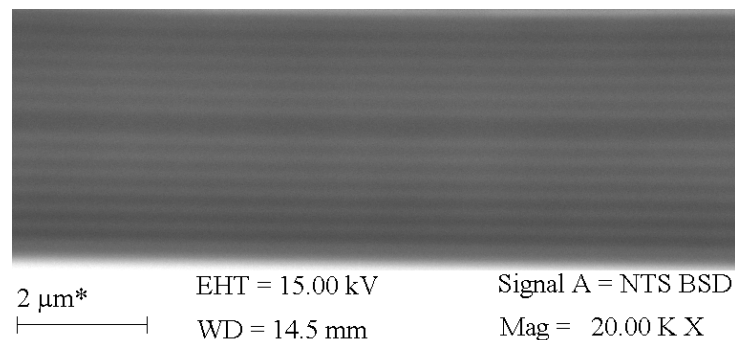


Figure 45 – *Scanning electron microscopy of 1D-PSPC-Mc S26, with 5 s of etch-stop time.*

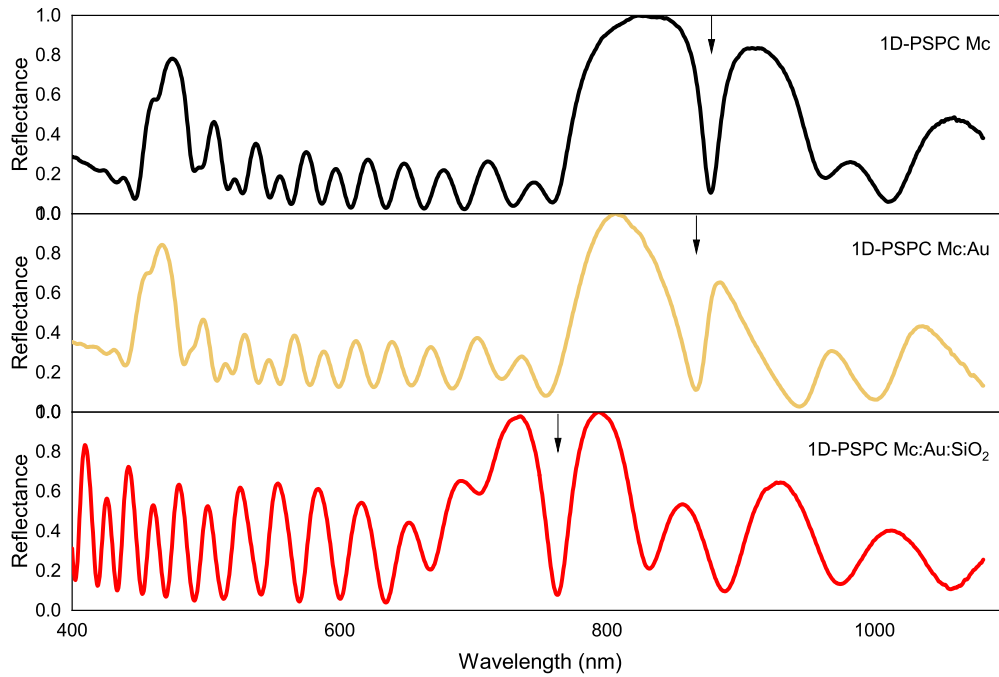


Figure 46 – Reflectance spectra of sample S26 for as-prepared porous silicon photonic crystal (black), with physical deposition of Au (yellow) and oxidized at 900°C (red) for 5 minutes.

caused destructive interference fringes due to the surface location of the Au thin film. Sample S26 was thermally oxidized in air at 900°C for 5 minutes to diffuse Au from the surface into the porous matrix. The EDS map still shows the Au concentration at the surface of the device, in blue for Au, while Si is highlighted in green and oxygen in red. However, the map of S26 (Figure 47b) shows a higher diffusion of Au into the device, in counterpart to the 1D-PSPC: Au: SiO₂ of S22 (Figure 41b), this is because the 1D-PSPC-Mc was paused with 5 s, which produces higher porosity, and the low concentration of Au, on the order of 3%, despite the EDS map showing more concentration of Au than S22, this is because the EDS it's a point-by-point technique to obtain the atomic concentration. This is because all these facts allow a better diffusion of Au, resulting in a higher shift of λ_c after annealing.

On the other hand, the XRD patterns of 1D-PSPC-Mc devices (samples S31-S33) show the characteristic XRD spectra of Au and Si phases in Figure 48. After thermal treatment, the peak intensity at 38.2° shows the concentration enhancement of Au nanoparticles with crystallographic orientation (111). The absence or even the low intensity observed in the peak corresponding to the (200) planes suggests the formation of lower concentrations of Au (200), although both 1D-PSPCs and the microcavities were sintered under the same conditions. This fact could be associated with the possible non-homogeneous distribution temperature in the furnace.

Figure 49 shows some images before and after treatment of the 1D-PSPC-Mc. For

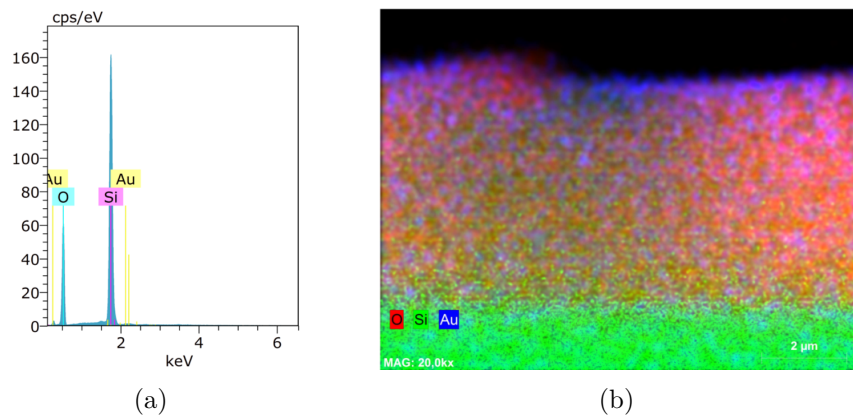


Figure 47 – Semi-qualitative energy dispersive X-ray spectroscopy results (EDS) after Au deposition and thermal treatment of 1D-PSPC Mc of sample S26 (a) is the qualitative elemental representation and (b) shows the EDS map.

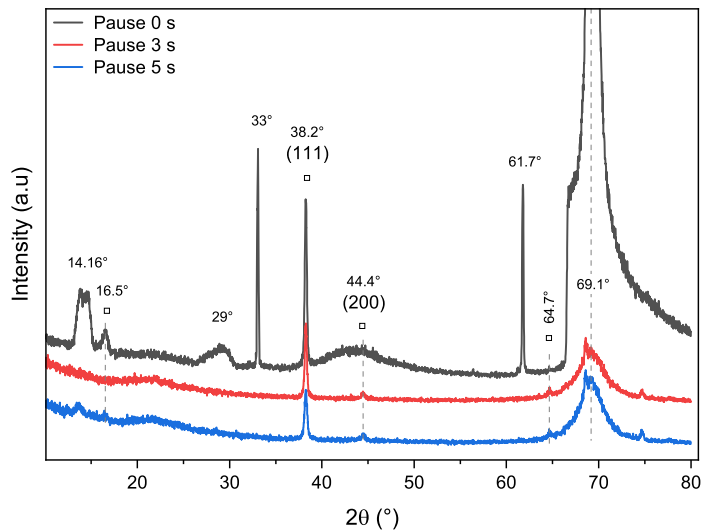


Figure 48 – X ray diffraction pattern of 1D-PSPC-Mc: Au:900°C. The square symbol signs the Au pattern.

the as-etched samples, the optical response of Figure 26 was taken in the center of each sample. The colored area near the sample edge, like concentric rings, is indicative of the nonhomogeneous formation of the lateral pore distribution along the whole sample. This fact is a typical feature in PS associated with the non-homogeneous distribution of the current density during pore formation [48][9]. Figure 49b, on the other hand, shows the optical effect after the incorporation of Au NPs and thermal annealing in the photonic devices due to Au diffusion through the porous matrix (for comparison, see the thin layer on the silicon substrate), and is clearly see the blue shift of the PBG due to SiO_2 formation.

4.4.3 Passivation by Titanium dioxide: multilayer structures with resonant cavity

The fresh 1D-PSPC-Mc devices (samples S40 to S45 in Table 11) with reflectance spectra shown in Figure 30 were embedded in a solution gel (sol-gel) of TiO_2 for passivation for 1 week. The optical behavior of the TiO_2 deposited devices is shown in Figure 50. A quick naked-eye analysis shows that, unlike the samples passivated with Au, both the PBG

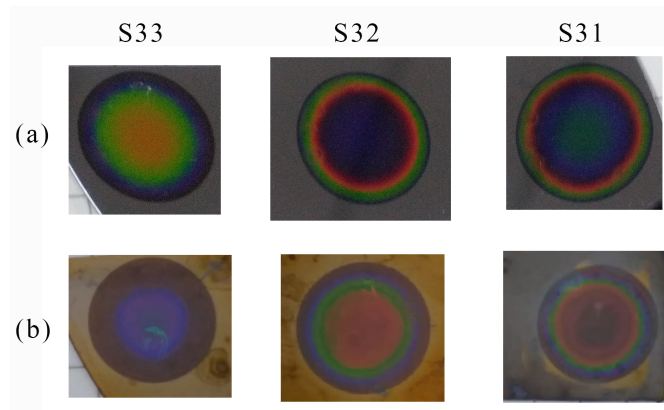


Figure 49 – Photonic crystal with a resonant cavity containing gold nanoparticles for 0, 3 and 5 s of pauses in the following order (a) 1D-PSPC-Mc (b) 1D-PSPC-Mc:900°C.

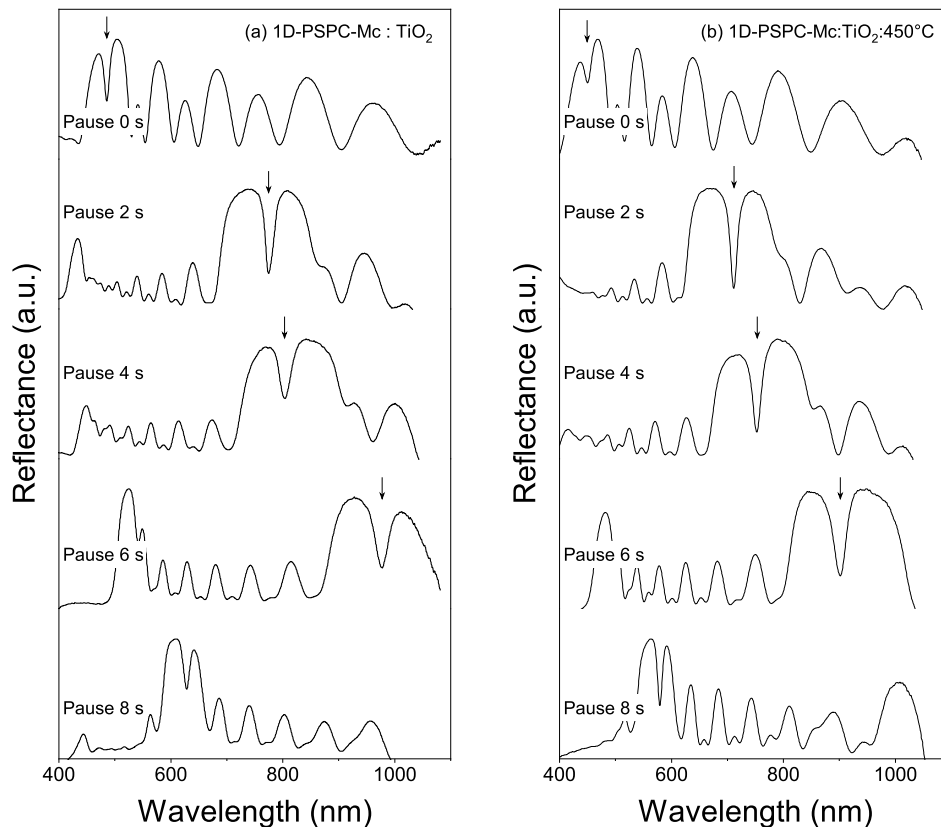


Figure 50 – Shift in reflectance spectra of samples S40-S45. (a) 1D-PSPC-Mc with TiO_2 deposition and (b) after thermal annealing for different etch-stop times.

Table 13 – Comparison of the position of the microcavity based on the reflectance spectra of Figure 30 and Figure 50.

Samples	Break (s)	As-etched (nm)	1D-PSPC Mc:TiO ₂ (nm)	1D-PSPC Mc:TiO ₂ :450°C (nm)
S40	0	486.8	485.2	448.2
S45	2	741.0	776.3	711.3
S42	4	802.2	803.9	751.9
S43	6	953.5	977.6	900.3
S44	8	-	-	-

and microcavity features are preserved after TiO₂ passivation, but the PBG position of some samples (S45 and S43) is red shifted, as summarized in Table 13, while the shift for the others is negligible and within experimental error. The position of the cavity is denoted by λ_c and marked by black arrows in Figure 50a.

To understand this ambiguous behavior, one must consider that the as-passivated devices are composed of Si, air, and TiO₂. However, considering that TiO₂ has a lower refractive index than Si (Figure 32), a blue shift in PBG and microcavity position of all samples is expected after passivation (Figure 53). However, Figure 50a shows us the opposite behavior. This redshift and also the non-displacement of the PBG can be explained by assuming that the pores were completely filled with sol-gel TiO₂ solution, which leads to a redshift because of its refractive index is larger than that of air, since sol-gel TiO₂ is composed of xylene, water, and titanium butoxide (IV). Similar behavior is observed when 1D-PSPC or microcavities are filled with organic solvents [70]. Pacholsky [88] says that for samples with unshifted PBG, this is because the pores are not filled by the solution, i.e., the TiO₂ sol-gel forms a thin sealing layer, keeping the pores unfilled, so the optical response remains unshifted. This is the reason that λ_c remains almost in the same place within the experimental error 52a.

To remove any impurities that might originate from the TiO₂ sol-gel, such as trapped molecules in the surface (Figure 51a) or porous matrix (Figure 55b), the five devices were thermally annealed in air environment at 450°C for 15 minutes. The reflectance spectra of Figure 50b show an enhancement of the transmission band of samples S45, S42, and S43, and the position of λ_c (Table 13) clearly shows the blue shift of the resonance peak as a result of the formation of SiO₂ and the calcination of organic impurities from the TiO₂ sol-gel during the thermal treatment. According to the FTIR analysis (Figure 55c), the organic impurities were eliminated after the thermal treatment.

After this passivation treatment, the complex system is described as a medium with four components: Si, SiO₂, TiO₂, and air (1D-PSPC-Mc:TiO₂:SiO₂). The study followed the same procedure as for the gold-passivated 1D-PSPCs. As for the non-reaction of TiO₂ after thermal annealing, the only phases that change are silicon, which converts to

SiO₂. For this condition, and assuming $\sim 14\%$ of TiO₂ inside the pores, the theoretical results of the degree of oxidation of silicon are shown in Figure 54. This figure should be interpreted in the following sense: If the initial porosity of the PS layer is higher than 48%, the system remains porous even after complete oxidation. For layers with porosity lower than 48%, the porous structure could be filled up and consequently, the porous structure is transformed into a nanocomposite. However, this depends on the oxidation temperature. When the TiO₂ concentration is increased, the pores are naturally filled faster and thus the n_{eff} tends to increase [88]. The advantage of using TiO₂ as a passivation layer is the formation of a two-phase passivation layer after thermal treatment, which ensures a chemically stable porous surface, making this structure suitable for use as a sensor.

4.4.3.1 Complementary analysis for TiO₂ in multilayers: FTIR, EDS and XRD

The presence of TiO₂ within the pores was investigated by FTIR and EDS analysis. Since all 1D-PSPC-Mc were simultaneously subjected to passivation by immersion in a TiO₂-based solution, the FTIR of sample S40 is shown in Figure 55 as a representation of this group of devices, since analogous behavior was observed in the other samples. Figure 55a corresponds to the FTIR spectrum of the TiO₂-based liquid in which the samples were embedded. The labeled peaks between 2960 and 830 cm⁻¹ correspond to the isomers of xylene [95][96][97]. The peaks at 770 and 743 cm⁻¹ are associated with $\nu(\text{Ti-O})$ vibrations in multiphase TiO₂ [98], while the broad band at 3436 cm⁻¹ and the peak at 1638 cm⁻¹ belong to the -OH groups. In the case of the spectrum after one week of immersion (Figure 55b), the absence of peaks corresponding to the isomers of xylene is striking, leaving only

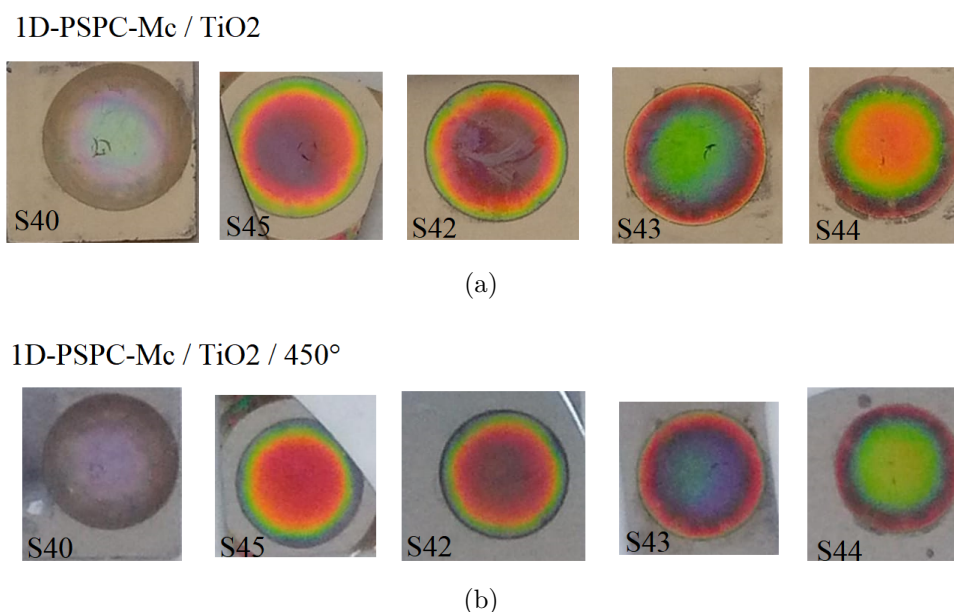


Figure 51 – (a) Images of the 1D-PSPC-Mc embedded with TiO₂. (b) Images of the 1D-PSPC-Mc embedded with TiO₂ and thermal annealing at 450° C for 15 min. Sample S40-S45.

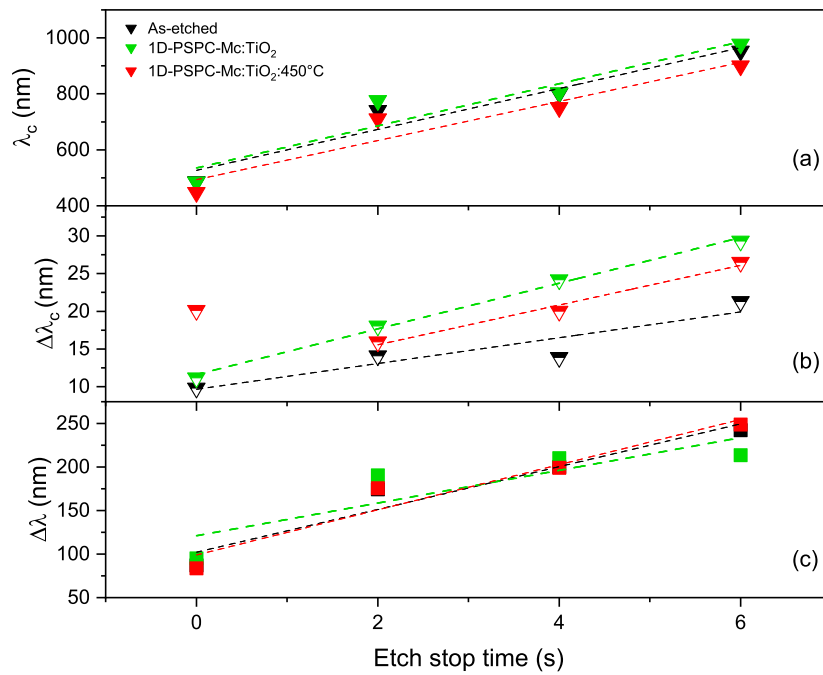


Figure 52 – Comparison curve of 1D-PSPC-Mc in the as-etched (black), with TiO_2 deposition (green), and after annealing at 450°C (red) for the (a) microcavity position, (b) FWHM of transmission band, and the (c) width of the PBG.

the broadband and the peak associated with the -OH groups. Moreover, the presence of the peak at 1038 cm^{-1} , which overlaps with that at 1104 cm^{-1} , indicates the coexistence of SiO_2 covering the pore surface and m-xylene forming the sol-gel layer. After thermal treatment at 450°C for 15 min, these peaks were suppressed, and the peaks associated

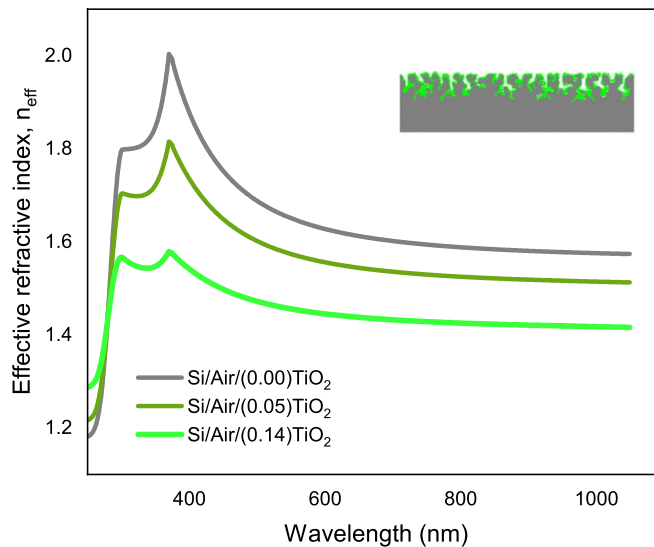


Figure 53 – Calculated dependence of the effective refractive index with a wavelength in a system composed of air, titanium dioxide, and porous silicon with initial porosity of 70%.

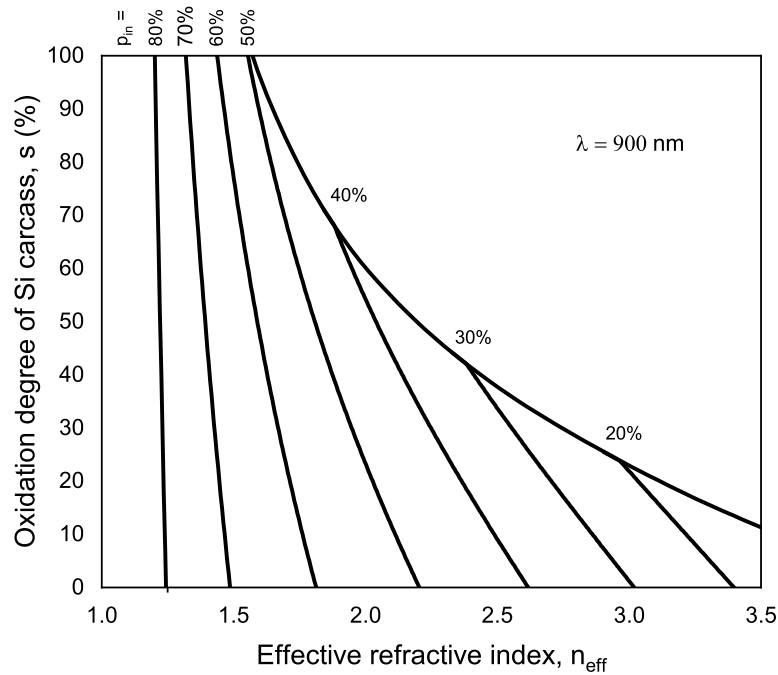


Figure 54 – Calculated dependence of porous silicon oxidation degree with the effective refractive index of PS layers passivated with TiO_2 and SiO_2 for various initial porosity. The volume fraction of TiO_2 is 0.138

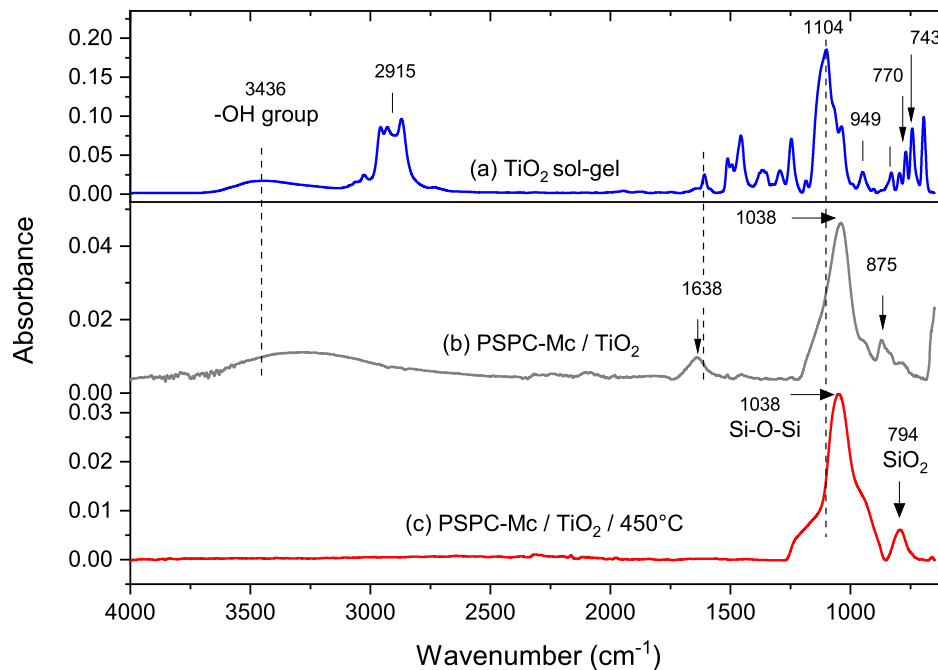


Figure 55 – Fourier transform infrared spectroscopy (FT-IR) of (a) TiO_2 sol-gel, (b) as-etched sample of 1D-PSPC-Mc (S40) embedded in TiO_2 by sol-gel method, and (c) after oxidized at 450°C for 15 minutes.

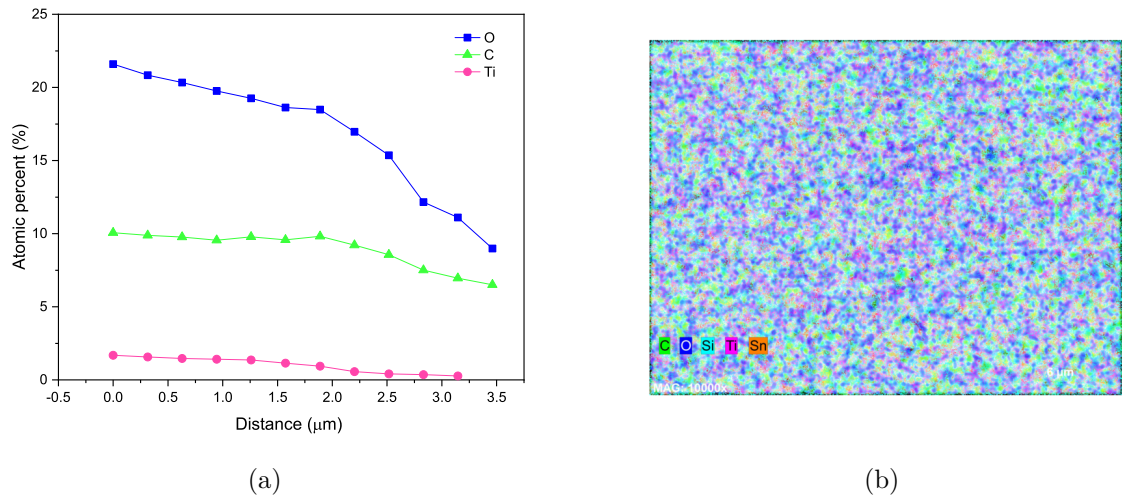


Figure 56 – Energy dispersive X-ray spectroscopy (EDS) of 1D-PSPC-Mc showing the (a) atomic percent at depth and (b) map of the surface of sample S45.

with the formation of SiO_2 appear well defined.

Although the presence of TiO_2 could not be detected by FTIR due to the resolution limits of the instrument (most peaks are below 600 cm^{-1} [99][100]), the formation of this compound within the pores after the thermal treatment was identified by EDS analysis, as shown in Figure 56. The cross-sectional analysis over the entire thickness of the device (from $0\text{ }\mu\text{m}$ to $3.5\text{ }\mu\text{m}$) shows that a larger and homogeneous concentration of TiO_2 is formed at the surface of the pores (Figure 56b), leading to the formation of a gradient in-depth not only in the TiO_2 concentration but also in the porosity and thus in the effective refractive index. However, as far as the distribution of the TiO_2 surface is concerned, the EDS map reveals an almost homogeneous distribution of Ti, O, and C on the whole surface (Figure 56b).

XRD analysis is of paramount importance for the identification of crystallographic features, such as the identification of phases and phase transitions in multiphase TiO_2 structures. Figure 57 shows the XRD patterns of the five devices (S40-S45). The peak at 69.23° corresponds to the Si [93]. The peaks at 61.85° , 68.79° , and 74.69° correspond to TiO_2 in the anatase structure of plane (204), (116), and (215) [101][102][99][98], the peaks at 44.29° and 61.85° indicate the (210) and (002) crystallographic planes of TiO_2 in rutile structure, respectively [98]. The peaks associated with TiO_2 -rutile indicate a phase transition, as the oxidation temperature was 450°C , and also the coexistence of anatase and rutile, as the peak at 61.85° is attributed to both phases, as reported by Verma et al. [98].

As mentioned above, some groups of samples were subjected to passivation by thermal oxidation and deposition of gold and TiO_2 , followed by thermal sintering in air at 900°C and 450°C , respectively. Optical stability was investigated by measuring the

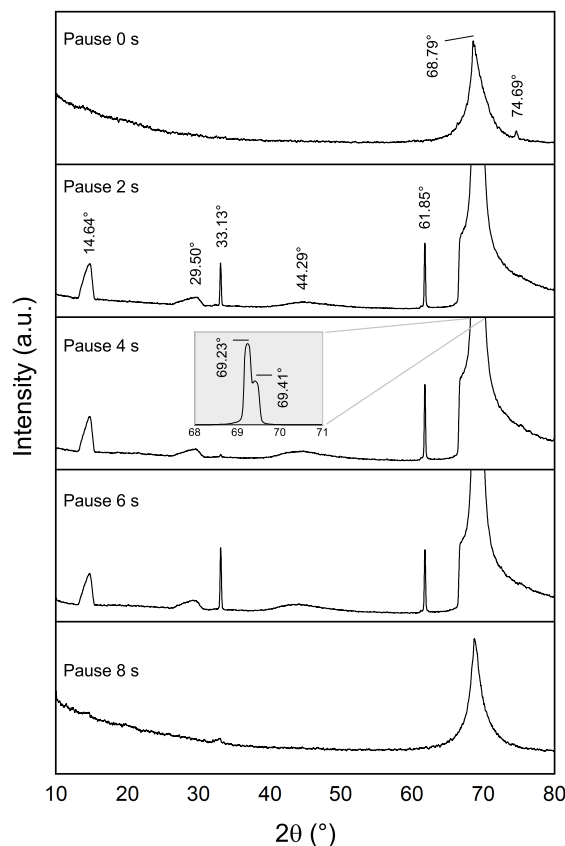


Figure 57 – Comparison of X-ray diffraction (XRD) of passivated devices with TiO_2 and thermally oxidized devices (a) S40, (b) S45, (c) S42, (d) S43, and (e) S44.

optical response of these passivated structures after 20 to 36 weeks of storage, and the results for some representative samples are summarized in Figure 58. The optical response of the storage-passivated samples is practically unchanged in the optical position, although some slight differences in intensity are observed, which can be attributed to difficulties in focusing the same porous region in both measurements.

The identification of molecular absorption and functional groups was confirmed by FTIR analysis. For the case treated by thermal oxidation (Figure 59a), the characteristic peaks at 1725 , 1103 , 1025 , and 792 cm^{-1} correspond to the $\text{C}=\text{O}$ stretching vibration [103], the asymmetric Si-O-Si vibration [104][105], the Si-O bond, and the Si-O-Si vibration, and extend to all devices that were thermally oxidized. The presence of carbon comes from the exposition to organic solvents (alcohols) used to verify the effect of passivation by reflectance spectroscopy (Figure 58). For the Au-treated devices, the FTIR spectrum shows similar absorption patterns as for the thermally oxidized sample (S39) (Figure 59b). The absence of an additional peak that could be associated with compounds from Au, Si, and O bonds suggests that no such compounds were formed or, if they were, the amount of compounds is below the sensitivity of the FTIR instrumentation. However, according to

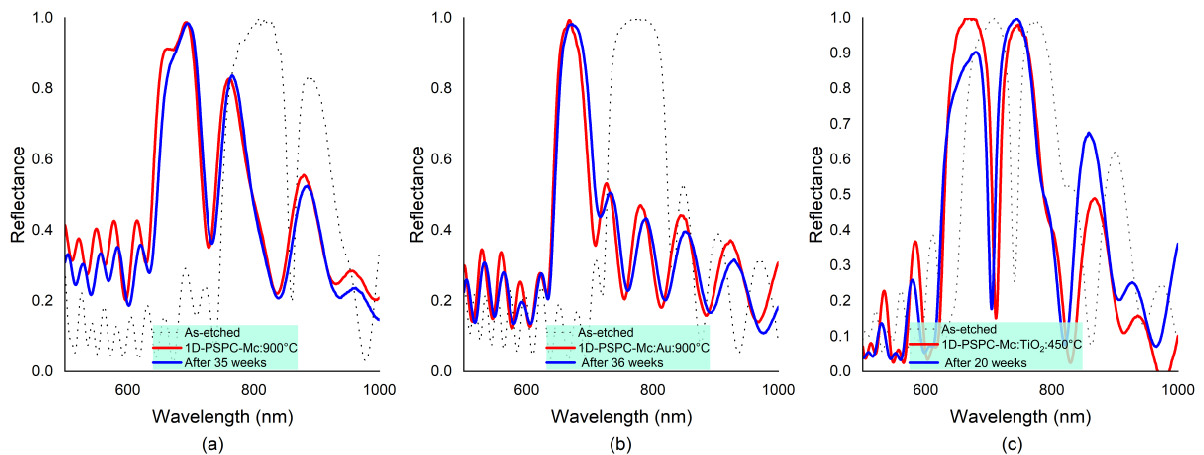


Figure 58 – Reflectance spectra of samples (a) S37, (b) S32 and (c) S45. In as-etched (dots), after treatment (red), and the verification (blue).

Bhau et al. [106], the peak around 1030 cm^{-1} (inset of Figure 59b) indicates the presence of gold nanoparticles within the porous structure, suggesting that Au diffuses into the porous structure after thermal treatment and forms these nanoparticles.

As for the device passivated with TiO_2 (Figure 59c), the presence of the large

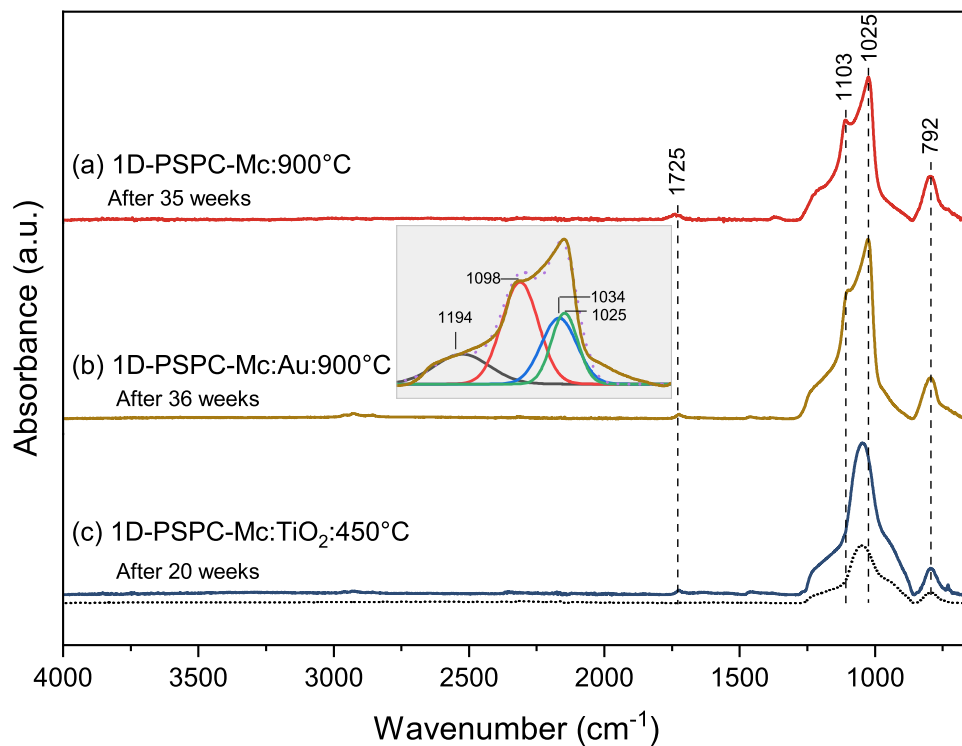


Figure 59 – Comparison of absorbance of devices passivated with (a) SiO_2 (S39), (b) Au and thermal annealing (S33), and (c) TiO_2 and thermal oxidation (S40); the curve in the black dots corresponds to FTIR immediately after passivation.

band around 1045 cm^{-1} is attributed to the asymmetric Si-O-Si stretching, and the right shoulder is due to the Si-OH stretching [107]. The presence of the hydroxyl group is attributed to the corrosion feature, as these devices were fabricated using electrolyte type II, which has H_2O in its composition. In addition, a comparison of the FTIR curves immediately after treatment (curve in black dots) and after 20 weeks of storage is shown. The FTIR curves confirm the passivation of this type of device. A similar profile confirms the passivation stability by TiO_2 .

4.5 Optical response of passivated devices in air and liquid media

Porous matrix, both single layers and photonic crystals exhibit a shift in the reflectance spectrum when immersed in different solvents, leading to a change in the n_{eff} of the constituents layers because the refractive index of the solvent is higher than that of air [88][69][108][68]. This feature makes PS suitable for applications as an optical sensor with faster response and no risk for handling volatile or flammable substances [109]. The main advantage of using microcavities for this objective is related to the position shift of the resonance peak. Similar behavior can be observed for a distributed Bragg reflector with narrow PBG[110][111].

For the case of single layers as an optical sensor, few works are reported [81]. This fact can be associated with difficulties in visual perception of reflectance data, since only the number of interference fringes or even their maximum position is observed. However, in this case, the OT changes in the FFT spectra can be used as a sensing element due to the presence of analytes [81][112]. Another way to calculate the OT is to use the slope of the linear curve m versus λ_m [38]. In this sense, Figure 60 shows the linear trend of OT as a function of the refractive indices of the solvents measured at the single layers S14 and S15. The following solvents were used as probes: Methanol (1.326), ethanol (1.359), heptane (1.387) and toluene (1.493). This measurement was performed in the as-etched devices (black symbols), with 60 nm Au (yellow symbols), and after sintering in air at 900°C (red symbols). The filled symbols correspond to OT, obtained by FFT, and the unfilled symbols correspond to OT, obtained from the slope of the fitting procedure. The red shift of the reflectance spectrum, and hence the increase in OT as a function of refractive index (Figure 60), is due to the refractive index of the solvent being larger than that of air.

The S14 device showed an acceptable optical response along the solvents, while the S15 immersed in toluene ($n = 1.493$) left the linear trend. This behavior was associated with the high volatility of this solvent, so this data was removed from the analysis. Comparing Figure 60a and b, it is noticeable that the sensitivity of S14 decreases after Au deposition, but increases again after sintering. Comparable results are observed for sample S15, despite the calculated OT method. This linear trend is also observed for the

unoxidized samples. This behavior is to be expected since the OT change is caused by the presence of the organic solvent in the pores.

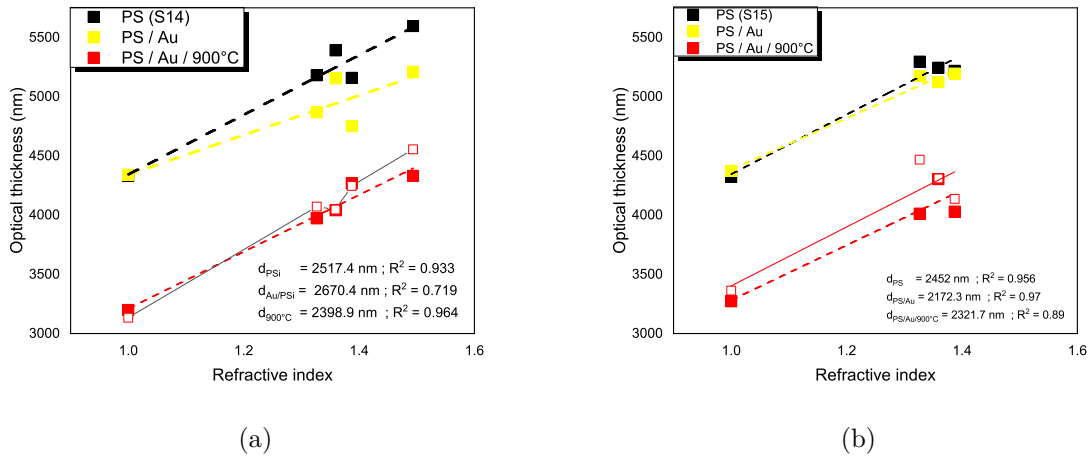


Figure 60 – Optical thickness of single PS layers as a function of the refractive index of the organic solvent in the as-etched devices (black symbol), after Au deposition of 60 nm nominal thickness (yellow symbol) and thermal sintering at 900°C (red symbol) for (a) S14 and (b) S15.

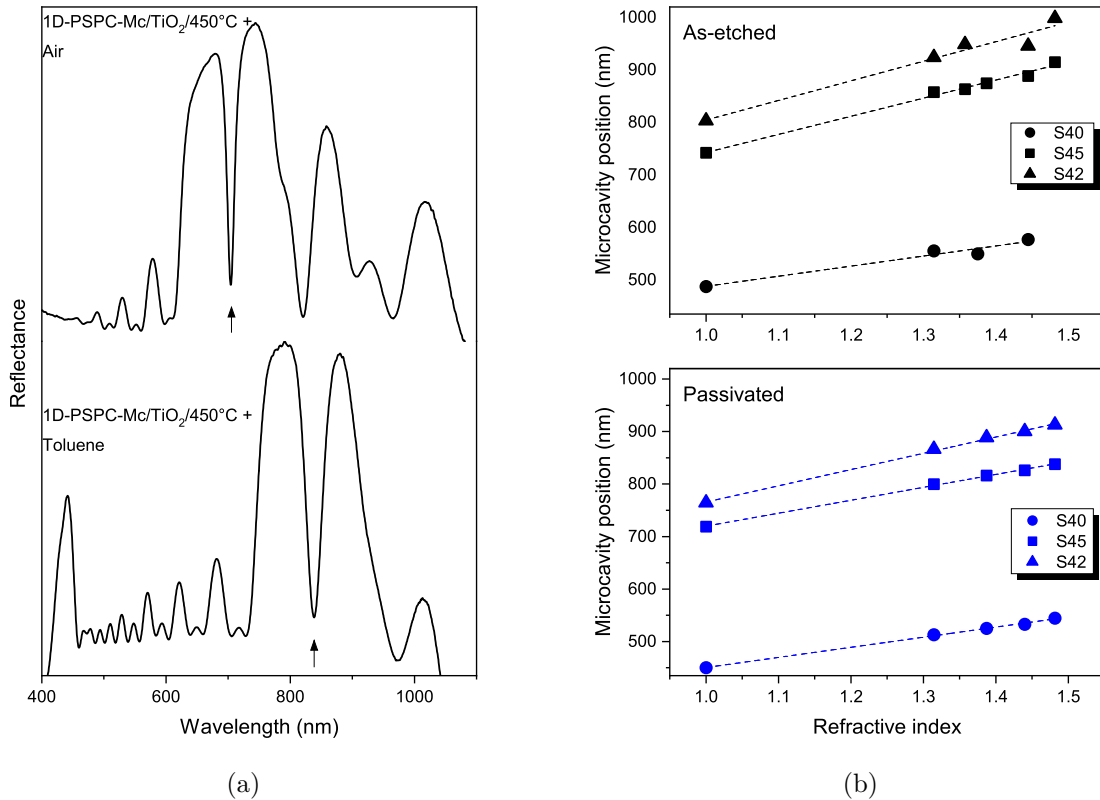


Figure 61 – (a) Reflectance spectra of S45 device before (above) and after immersion in organic solvent (toluene). Change of the microcavity position for the (b) as-etched and (c) passivated (TiO₂:450°C) devices S40 (0 s), S45 (2 s) and S42 (4 s).

Similar behavior was observed for the multilayer structure. The 1D-PSPC-Mc devices were immersed in organic solvents. Figure 61a shows the representative reflectance spectra of S45 in air (top) and after immersion in toluene (bottom). The λ_c shift to a higher wavelength is observed due to liquid infiltration with solvents having a higher refractive index than air. The relationship between the resonance peak and the refractive index of the solvent is shown in Figure 61b for the as-etched (top) and TiO₂/450°C passivated devices (bottom), respectively. However, comparing the results of single layers, the analysis of the λ_c shift is faster even with the naked eye. Moreover, the accuracy of this dependence of the λ_c refractive index on the solvent is higher.

5 Conclusions

Photonic crystals and microcavity devices based on porous silicon are of great importance in photonics, optoelectronics, and even optical sensors. The main difficulties for the fabrication of devices with excellent optical responses were associated with in-depth inhomogeneities. To solve it, the inclusion of a pause between layers during their formation was suggested. Although this strategy was reported as a possible solution, a systematic investigation about the effect of this pause was not systematically investigated. Here the systematic investigation provides the following conclusions:

- In photonic crystals and microcavities, the inclusion of a pause between two adjacent H and L layers shows a red shift in PBG. This behavior was caused by an increase in optical thickness, i.e., an increase in physical thickness and a decrease in porosity of each constituent layer. The change in PBG position and width is the result of an increase in thickness and a decrease in porosity due to the etch-stop time, which in turn promotes the restitution of HF at the etch-front during pore formation. With respect to the silicon etching rate, it was demonstrated that the silicon dissolution during pore formation depends on both the electrolyte type and the etch-stop time. H₂O in the ethanolic solution was found to improve the etching rate due to its oxidizing capability.
- The increasing thickness and decreasing porosity insofar the etch-stop time is not dependent on the stacking order of the H and L layers, since devices with HLHL... HL, and LHLH... LH show the same trend. But the HF diffusion in the electrolyte shows a dependence on the porosity of the top layer. Devices in which the first top layer has high porosity allow better diffusion of HF into the electrolyte and in this way increase the diffusion coefficient, but affect the mechanical and optical stability.
- As-etched porous structures are chemically unstable, so their chemical and optical properties change over time due to the formation of native oxides. Stabilization of these properties was achieved by passivation using SiO₂ growth or even by covering the porous surface with gold nanoparticles and TiO₂. However, despite the passivation material and after thermal treatment, the position of the passivated photonic crystal and microcavities undergoes a blueshift, while their width becomes narrower. In the structure HLHL... HL however, the effect of expansion-contraction due to oxidation leads to a violation of Bragg's law and thus to a loss of PBG. The thermal passivation was stable over time, which was confirmed by reflectance measurements after 20 and 36 weeks.

Annex

ANNEX A – Works presented at conferences and events

1. J. L. M. Villanueva, A.F. Oliveira and D.R. Huanca, Influence of the etch-stop upon the optical and structural properties of 1D-Porous Silicon Photonic Crystal. *11th Brazilian German Workshop on Applied Surface Science*.
2. J. L. M. Villanueva, A.F. Oliveira and D.R. Huanca, Porous silicon photonic crystals: Influence of the etch-stop on the optical response. *SBMicro 2022*.
3. J. L. M. Villanueva, A.F. Oliveira and D.R. Huanca. Influence of the electrolyte upon the optical response of 1D-Porous Silicon Photonic Crystal structures using the etch-stop method. *II Workshop de Física Experimental da UNIFEI, 2022*.
4. J. L. M. Villanueva, D.R. Huanca and A.F. Oliveira. Influence of the electrolyte and etch-stop time upon the optical response of 1D-Porous Silicon Photonic Crystal structures. *Workshop on Structures Light and its Applications, 2022*.

Bibliography

- 1 Steane, A. Quantum computing. *Reports on Progress in Physics*, IOP Publishing, v. 61, n. 2, p. 117, 1998.
- 2 Wei, Q.; and Ning, Z. Chiral perovskite spin-optoelectronics and spintronics: toward judicious design and application. *ACS Materials Letters*, ACS Publications, v. 3, n. 9, p. 1266–1275, 2021.
- 3 Rana, B.; Fukuma, Y.; Miura, K.; Takahashi, H.; and Otani, Y. Excitation of coherent propagating spin waves in ultrathin CoFeB film by voltage-controlled magnetic anisotropy. *Applied Physics Letters*, AIP Publishing, v. 111, n. 5, p. 052404, jul. 2017. Available in: <<https://doi.org/10.1063/1.4990724>>.
- 4 Martínez Ricci, M. L. *Respuesta electromagnética de cristales fotónicos 1D con metamateriales*. Tese — Faculty of Exact and Natural Sciences. Physics department. Buenos Aires' University, April 2009.
- 5 Wehrspohn, R.B.; Kitzrow, H.S.; and Busch, K. *Nanophotonic materials: photonic crystals, plasmonics, and metamaterials*. [S.l.]: John Wiley & Sons, 2008.
- 6 Maier, S. A.; and others. *Plasmonics: fundamentals and applications*. [S.l.]: Springer, 2007. v. 1.
- 7 Cvetkov, A. V.; Khanin, S. D.; Kumzerov, Y. A.; Puchkov, N. I.; Solovyev, V. G.; Vanin, A. I.; and Yanikov, M. V. *Excitation of surface plasmon-polaritons in metal-dielectric structures based on opals*. 2022.
- 8 Bruhier, H; Verrier, I; Gueye, T.; Varenne, C.; Ndiaye, A.; Parriaux, O.; Veillas, C.; and Reynaud, S.; and Brunet, J.; and Jourlin, Y. Effect of roughness on surface plasmons propagation along deep and shallow metallic diffraction gratings. *Optics Letters*, Optical Society of America, v. 47, n. 2, p. 349–352, 2022.
- 9 Sailor, M. J. *Porous Silicon in Practice. Preparation, Characterization and Applications*. [S.l.: s.n.], 2012.
- 10 Ramirez-Gutierrez, C. F.; Martinez-Hernandez, H. D.; Lujan-Cabrera, I. A.; and Rodriguez-García, M. E. Design, fabrication, and optical characterization of one-dimensional photonic crystals based on porous silicon assisted by in-situ photoacoustics. *Scientific reports*, Nature Publishing Group, v. 9, n. 1, p. 1–15, 2019.
- 11 Hamidi, S. M.; Tehranchi, M. M.; and Bananej, A. Adjustable faraday rotation by using engineered one-dimensional magneto photonic crystals. *Optical Materials*, Elsevier BV, v. 32, n. 9, p. 1085–1089, jul. 2010. Available in: <<https://doi.org/10.1016/j.optmat.2010.02.035>>.
- 12 Portela, G.; Dmitriev, V.; Zimmer, D. Ferromagnetic resonance isolator based on a photonic crystal structure with terahertz vortices. *Photonic Network Communications*, Springer, v. 39, n. 1, p. 47–53, 2020.

- 13 Kleine, T. S.; Diaz, L. R.; and Konopka, K. M.; Anderson, L. E.; Pavlopolous, N. G.; Lyons, N. P.; Kim, E. T.; Kim, Y.; Glass, R. S.; and Char, K.; and others. One dimensional photonic crystals using ultrahigh refractive index chalcogenide hybrid inorganic/organic polymers. *ACS Macro Letters*, ACS Publications, v. 7, n. 7, p. 875–880, 2018.
- 14 Wu, F.; Guang, L.; Zhiwei, G.; Jiang, H.; Xue, C.; Zheng, M.; Chen, C.; Du, G.; and Chen, H. Redshift gaps in one-dimensional photonic crystals containing hyperbolic metamaterials. *Physical Review Applied*, APS, v. 10, n. 6, p. 064022, 2018.
- 15 Ali, N. B.; Alshammari, S.; Trabelsi, Y.; Alsaif H.; Kahouli, O.; and Elleuch, Z. Tunable multi-band-stop filters using generalized fibonacci photonic crystals for optical communication applications. *Mathematics*, MDPI AG, v. 10, n. 8, p. 1240, abr. 2022. Available in: <<https://doi.org/10.3390/math10081240>>.
- 16 Galindo-Linares, E.; Halevi, P.; Sánchez, A.S. Tuning of one-dimensional Si/SiO₂ photonic crystals at the wavelength of 1.54 μm . *Solid State Communications*, Elsevier BV, v. 142, n. 1-2, p. 67–70, abr. 2007. Available in: <<https://doi.org/10.1016/j.ssc.2007.01.018>>.
- 17 Bonifacio, L. D.; Lotsch, B. V.; Puzzo, D. P.; Scotognella, F.; Ozin, G. A. Stacking the nanochemistry deck: Structural and compositional diversity in one-dimensional photonic crystals. *Advanced Materials*, Wiley, v. 21, n. 16, p. 1641–1646, abr. 2009. Available in: <<https://doi.org/10.1002/adma.200802348>>.
- 18 Graham, S. A.; Boyko, E.; Salama, R.; and Segal, E. Mass transfer limitations of porous silicon-based biosensors for protein detection. *ACS Sensors*, American Chemical Society (ACS), v. 5, n. 10, p. 3058–3069, set. 2020. Available in: <<https://doi.org/10.1021/acssensors.0c00670>>.
- 19 Pavese, L. Porous silicon dielectric multilayers and microcavities. *La Rivista del Nuovo Cimento*, Springer Science and Business Media LLC, v. 20, n. 10, p. 1–76, out. 1997. Available in: <<https://doi.org/10.1007/bf02877374>>.
- 20 Thönissen, M.; Berger, M. G.; Billat, S.; Arens-Fischer, R.; Krüger, M.; Lüth, H.; Theiss, W.; Hillbrich, S.; Grosse, P.; Lerondel, G.; and others. Analysis of the depth homogeneity of p-PS by reflectance measurements. *Thin Solid Films*, Elsevier, v. 297, n. 1-2, p. 92–96, 1997.
- 21 Abelès, F. Recherches sur la propagation des ondes électromagnétiques sinusoidales dans les milieux stratifiés. *Annales de Physique*, EDP Sciences, v. 12, n. 5, p. 596–640, 1950. Available in: <<https://doi.org/10.1051/anphys/195012050596>>.
- 22 Abelès, F. Les ondes électromagnétiques de surface et leur utilisation pour l'étude des surfaces et interfaces. *Le Journal de Physique Colloques*, EDP Sciences, v. 38, n. C5, p. C5–67–C5–75, nov. 1977. Available in: <<https://doi.org/10.1051/jphyscol:1977508>>.
- 23 Joannopoulos, J. D.; Johnson, S. G.; Winn, J. N.; and Meade, R. D. Photonic crystals. In: *Photonic Crystals*. [S.l.]: Princeton university press, 2011.
- 24 Taflove, A.; Hagness, A. *Computational Electrodynamics. The Finite-Difference Time-Domain Method*. [S.l.: s.n.], 1995.

- 25 John, S. Strong localization of photons in certain disordered dielectric superlattices. *Physical review letters*, APS, v. 58, n. 23, p. 2486, 1987.
- 26 Yablonovitch, E. Inhibited spontaneous emission in solid-state physics and electronics. In: *Confined Electrons and Photons*. Springer US, 1995. p. 841–844. Available in: <https://doi.org/10.1007/978-1-4615-1963-8_41>.
- 27 Barrows, F. P.; and Bartl M. H. Photonic structures in biology: A possible blueprint for nanotechnology. *Nanomaterials and Nanotechnology*, SAGE Publications, v. 4, p. 1, jan. 2014. Available in: <<https://doi.org/10.5772/58289>>.
- 28 Starkey, T.; and Vukusic, P. Light manipulation principles in biological photonic systems. *Nanophotonics*, Walter de Gruyter GmbH, v. 2, n. 4, p. 289–307, out. 2013. Available in: <<https://doi.org/10.1515/nanoph-2013-0015>>.
- 29 Prasad, P. N. *Nanophotonics*. [S.l.]: John Wiley & Sons, 2004.
- 30 Vigneron, J. P.; and Simonis, P. Natural photonic crystals. *Physica B: Condensed Matter*, Elsevier BV, v. 407, n. 20, p. 4032–4036, out. 2012. Available in: <<https://doi.org/10.1016/j.physb.2011.12.130>>.
- 31 Huanca, D. R.; and Salcedo, W. J. Optical characterization of one-dimensional porous silicon photonic crystals with effective refractive index gradient in depth. *Physica status solidi (a)*, Wiley, v. 212, n. 9, p. 1975–1983, abr. 2015. Available in: <<https://doi.org/10.1002/pssa.201532063>>.
- 32 Hu, Y.; Miles, B. T.; Ho, Y. L. D.; Taverne, M. P. C.; Lifeng Chen; Henkjan Gersen; Rarity, J. G.; and Faul, C. F. J. Toward Direct Laser Writing of Actively Tuneable 3D Photonic Crystals. *Advanced Optical Materials*, Wiley, v. 5, n. 3, p. 1600458, nov. 2016. Available in: <<https://doi.org/10.1002/adom.201600458>>.
- 33 Dhanekar, S.; and Jain, S. Porous silicon biosensor: Current status. *Biosensors and Bioelectronics*, Elsevier BV, v. 41, p. 54–64, mar. 2013. Available in: <<https://doi.org/10.1016/j.bios.2012.09.045>>.
- 34 Pacholski, C.; Sartor, M.; Sailor, M. J.; Cunin, F.; and Miskelly, G. M. Biosensing using porous silicon double-layer interferometers: reflective interferometric fourier transform spectroscopy. *Journal of the American Chemical Society*, American Chemical Society (ACS), v. 127, n. 33, p. 11636–11645, jul. 2005. Available in: <<https://doi.org/10.1021/ja0511671>>.
- 35 Huanca, D. R.; and Salcedo, W. J. Porous silicon photonic crystal applied as chemosensor for organic solvent. In: . [S.l.: s.n.], 2015.
- 36 Gorgutsa, S.; Berzowksa, J.; and Skorobogatiy, M. Optical fibers for smart photonic textiles. In: *Multidisciplinary Know-How for Smart-Textiles Developers*. Elsevier, 2013. p. 70–107e. Available in: <<https://doi.org/10.1533/9780857093530.1.70>>.
- 37 Boriskina, J. V.; Erokhin, S. G.; Granovsky, A. B.; Vinogradov, A. P.; and Inoue, M. Enhancement of the magnetorefractive effect in magnetophotonic crystals. *Physics of the Solid State*, Pleiades Publishing Ltd, v. 48, n. 4, p. 717–721, abr. 2006. Available in: <<https://doi.org/10.1134/s1063783406040160>>.

- 38 Stenzel, O.; and others. *The physics of thin film optical spectra*. [S.l.]: Springer, 2015.
- 39 Léron del, G.; and Romestain, R. Fresnel coefficients of a rough interface. *Applied Physics Letters*, AIP Publishing, v. 74, n. 19, p. 2740–2742, maio 1999. Available in: <<https://doi.org/10.1063/1.123999>>.
- 40 Lujan-Cabrera, I. A.; Ramirez-Gutierrez, C. F.; Castaño-Yepes, J. D.; and Rodriguez-Garcia, M.E. Effects of the interface roughness in the optical response of one-dimensional photonic crystals of porous silicon. *Physica B: Condensed Matter*, Elsevier BV, v. 560, p. 133–139, maio 2019. Available in: <<https://doi.org/10.1016/j.physb.2019.02.010>>.
- 41 Huanca, D. R. *Estruturas multicamadas de silício poroso para aplicação em dispositivos de cristais fotônicos*. Dissertação (Mestrado) — Escola Politécnica da Universidade de São Paulo, 2007.
- 42 Yeh, P.; Yariv, A.; and Hong, C.S. Electromagnetic propagation in periodic stratified media. i. general theory. *JOSA*, Optical Society of America, v. 67, n. 4, p. 423–438, 1977.
- 43 Pérez, E. X. Design, fabrication and characterization of porous silicon multilayer optical devices. *PhD thesis, Universitat Rovira I Virgili*, 2007.
- 44 Griffiths, D.J.; Griffiths, P.D.J.; and College, R. *Introduction to Electrodynamics*. Prentice Hall, 1999. ISBN 9780138053260. Available in: <<https://books.google.com.br/books?id=M8XvAAAAMAAJ>>.
- 45 Kittel, C. *Introduction to Solid State Physics*. 6th. ed. New York: John Wiley & Sons, Inc., 1986.
- 46 Pandey, J. P. Transfer matrix method for one-dimensional photonic crystals. *J. Ramanujan Soc. Math Math Sc*, v. 6, n. 1, p. 121–130, 2017.
- 47 Orfanidis, S. J. *Electromagnetic waves and antennas*. [S.l.]: Rutgers University New Brunswick, NJ, 2002.
- 48 Huanca, D. R. Porous silicon: A sponge-like structure for photonic based sensor devices. In: Klaus D. Sattler (Ed.). *21st Century Nanoscience—A Handbook. Design Strategies for Synthesis and Fabrication*. [S.l.]: CRC Press, 2020. cap. 4, p. 4–1 – 4–37.
- 49 Torres Rosales, A. A. *Fabricación y caracterización de microcavidades ópticas de silício poroso*. [S.l.]: Universidad Autónoma de San Luis Potosí Facultad de Ciencias, 2019.
- 50 Huanca, D. R. One-dimensional porous silicon photonic crystals. In: _____. *Silicon Nanomaterials Sourcebook: Low-Dimensional Structures, Quantum Dots, and Nanowires*. [S.l.]: CRC Press, 2017. v. 1, cap. 1, p. 3–42.
- 51 Lehmann V. *Electrochemistry of silicon: instrumentation, science, materials and applications*. [S.l.: s.n.], 2002.
- 52 Khriachtchev, L. *Silicon Nanophotonics: Basic Principles, Present Status, and Perspectives*. [S.l.]: CRC Press, 2016.
- 53 Lehmann, V; Stengl, R.; and Luigart, A. On the morphology and the electrochemical formation mechanism of mesoporous silicon. *Materials Science and Engineering B-advanced Functional Solid-state Materials*, v. 69, p. 11–22, 01 2000.

- 54 Svyakhovskiy, S. E.; Maydykovsky, A. I.; and Murzina, T. V. Mesoporous silicon photonic structures with thousands of periods. *Journal of Applied Physics*, AIP Publishing, v. 112, n. 1, p. 013106, jul. 2012. Available in: <<https://doi.org/10.1063/1.4732087>>.
- 55 Herrn, A.L. *Fabrication and characterization of macroporous silicon*. [S.l.]: Martin-Luther-Universität Halle-Wittenberg, 2018.
- 56 Lehmann, V.; and Rönnebeck, S. The physics of macropore formation in low doped p-type silicon. *Journal of The Electrochemical Society*, v. 146, n. 8, p. 2968–2975, 1999.
- 57 Theiß, W. Optical properties of porous silicon. *Surface Science Reports*, Elsevier, v. 29, n. 3-4, p. 91–192, 1997.
- 58 Pavesi, L.; Mazzoleni, C.; Guardini, R.; Cazzanelli, M; Pellegrini, V.; and Tredicucci, A. Porous-silicon microcavities. *Il Nuovo Cimento D*, Springer Science and Business Media LLC, v. 18, n. 10, p. 1213–1223, out. 1996. Available in: <<https://doi.org/10.1007/bf02464699>>.
- 59 Lehmann, V.; and Gösele, U. Porous silicon formation: A quantum wire effect. *Applied Physics Letters*, AIP Publishing, v. 58, n. 8, p. 856–858, fev. 1991. Available in: <<https://doi.org/10.1063/1.104512>>.
- 60 Léron del, G.; Reece, P.; Bruyant, A.; and Gal, M. Strong light confinement in microporous photonic silicon structures. *MRS Proceedings*, Springer Science and Business Media LLC, v. 797, 2003. Available in: <<https://doi.org/10.1557/proc-797-w1.7>>.
- 61 Rouquerol, J., et. al. Recommendations for the characterization of porous solids. *Pure & Appl. Chem.*, v. 66, n. 8, p. 1739–1758, 1994.
- 62 Garnett, J. C. M. Colours in metal glasses and in metallic films. *Phil. Trans. A*, v. 203, p. 385–420, 1904.
- 63 Looyenga, H. Dielectric constants of heterogeneous mixtures. *Physica*, Elsevier, v. 31, n. 3, p. 401–406, 1965.
- 64 Ghasemi-Mobarakeh, L.; Semnani, D.; and Morshed, M. A novel method for porosity measurement of various surface layers of nanofibers mat using image analysis for tissue engineering applications. *Journal of Applied Polymer Science*, Wiley, v. 106, n. 4, p. 2536–2542, 2007. Available in: <<https://doi.org/10.1002/app.26949>>.
- 65 Terao, T.; Inoue, G.; Kawase, M.; Kubo, N.; Yamaguchi, M.; Yokoyama, K.; Tokunaga, T.; Shinohara, K.; Hara, Y.; and Hara, T. Development of novel three-dimensional reconstruction method for porous media for polymer electrolyte fuel cells using focused ion beam-scanning electron microscope tomography. *Journal of Power Sources*, v. 347, p. 108–113, 2017. ISSN 0378-7753. Available in: <<https://www.sciencedirect.com/science/article/pii/S037877531730215X>>.
- 66 Washburn, E. W.; and Bunting, E. N. Porosity: VI. Determination of porosity by the method of gas expansion. *Journal of the American Ceramic Society*, Wiley, v. 5, n. 2, p. 112–130, fev. 1922. Available in: <<https://doi.org/10.1111/j.1151-2916.1922.tb17640.x>>.
- 67 Michael J, Sailor. *Porous Silicon in Practice - Preparation, characterization, and applications*. [S.l.: s.n.], 2012.

- 68 Huanca, D. R.; Ramirez-Fernandez, F. J.; and Salcedo, W. J. Porous silicon optical cavity structure applied to high sensitivity organic solvent sensor. *Microelectronics Journal*, Elsevier BV, v. 39, n. 3-4, p. 499–506, mar. 2008. Available in: <<https://doi.org/10.1016/j.mejo.2007.07.025>>.
- 69 Torres-Costa, V.; Salonen, J.; Jalkanen, T. M.; Lehto, V.-P.; Martín-Palma, R. J.; and Martínez-Duart, J. M. Carbonization of porous silicon optical gas sensors for enhanced stability and sensitivity. *physica status solidi (a)*, Wiley, v. 206, n. 6, p. 1306–1308, jun. 2009. Available in: <<https://doi.org/10.1002/pssa.200881052>>.
- 70 Huanca, D. R.; and Salcedo, W. J. Porous silicon heterostructures for refractometer device application. *ECS Transactions*, The Electrochemical Society, v. 23, n. 1, p. 499–506, set. 2009. Available in: <<https://doi.org/10.1149/1.3183756>>.
- 71 Salem, M. S.; Sailor, M. J.; Harraz, F. A.; Sakka, T.; and Ogata, Y. H. Electrochemical stabilization of porous silicon multilayers for sensing various chemical compounds. *Journal of Applied Physics*, AIP Publishing, v. 100, n. 8, p. 083520, out. 2006. Available in: <<https://doi.org/10.1063/1.2360389>>.
- 72 Pap, A. E.; Kordás, K.; Tóth, G.; Levoska, J.; Uusimäki, A.; Vähäkangas, J.; Lepävuori, S.; and George, T. F. Thermal oxidation of porous silicon: Study on structure. *Applied Physics Letters*, AIP Publishing, v. 86, n. 4, p. 041501, jan. 2005. Available in: <<https://doi.org/10.1063/1.1853519>>.
- 73 Ott, N.; Nerding, M.; Müller, G.; Brendel, R.; and Strunk, H. P. Evolution of the microstructure during annealing of porous silicon multilayers. *Journal of Applied Physics*, AIP Publishing, v. 95, n. 2, p. 497–503, jan. 2004. Available in: <<https://doi.org/10.1063/1.1633657>>.
- 74 El-Gamal, A. A.; Ibrahim, S. M.; and Amin, M. Impact of thermal oxidation on the structural and optical properties of porous silicon microcavity. *Nanomaterials and Nanotechnology*, SAGE Publications, v. 7, p. 184798041773570, jan. 2017. Available in: <<https://doi.org/10.1177/1847980417735702>>.
- 75 Neamen, D. A. *Semiconductor physics and devices: basic principles*. [S.l.]: McGraw-hill, 2003.
- 76 da Silva, M. P. C.; Oliveira, A. F. ; Huanca, D. R.; and da Silva, W. Y. A. Electrical characterization of Si-based/SiO₂ /TiO₂ heterostructures. *SBMicro*, 2021.
- 77 Billat, S.; Thönissen, M.; Arens-Fischer, R.; Berger, M. G.; Krüger, M.; and Lüth, H. Influence of etch stops on the microstructure of porous silicon layers. *Thin Solid Films*, Elsevier BV, v. 297, n. 1-2, p. 22–25, abr. 1997. Available in: <[https://doi.org/10.1016/s0040-6090\(96\)09421-7](https://doi.org/10.1016/s0040-6090(96)09421-7)>.
- 78 Vazquez, G.; Alvarez, E.; and Navaza, J. M. Surface tension of alcohol water + water from 20 to 50°C. *Journal of chemical and engineering data*, ACS Publications, v. 40, n. 3, p. 611–614, 1995.
- 79 Islam, S.; Bidin, N.; Osman, S. S.; Krishnan, G.; Salim, A. A.; Riaz, S.; Suan, L. P.; Naseem, S.; and Sanagi, M. M. Synthesis and characterization of ni NPs-doped silica–titania nanocomposites: structural, optical and photocatalytic properties. *Applied*

Physics A, Springer Science and Business Media LLC, v. 123, n. 1, dez. 2016. Available in: <<https://doi.org/10.1007/s00339-016-0685-4>>.

80 Christiansen, T. L.; Hansen, O.; Jensen, J. A.; and Thomsen, E. V. Thermal oxidation of structured silicon dioxide. *ECS Journal of Solid State Science and Technology*, The Electrochemical Society, v. 3, n. 5, p. N63–N68, 2014. Available in: <<https://doi.org/10.1149/2.003405jss>>.

81 Mun, K. S.; Alvarez, S. D.; Choi, W. Y.; and Sailor, M. J. A Stable, Label-free Optical Interferometric Biosensor Based on TiO₂ Nanotube Arrays. *ACS Nano*, American Chemical Society (ACS), v. 4, n. 4, p. 2070–2076, mar. 2010. Available in: <<https://doi.org/10.1021/nn901312f>>.

82 Hosny, M.; Wissem, D.; Ikbél, H.; and Hatem, E. Influence of gold nanoparticles deposition on porous silicon properties. *Sensors & Transducers*, IFSA Publishing, SL, v. 27, n. 5, p. 202, 2014.

83 Behzad, K.; Mat Yunus, W. M.; Talib, Z. A.; Zakaria, A.; and Bahrami, A. Preparation and thermal characterization of annealed gold coated porous silicon. *Materials*, MDPI AG, v. 5, n. 12, p. 157–168, jan. 2012. Available in: <<https://doi.org/10.3390/ma5010157>>.

84 Yakubovsky et al. *Optical constants of Au (Gold)*. 2017. Available in: <<https://refractiveindex.info/?shelf=main&book=Au&page=Yakubovsky-53nm>>. Accessed: Septembre 26, 2022.

85 Sarkar et al. *Optical constants of TiO₂ (Titanium dioxide)*. 2019. Available in: <<https://refractiveindex.info/?shelf=main&book=TiO2&page=Sarkar>>. Accessed: Septembre 26, 2022.

86 Barla, K.; Herino, R.; and Bomchil, G. Stress in oxidized porous silicon layers. *Journal of Applied Physics*, AIP Publishing, v. 59, n. 2, p. 439–441, jan. 1986. Available in: <<https://doi.org/10.1063/1.337036>>.

87 Zheng, D. W.; Huang, Y. P.; He, Z. J.; Li, A. Z.; Tang, T. A.; Kwor, R.; and Cui, Q.; and Zhang, X. J. Microstructure, heat treatment, and oxidation study of porous silicon formed on moderately doped p-type silicon. *Journal of applied physics*, American Institute of Physics, v. 81, n. 1, p. 492–496, 1997.

88 Pacholski, C. Photonic crystal sensors based on porous silicon. *Sensors*, MDPI AG, v. 13, n. 4, p. 4694–4713, abr. 2013. Available in: <<https://doi.org/10.3390/s130404694>>.

89 Astrova, E. V.; and Tolmachev, V. A. Effective refractive index and composition of oxidized porous silicon films. *Materials Science and Engineering: B*, Elsevier, v. 69, p. 142–148, 2000.

90 Balderas-Valadez, R. F.; Schürmann, R.; and Pacholski, C. One spot—two sensors: Porous silicon interferometers in combination with gold nanostructures showing localized surface plasmon resonance. *Frontiers in Chemistry*, Frontiers Media SA, v. 7, set. 2019. Available in: <<https://doi.org/10.3389/fchem.2019.00593>>.

- 91 Mahros, A. M.; and Tharwat, M M.; and Elrashidi, A. Exploring the impact of nanoparticles shape on the performance of plasmonic based fiber optics sensors. *Plasmonics*, Springer Science and Business Media LLC, v. 12, n. 3, p. 563–570, jun. 2016. Available in: <<https://doi.org/10.1007/s11468-016-0298-y>>.
- 92 Krishnamurthy, S.; Esterle, A.; Sharma, N. C.; and Sahi, S. V. Yucca-derived synthesis of gold nanomaterial and their catalytic potential. *Nanoscale Research Letters*, Springer Science and Business Media LLC, v. 9, n. 1, nov. 2014. Available in: <<https://doi.org/10.1186/1556-276x-9-627>>.
- 93 Rohaeti, E.; and Hikmawati, I. Production of semiconductor materials silicon from silica rice husk waste as alternative silicon sources. *Journal Material Science and Technology*, 2010.
- 94 Font, F.; and Myers, T. G. Spherically symmetric nanoparticle melting with a variable phase change temperature. *Journal of Nanoparticle Research*, Springer Science and Business Media LLC, v. 15, n. 12, nov. 2013. Available in: <<https://doi.org/10.1007/s11051-013-2086-3>>.
- 95 Coblenz Society. *Infrared Spectrum of p-Xylene*. 1966. Available in: <<https://webbook.nist.gov/cgi/cbook.cgi?ID=C106423&Type=IR-SPEC&Index=4>>. Accessed: October 16, 2022.
- 96 Coblenz Society. *Infrared Spectrum of o-Xylene*. 1970. Available in: <<https://webbook.nist.gov/cgi/cbook.cgi?ID=C95476&Units=SI&Type=IR-SPEC&Index=2#IR-SPEC>>. Accessed: October 16, 2022.
- 97 Coblenz Society. *Infrared Spectrum of m-Xylene*. 1970. Available in: <<https://webbook.nist.gov/cgi/cbook.cgi?ID=C108383&Units=SI&Type=IR-SPEC&Index=3#IR-SPEC>>. Accessed: October 16, 2022.
- 98 Verma, R.; Gangwar, J.; and Srivastava, A. K. Multiphase TiO₂ nanostructures: a review of efficient synthesis, growth mechanism, probing capabilities, and applications in bio-safety and health. *RSC Advances*, Royal Society of Chemistry (RSC), v. 7, n. 70, p. 44199–44224, 2017. Available in: <<https://doi.org/10.1039/c7ra06925a>>.
- 99 Bagheri, S.; Shameli, K.; and Abd Hamid, S. B. Synthesis and characterization of anatase titanium dioxide nanoparticles using egg white solution via sol-gel method. *Journal of Chemistry*, Hindawi Limited, v. 2013, p. 1–5, 2013. Available in: <<https://doi.org/10.1155/2013/848205>>.
- 100 Rajakumar, G.; Rahuman, A. A.; Roopan, S. M.; Khanna, V. G.; Elango, G.; Kamaraj, C.; Zahir, A. A.; and Velayutham, K. Fungus-mediated biosynthesis and characterization of tio₂ nanoparticles and their activity against pathogenic bacteria. *Spectrochimica Acta Part A: Molecular and Biomolecular Spectroscopy*, Elsevier BV, v. 91, p. 23–29, jun. 2012. Available in: <<https://doi.org/10.1016/j.saa.2012.01.011>>.
- 101 Zhang, H.; Wang, X.; Li, N.; Xia, J.; Meng, Q.; Ding, J.; and Lu, J. Synthesis and characterization of TiO₂/graphene oxide nanocomposites for photoreduction of heavy metal ions in reverse osmosis concentrate. *RSC Advances*, Royal Society of Chemistry (RSC), v. 8, n. 60, p. 34241–34251, 2018. Available in: <<https://doi.org/10.1039/c8ra06681g>>.

- 102 Senthilkumar, S.; Ashok, M.; Kashinath, L.; Sanjeeviraja, C.; and Rajendran, A. Phytosynthesis and characterization of TiO₂ nanoparticles using *Diospyros ebenum* leaf extract and their antibacterial and photocatalytic degradation of crystal violet. *Smart Science*, Informa UK Limited, v. 6, n. 1, p. 1–9, dez. 2017. Available in: <<https://doi.org/10.1080/23080477.2017.1410012>>.
- 103 Du, Y.; Huang, L.; Wang, Y.; Yang, K.; Zhang, Z.; Wang, Y.; Kipper, M.; Belfiore, L.; and Tang, J. Preparation of graphene oxide/silica hybrid composite membranes and performance studies in water treatment. *Journal of Materials Science*, Springer Science and Business Media LLC, v. 55, n. 25, p. 11188–11202, maio 2020. Available in: <<https://doi.org/10.1007/s10853-020-04774-5>>.
- 104 Ngoc, K. H. P.; and Vu, A. T. Simple Preparation of the CuO-Fe₃O₄/Silica Composite from Rice Husk for Enhancing Fenton-Like Catalytic Degradation of Tartrazine in a Wide pH Range. *Adsorption Science & Technology*, Hindawi Limited, v. 2022, p. 1–16, jun. 2022. Available in: <<https://doi.org/10.1155/2022/6454354>>.
- 105 Panwar, K.; Jassal, M.; and Agrawal, A. K. TiO₂-SiO₂ Janus particles with highly enhanced photocatalytic activity. *RSC Advances*, Royal Society of Chemistry (RSC), v. 6, n. 95, p. 92754–92764, 2016. Available in: <<https://doi.org/10.1039/c6ra12378c>>.
- 106 Bhau, B. S.; Ghosh, S.; Puri, S.; Borah, B.; Sarmah, D. K.; and Khan, R. Green synthesis of gold nanoparticles from the leaf extract of nepenthes khasiana and antimicrobial assay. *Advanced Materials Letters*, International Association of Advanced Materials, v. 6, n. 1, p. 55–58, jan. 2015. Available in: <<https://doi.org/10.5185/amlett.2015.5609>>.
- 107 Lopes, I. M. F.; Abersfelder, K.; Oliveira, P. W.; Mousavi, S. H.; and Junqueira, R. M. R. Flower-like silicon dioxide/polymer composite particles synthesized by dispersion polymerization route. *Journal of Materials Science*, Springer Science and Business Media LLC, v. 53, n. 16, p. 11367–11377, maio 2018. Available in: <<https://doi.org/10.1007/s10853-018-2378-1>>.
- 108 Mulloni, V.; and Pavesi L. Porous silicon microcavities as optical chemical sensors. *Applied Physics Letters*, AIP Publishing, v. 76, n. 18, p. 2523–2525, maio 2000. Available in: <<https://doi.org/10.1063/1.126396>>.
- 109 De Stefano, L.; Rendina, I.; Moretti, L.; and Rossi, A. M. Optical sensing of flammable substances using porous silicon microcavities. *Materials Science and Engineering: B*, Elsevier BV, v. 100, n. 3, p. 271–274, jul. 2003. Available in: <[https://doi.org/10.1016/s0921-5107\(03\)00114-4](https://doi.org/10.1016/s0921-5107(03)00114-4)>.
- 110 Kim, H. J.; Kim, Y. Y.; Lee, K. W.; and Park, S. W. A distributed bragg reflector porous silicon layer for optical interferometric sensing of organic vapor. *Sensors and Actuators B: Chemical*, Elsevier BV, v. 155, n. 2, p. 673–678, jul. 2011. Available in: <<https://doi.org/10.1016/j.snb.2011.01.028>>.
- 111 Snow, P. A.; Squire, E. K.; Russell, P. St. J.; and Canham, L. T. Vapor sensing using the optical properties of porous silicon bragg mirrors. *Journal of Applied Physics*, AIP Publishing, v. 86, n. 4, p. 1781–1784, ago. 1999. Available in: <<https://doi.org/10.1063/1.370968>>.

112 Fellah, S.; Wehrspohn, R. B.; Gabouze, N.; Ozanam, F.; and Chazalviel, J.-N. Photoluminescence quenching of porous silicon in organic solvents: evidence for dielectric effects. *Journal of Luminescence*, Elsevier BV, v. 80, n. 1-4, p. 109–113, dez. 1998. Available in: <[https://doi.org/10.1016/s0022-2313\(98\)00077-5](https://doi.org/10.1016/s0022-2313(98)00077-5)>.